Title
Tapering Enhanced Stimulated Superradiant Amplification

Author
Park, Youna

Publication Date
2022

Peer reviewed|Thesis/dissertation

UNIVERSITY OF CALIFORNIA
Los Angeles

Tapering Enhanced Stimulated Superradiant Amplification

A dissertation submitted in partial satisfaction
of the requirements for the degree
Doctor of Philosophy in Physics

by

Youna Park

2022

ABSTRACT OF THE DISSERTATION

Tapering Enhanced Stimulated Superradiant Amplification

by

Youna Park
Doctor of Philosophy in Physics
University of California, Los Angeles, 2022
Professor Pietro Musumeci, Chair

High average and peak power radiation sources across the entire range of the electromagnetic spectrum have the potential for breakthrough advances in many scientific and technology areas, ranging from single-molecule imaging in the X-rays, to EUV lithography to particle acceleration and space applications using VIS/IR lasers.

The inherent characteristics of Free-Electron Lasers (FELs) such as peak power, coherence, and wavelength adjustability coupled with high repetition rate / high efficiency electron accelerators make them nearly ideal radiation sources, operating in vacuum with essentially no mechanism for waste heat and material breakdown.

On the other hand, the efficiency of the short wavelength FELs is typically limited to less than 1 % by saturation effects. A traditional method to increase the efficiency is to vary the undulator parameters with the electron beam energy by tapering. While FEL tapering research started decades ago, the UCLA group has been recently pointed out a novel approach (termed TESSA or tapering enhanced stimulated superradiant amplification) in which electron beams enter a strongly tapered undulator already pre-bunched along with an intense seed laser. In this case, the seed laser can efficiently decelerate the prebunched

electrons converting large fraction of their kinetic energy into superradiant coherent emission, significantly increasing the output power of the system.

As a preliminary study, the Nocibur experiment at Brookhaven National Laboratory few years ago investigated the resonant interaction of a high intensity 10.3 μm 200 GW seed laser, a 65 MeV electron beam, in a short 54 cm long tapered helical undulator. While the experiment measured high deceleration efficiency of 30 %, an accurate characterization of the radiation was not possible because the high seed power would damage the diagnostics. This document discusses the next generation experiment in this line of research (TESSA-266) aimed at demonstrating 10 % conversion efficiency in the UV range of the electromagnetic spectrum. The name of the experiment is due to the original target wavelength (266 nm), even though after reviewing the experimental parameter the target wavelength shifted to 257.5 nm. The experiment was designed to use the Argonne National Laboratory (ANL) Advanced Photon Sources (APS) linac electron beam at an energy 343 MeV, and a seed power of 1 GW. Due to the moderate amount of seed power, the TESSA-266 is in a high-gain regime in which the radiation field grows significantly along the undulator. This document discusses the magnetic design of the TESSA undulator and prebuncher section, the beamline design for the seed laser transport, the tapering optimization, start-to-end beam dynamics, and the post-undulator diagnostics for future experiments.

Due to complexities associated with the 2020 COVID pandemic, the experiment was postponed. This document also discusses a recent related experiment called TESSAtron, where the already built TESSA undulator was used at Pegasus Laboratory at UCLA to demonstrate the TESSA path to a very high efficiency at a longer wavelength. In the TESSAtron experiment, we combined the TESSA concept with the so called zero-slippage interaction where the group velocity of the radiation is matched with that of the electrons by using a waveguide in the undulator. A prebunched electron beam was generated using velocity bunching in the photoinjector and then decelerated in the strongly tapered undulator by around 10 %.

Even though the long range of the program is to push the TESSA concept to shorter wavelengths, these results are very important in their own right. The THz range is often called a "THz Gap" because conventional radiation sources such as the vacuum electronic sources and the solid state lasers do not generate power efficiently in this range. Obtaining a higher average power radiation source is critical for many areas such as plasma ignition, nuclear power sources, and laser based propulsion.

The dissertation of Youna Park is approved.

Robert Candler

Anshul Kogar

Michalis Bachtis

Pietro Musumeci, Committee Chair

University of California, Los Angeles

2022

To my family..

TABLE OF CONTENTS

LIST OF FIGURES

LIST OF TABLES

ACKNOWLEDGMENTS

I am very thankful for the opportunity to have participated in the FEL experiment during my graduate studies. It gave me the opportunity to do computational and experimental work. The experience of working with different people and groups was invaluable for me. As the proverb goes,"It takes a village to raise a child." It took the wisdom and encouragement from many others to help me grow in science and in my personal life.

I would like to thank my advisor Professor Pietro Musumeci for his dedicated support throughout the journey. His enthusiasm, wisdom, honesty, and discernment were very helpful for me. I am also very thankful for David Cesar, Nick Sudar, Emma Curry Snively, and Claudio Emma for being there to help in the early stages of the journey when I was like a little kid in the field. I am thankful for David Dang, Jack Isen, and Grace O'Neill for the great time spent working with the magnets. I thank Andrew Fisher, Alex Ody, Eric Cropp, Max Lenz, Paul Denham, and Sophie Crisp for their help with the experimental work. I am also thankful for Gerard Lawler, Walter Lynn, Nathan Majernik, Joshua Mann, Gerard Andonian, and Oliver Williams for being enthusiastic office mates. I would like to thank all of the PBPLers for their contagious enthusiasm for science.

I would like to thank Tara Hodgetts, Ron Agustsson, Ivan Gadjev, and Alex Murokh at Radiabeam for their continuous help with the engineering work. I would also like to thank Sasha Zholents, Bill Berg, Soonhong Lee, Alex Lumpkin, Jeff Dooling, Yine Sun, Kent Wootton, Michael Borland, and Bob Soliday for helping me during my SCGSR year. I also thank Chris Hall and Stephen Webb at Radiasoft and Wei Hou Tan at Northern Illinois University for helping with the beamline simulation. I also thank Alex Weil for helping with the English while writing this document.

As for the materials in my dissertation, some materials in Chapter 1 and 2 are from a co-authored publication on the TESSA experiment[85]. Pietro Musumeci contributed the background information of the TESSA experiment, Tara Campese contributed the engineer-

ing perspectives about the TESSA undulator and the break section, Paul Denham and Ivan Gadjev contributed the magnetic designs of the hybrid quadrupole and the electromagnetic dipole in the break section, respectively, and Andrew Fisher contributed the magnetic measurement of the undulator. The pictures of the prebuncher and the undulator are from Ivan Gadjev. The start-to-end simulation presented in this document is from an optimization run in the APS Weed Cluster, and Bob Soliday, Michael Borland, and Yine Sun helped me with the genetic optimizer in the cluster. Sirepo, Jupyter Server by Radiasoft (a public HPC server with accelerator codes) and NERSC were also used for the beamline simulation. Chris Hall and Wei Hou Tan helped with the start-to-end simulation and investigated various options of nonlinear corrections and optimization of transverse parameters, respectively. The post-undulator diagnostics design was provided by Sasha Zholents.

Some materials in the third chapter are from an article that has been published [41]. Andrew Fisher worked on undulator tuning and alignment, analytical perspectives, and matching the experimental results at different beam energy with the GPT-FEL simulation. Alex Ody helped with beamline operation and clarified the RF setup of the Pegasus Laboratory (Figure 3.6), and Max Lenz provided the THz transmission in the undulator and the diagnostics, as well as the THz pulse length[66]. Gerard Andonian provided the THz interferometer (BLISS), the THz source, as well as the engineering help regarding the diagnostics section. Finally, my advisor Pietro Musumeci offered helpful supervision and analytical perspectives throughout my participation in the TESSA program and the TESSAtron experiment. He also provided instructions and corrections while writing this document.

The LEA-TESSA research has been supported by DOE BES grant DE-SC0021190, DOE SBIR/STTR grants DE-SC0017102, DE-SC0018559, and DE-SC0018571. This research used resources of the Advanced Photon Source, a U.S. Department of Energy (DOE) Office of Science User Facility, operated for the DOE Office of Science by Argonne National Laboratory under Contract No. DE-AC02-06CH11357. This research used resources of the National Energy Research Scientific Computing Center (NERSC), a U.S. Department of Energy Of-

fice of Science User Facility located at Lawrence Berkeley National Laboratory, operated under Contract No. DE-AC02-05CH11231 using NERSC award BES-ERCAP0019016. The TESSAtron research has been supported by NSF grant no. PHY-1734215 and DOE grants nos. DE-SC0009914 and DE-SC0021190.

Finally, I would also like to thank my family for the continuous support through my years in the academia. I would not have made it through the doctoral process without their help. I am also thankful for the Blessed Family for helping with my spiritual needs. I thank God most of all for allowing the great opportunity to grow and for His presence of joy, mercy, and kindness throughout the journey.

VITA

2007-2012 B.S. Physics, UCLA

2014-2017 Teaching Assistant, UCLA

2017-2022 Graduate Student Researcher under Pietro Musumeci, UCLA Particle Beam Physics Laboratory

PUBLICATIONS

Y. Park, P. Musumeci et al, "Tapered helical undulator system for high efficiency energy extraction from a high brightness electron beam", Nucl. Instrum. Meth. A, vol. 1028, p. 166 370, 2022, DOI: 10.1016/j.nima.2022.166370

A. Fisher, Y. Park, P. Musumeci, et al, "Single pass high efficiency THz Free Electron Laser", Nat. Photonics, 2022, DOI: 10.1038/s41566-022-00995-z

Y. Park, et al, "Strongly Tapered Undulator Design for High Efficiency and High Gain Amplification at 266 nm," FEL2019, DOI: 10.18429/JACoW-FEL2017-MOP011

CHAPTER 1

Introduction to TESSA

1.1 Background

Modern particle accelerators are very efficient in converting and concentrating wall-plug electrical power into relativistic electron beams [83, 6]. At the same time, converting this energy into coherent radiation in an efficient manner still remains an open challenge. Beam-matter interaction is inefficient, generates large amount of heat and the electromagnetic energy is degraded to incoherent radiation. Free-electron laser (FEL) schemes potentially have very low losses as the interaction between charged particles and radiation takes place in vacuum, but in their practical implementation have been so far still limited to efficiencies at short wavelength on the order of the ρ FEL parameter, which is typically well below 1% [12]. Improving the conversion efficiency of relativistic electron beam power into coherent short wavelength radiation in FELs has the potential to enable fundamental breakthroughs in various areas of science and industry owing to the fact that high efficiency FELs are essentially ideal light sources, capable of very high average and peak power (only limited by beam power) and tunable over the entire region of the electromagnetic spectrum simply changing the e-beam energy [62].

High repetition rate linear accelerators can be used to generate electron beams with MW-class average power. Within a single pulse, high brightness radiofrequency (RF) photoinjector technology in combination with RF compression allows for extremely high (10-100 kA) peak currents at 10 GeV energies, approaching PW peak power levels in state-of-the-art

facilities [118]. Notably, state-of-the-art coherent X-ray sources do not take advantage of all the available power stored in the beam. Most of it is left in the unconverted particle kinetic energy and simply wasted on the beam dump [71].

Being able to convert a sizable fraction of this power into X-rays would enable dream-like goals, which are still far from being achievable at state-of-the-art 4th generation XFELs, including single-shot diffract-before-destroy coherent imaging [45] and access to Schwinger field physics [2]. In the EUV range of the electromagnetic spectrum, a very high average FEL-based source could provide a path for fast throughput material processing (EUV-lithography at 13.5 nm) and potentially offering down the line another option for continuing Moore's law exponential trend, should effective multi-layer optics be developed at a shorter wavelength [84, 56, 77].

The physical concept that we pursue in the quest for very high efficiency FELs is the so-called Tapering-Enhanced-Stimulated-Spontaneous-Amplification [29, 48] regime where high intensity seed and pre-bunched electron beams are used in combination with strongly tapered undulators to sustain high gradient deceleration over extended distances, resulting in converting more energy from the beam into coherent radiation.

The TESSA program aims at addressing the efficiency limitations in electron-based coherent radiation generation by exploiting recent progress in high brightness beam sources and increased understanding of the strong coupling with the electromagnetic field in tapered undulator systems [35, 39, 69, 97]. The program is the result of a collaborative effort of UCLA, RadiaBeam, Argonne National Laboratory and RadiaSoft and has been formed based on the possibility to use the high brightness beam from the APS linac, an electron accelerator with energy up to 500 MeV, and nominally operated around 350 MeV. The resulting project, named TESSA-266 is a seeded FEL experiment operating in the TESSA regime with the goal of demonstrating record high single pass energy extraction efficiency in the strongly tapered seeded regime at UV wavelengths.

1.1.1 Outline of this dissertation

The main subject of this dissertation is the exploration of the possibility of high peak radiation power and efficiency generated from a strongly tapered undulator system and prebunched electrons. This first chapter introduces the basic principles of a free electron laser (FEL) and provides the historical background of tapered FELs. Applications of high power radiation sources are presented. We then move on to the theoretical aspects of high efficiency FELs presenting an analysis in a 1D approximation. After introducing the complexity coming from the three dimensional effects, we present the numerical simulations that take advantage of modern computing resources to tackle this problem.

The next chapter discusses the TESSA experiment assuming that the experiment would be held at the Linac Extension Area (LEA) beamline of the Advanced Photon Source (APS) at Argonne National Laboratory. The magnetic design of the undulator is optimized for the LEA beam energy of 343 MeV and the target resonant wavelength of 266 nm. The injection chicane and the prebuncher chicane are designed according to the availability of the laboratory space and the dipole magnets. The undulator break section is one of the novelties in the project as it both optimizes the phase shift and refocuses the beam in a short distance. The simulation methods for optimizing the tapering in the time independent and time dependent schemes are discussed. Numerical studies for the acceptable tolerances in the experimental parameter indicate the engineering and physics design requirements for this experiment. The design for the post-undulator diagnostics is also provided for future reference. While the main subject of the second chapter is the TESSA experiment assuming the availability of the LEA beam, the realistic plans for the LEA-TESSA experiment have been shifted due to the schedule in the laboratory and the COVID situation. Discussions are underway to conduct the actual experiment at the Fermilab Accelerator Science and Technology (FAST) facility at a different e-beam energy, but this development is beyond the scope of this document.

The last chapter discusses a recent experiment held at the Pegasus Laboratory (UCLA) which utilizes the TESSA undulator to study the terahertz wavelength in zero-slippage interaction. The experiment is called TESSAtron referring to the tapering enhanced superradiant amplification in a different context involving the waveguide dispersion. In the zero-slippage interaction, the velocities of the radiation and the electron beam are matched tangentially (as opposed to an intersection point with two lines of different slopes). Unlike the TESSA experiment, the TESSAtron experiment does not have a prebuncher or a seed; the electrons are velocity-bunched from the photoinjector and produce the photons which are the seed for the superradiance in the undulator (which makes the acronym work as in spontaneous superradiant amplification). This last chapter describes the reasons to study the terahertz radiation wavelength and introduces the zero slippage interaction. The experimental setup provides the important details of the Pegasus-TESSAtron beamline and the experimental methods to measure the energy of the electron beam and the terahertz radiation. The experimental results show an average extraction efficiency of 10%. The chapter provides supplemental details of the simulation of the Pegasus beamline and the undulator and ends with a summary of experimental methods for operating the Pegasus beamline. The methods apply to other experiments besides the TESSAtron and serve as future reference.

1.2 Free Electron Laser

A free electron laser is a device in which electrons and radiation pass through a periodic magnetic array, called undulator, resulting in radiation amplification (Figure 1.1). A free electron laser can produce high brightness, high peak power radiation with the capability of tuning the wavelength, which is not possible for a conventional, optical laser in which its wavelength depends on the medium atomic properties. A free electron laser is an accelerator based light source which uses accelerated electron beams from a linear accelerator to produce the light. A synchrotron, in which electrons are guided by bending magnets to orbit in a

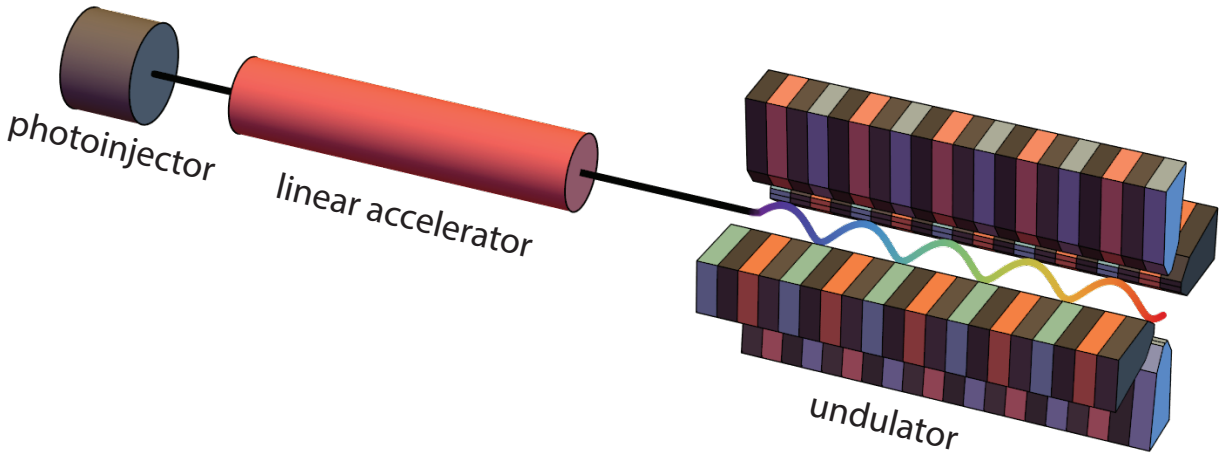

Figure 1.1: A free electron laser setup consists of an electron source, a linear accelerator, and a helical undulator

circular motion, is another accelerator based light source. A free electron laser produces coherent radiation with orders of magnitude higher brightness than that of a synchrotron by passing electron beams through an undulator. An undulator is a magnetic insertion device that guide electrons in a sinusoidal or helical trajectory. An undulator and a wiggler refer to the same kind of device, but the term undulator is more used for higher photon energy (smaller wavelengths).

The concept of a free electron laser derives from the better understanding of the electromagnetic interaction between charged particles and radiation that the physicists gained in the 1950s. While the idea of accelerating electrons by magnetic induction was realized back in 1902[60], the 2.3 MeV betatron built by Kerst at General Electric in 1941 was the first planned and engineered device to accelerate electrons by magnetic induction [59]. The device accelerated electrons in a evacuated tube placed between electromagnets. The researchers at General Electric improved the device to accelerate electrons to 100 MeV in 1945, but they could not detect radiation because the chamber was opaque and the relativistic effects on the wavelength was not realized. Radiation due to the interaction between electron and

external electromagnetic field was first measured in 1947 from a 70 MeV synchrotron made by the researchers at General Electric [32], so the name "synchrotron radiation" was given to describe the radiation from the motion of electrons in the magnetic field.

An undulator radiation was first measured in the experiment by Motz et al at Stanford in 1953[76]. They measured millimeter radiation from an 100 MeV electron beam passing through an undulator. Many years later, the radiation of 10.6 μm wavelength at 4 kW due to stimulated measured by Madey, et al at Stanford University in 1976 is considered as the first free electron laser experiment. The experiment showed an amplified radiation signal due to stimulated emissions from an 24 MeV energy electron beam passing through a 5.2 m constant, periodic magnetic field generated by a superconducting double helix [33]. A laser is an acronym for light amplification by stimulated emission of radiation, and Madey's publications showed how the amplified radiation from the interaction of electrons and a seed laser is in analogy with one in an optical laser. The success of the experiment opened a new way to construct a laser system with orders of magnitudes higher brightness and more versatile parameters than an atomic laser, and also offered interesting insights about classical physics and quantum mechanical system inherent in an FEL system. Radiation emitted from an electron beam passing through periodic magnetic fields can be described by Lorentz contraction and relativistic Doppler shift. Lorentz contraction refers to a phenomenon in which an object moving near the speed of light appears shorter to an observer at a laboratory frame. If the object moves with energy described by a relativistic Lorentz factor $\gamma = \frac{1}{1-v^2/c^2}$, the object will appear having a shorter length $L = \frac{L'}{\gamma}$ in the laboratory frame. When electrons pass through the undulator, in the rest frame of the electrons (primed), the electrons observe the period of the "moving" periodic field as a shorter period, so the electrons emit radiation with a wavelength of

$$\lambda = \frac{1}{\gamma}\lambda' = \frac{1}{\gamma}\lambda_u \tag{1.1}$$

as shown in Figure 1.2.

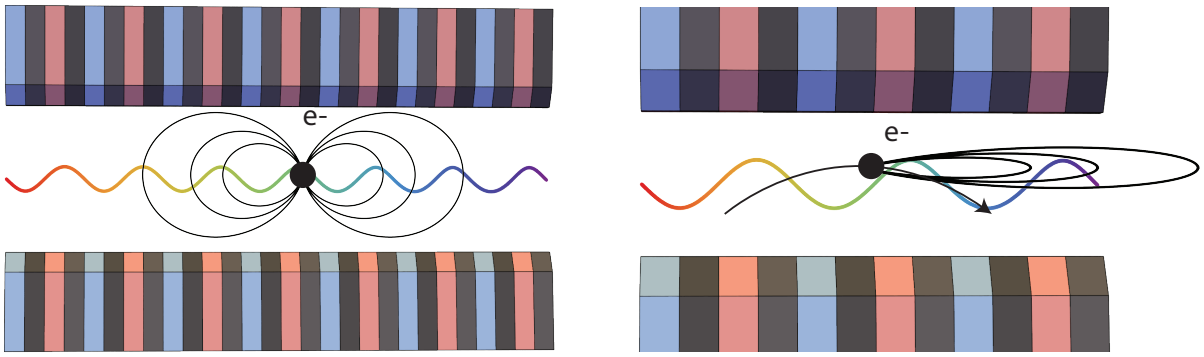

(a) (b)

Figure 1.2: Due to the Lorentz contraction, the undulator periods are shown shorter from the rest frame of the electrons (a), emitting dipole radiation with the periods contracted by $1/\gamma$. In the laboratory frame, the radiation wavelengths are further shortened due to the relativistic Doppler effects. Relativistic aberration also narrow the radiation cone.

On the other hand, the Doppler effect also influences the observed wavelength. The Doppler effect refers to the frequency shift of a wave emitted by a source when a source or an observer moves. When the source approaches the observer, the frequency shifts higher by $f_1 = \frac{1}{1-\frac{v}{c}} f_0$. Meanwhile, when the source moves near the speed of light, the emitted wave appears to have a longer period due to the time dilation $\tau = \gamma\tau'$, so the observed frequency is smaller than the frequency from the source. The frequency shift when the source approaches the observer in relativistic Doppler shift is

$$f_1 = \frac{1}{(1-\beta)}\frac{1}{\gamma} f_0 \approx 2\gamma f_0 \tag{1.2}$$

for relativistic approximation $1-\beta \approx \frac{1}{2\gamma^2}$, and so the observed wavelength is

$$\lambda_1 = \frac{1}{2\gamma}\lambda_0. \tag{1.3}$$

Therefore, the radiation wavelength λ_s emitted by a moving charge passing through the periodic field of period λ_u in the laboratory frame is influenced by both Lorentz contraction

and Doppler effect:

$$\lambda_s \approx \frac{1}{2\gamma^2}\lambda_u. \tag{1.4}$$

A free electron laser setup with electrons of beam energy γ moving through an undulator of period λ_u will accordingly emit radiation wavelength λ_s as shown above.

As it will be derived later in this chapter, the FEL resonance condition given a helical undulator is

$$\lambda_s = \frac{\lambda_u}{2\gamma^2}(1 + K^2) \tag{1.5}$$

where $K = eB_w/k_w mc$ is the undulator vector potential parameter, in which B_w is the on-axis magnetic field of the undulator and k_w is the wave vector of the undulator, λ_w is the undulator period, λ_s is the radiation wavelength, and γ is the electron beam energy. When the resonance condition is satisfied, the electron beam and radiation will interact to amplify the radiation intensity.

1.3 The History of Tapered FELs

With the successful measurement of gain at 10.6μm from a free electron laser by Madey, et al in 1976, the Stanford researchers operated a free electron laser oscillator at 3.4μm with average power of 0.36 W and peak power of 7kW from an electron beam of 43.5 MeV energy, 130 μA average current, and 0.06 mm mrad beam emittance, resulting with 0.01% efficiency [23]. While the extraction efficiency was higher at 0.25% in a following paper discussing the pulse length measurements of the FEL oscillator setup using an optical autocorrelation apparatus involving Michelson interferometry [9], the researchers at the time were already highly interested about increasing the FEL efficiency.

In 1981, Kroll, Morton, and Rosenbluth (KMR) contributed an important analysis of changing undulator parameters to keep the electrons in resonance. By varying the undulator

parameters such as the magnetic field or the period while the electron decelerates, more electrons can be trapped in the ponderomotive potential.

Warren, Brau, et al at Los Alamos National Laboratory in 1983 showed 3.7 % energy extraction efficiency at 10.6μm wavelength from a 20 Mev e-beam passing through an 100 cm long undulator that was period-tapered by 12 % [113]. Also, Orzechowski, et al in collaboration with Lawrence Berkeley Laboratory (LBL) and Lawrence Livermore National Laboratory (LLNL) in 1986 showed high extraction efficiency of 34 % from a 3-meter-long single-pass amplifier built to operate in the microwave regime at 34.6 GHz, which is around 9 mm in wavelength. The experiment was conducted at Electron Test Facility (ELF) of LLNL, where the electron beam source produced energy of 4.5 MeV and 10 kA current, while the the amplifier was tapered by 45% in the magnetic field from 5 kG. [81].

After this, there was significant activity in the field of tapered FELs. The analytical studies of a free electron laser in a high gain regime due to the varied undulator parameters were published in 1981. Understanding of the radiation spot size evolution due to the gain and the refractive effects was important for analyzing tapered FELs. The publications on optical guiding by Scharlemann, et al in 1985 [95] and by Sprangle, et al in 1987 [105] are common reference for the optical effects in FELs. Hafizi, et al discussed optimizing tapering to reduce the sideband growth in 1988 and also the relation of optimizing tapering and optical guiding[50, 51] in 1990. They predicted that the amplified signal of 10.6 μm wavelength and 100 W power could be produced at 16% efficiency at 25 m system length, which was ten-fold greater than an un-tapered case.

With the success of the 1986 ELF experiment, the researchers moved to the next phase of using a 25 m undulators system and 44 MeV electron beams to produce high efficiency radiation at 10.6 μm. The experimental results presented in 1989 were not successful, however, only extracting 0.21 GW radiation by 0.97% efficiency due to the electron beam brightness [115]. Their electron beam produced from a 2.5 MeV ATA injector had a normalized emittance of 3 mm-rad. Due in part to the end of the Cold War, the ELF researchers were not

funded to conduct further experiments.

There were some problems inherent in the tapered FELs such as how to keep more electrons trapped, how to find a good tapering strength, and how to produce a good quality input electron beam. Meanwhile, the quality of available input electron beams was tremendously improved with the BNL photoinjector developed in 1986, which generated nC-level of charge electron beams of 5-10 mm-mrad emittance [8].

Tapered FEL experiments were funded by the government as a part of the"Star Wars" program [52]. The "Star Wars" program is another term for the Strategic Defense Initiative (SDI) which aimed to defend against Soviet missile attacks and nuclear weapons using nuclear powered X-ray lasers from the ground or from satellites. The program was initiated by President Ronald Reagan in 1983, influenced by Edward Teller, one of the hydrogen bomb physicists. Because the idea sounded like a science fiction movie and was criticized by many other scientists, the SDI program was called the "Star Wars" program by the media and public. Consecutive experimental results were found to be unsuccessful by 1986, and Teller was also accused of misrepresenting the results. The SDI program spent around 30 billion dollars over ten years without showing immediate results, and eventually was discarded by President Bill Clinton in 1992.

Compounded with the end of the Cold War in 1989 and the end of the "Star Wars" program, supports for tapered FEL research became scarce, and mainly focused in the quest for X-ray FELs. For a long time, there were no more experiments specifically aimed at increasing the extraction efficiency of an FEL.

An essential work in the FEL community was the measurement of the short wavelength self amplified spontaneous emission (SASE) in 1998. While Madey's free electron laser setup was a stimulated emission in which there was a seed laser, the UCLA researchers measured 16 μm radiation from an electron beam of 13 MeV without out a seed laser [54]. The tapered case of SASE FELs was also considered shortly after. In 2001, a GINGER simulation of tapered SASE FELs showed that the efficiency increases by eight times with a resonant

wavelength of 530 nm, an electron beam energy of 217 MeV, and a system length of 20 m, and by 17 times with a resonant wavelength of 0.15 nm, an electron beam energy of 14.3 GeV, and a system length of 200 m [39].

More recent studies about tapering optimization were the numerical studies by Jiao, et al in 2012 in which the three dimensional effects on the radiation spot size were considered [57]. Also, in 2015, a modified KMR model, in which the resonant phase was varied to optimize the tapering, showed that the efficiency could increase to 20% with a radiation wavelength of 4 $\mathring{A}$ and an e-beam energy of 4 GeV. Their modified model showed around two-fold larger efficiency than the increase from the ordinary KMR model [69].

Meanwhile, the completion of the X-ray free electron laser in the Linac Coherent Light Source (LCLS) at wavelengths of 22 to 1.2 $\mathring{A}$ in 2009 was also another great progress in the FEL science [37]. A high brightness, short wavelength, and coherent light source is favorable for many research areas such as molecular imaging, X-ray spectroscopy and X-ray diffraction. Consecutively, there were some efforts to increase the efficiency by tapering, but in the SASE regime it was shown to remain low (at the 0.05%) even with tapering.

At UCLA, researchers have been investigating ways to increase the extraction efficiency for smaller wavelengths, in order to ultimately increase the efficiency of the free electron lasers in the EUV (100-900 $\mathring{A}$) or X-ray range (0.25-100 $\mathring{A}$). Based on a publication by C. Emma, C. Pellegrini, et al in 2015 on increasing the extraction efficiency of a x-ray FEL, the expected maximum efficiency in simulation was 7% at resonant wavelength of 1.5 $\mathring{A}$, electron beam energy of 12.9 GeV, and system length of 100 m[36].

The Nocibur experiment in 2016 by Sudar, Musumeci, et al demonstrated extraction efficiency 30% from a 54-cm-long helical undulator with gap and period tapering, and the electron beams decelerated from 65 to 35 MeV at a resonant wavelength of 10.6 μm [107]. The experimental results motivated the researchers to aim for a smaller wavelength of 257.5 nm in the UV range. The next chapter will discuss the details of the progress in experimental designs.

There have been other high FEL efficiency experiments besides the ones that use single-pass tapered FELs. An FEL oscillator experiment by JLab in 2001 showed 0.7% efficiency at 400 nm [10]. This experiment provided what used to be the highest efficiency achieved in the UV range. Kyoto University FEL (KU-FEL) has made progress over the past years and recently has shown 10% efficiency at 11μm with an FEL oscillator setup.

Figure 1.3 summarizes important high extraction efficiency experiments in different ranges of frequency, with the blue pentagon representing the past single-pass FEL experiments at the point of 2022, with the orange triangle representing the past FEL oscillator experiments, and the green star representing the expected value of the future experiment that will be presented in this document. Ultimately, the aim is to increase the efficiency at highest possible frequency, but the wavelength for the experiment that will be presented in this document will be at 257.5 nm, about a mid-point to the ultimate goal of the program.

1.4 The TESSA scheme

The Tapering Enhanced Stimulated Superradiant Amplification (TESSA) scheme refers to a study that seeks to increase the FEL extraction efficiency by using tapered undulators, prebunched electron beams and a seed laser. While previous literature has studied how to optimize the tapering in various ways, studies about optimizing tapering while using both prebunched electrons and strong intense input seeds are relatively novel.

The term "stimulated" in the acronym refers to the stimulated emission caused by using a seed laser to amplify the FEL radiation. The phenomena of stimulated emission and spontaneous emission in an FEL are similar to those in an optical laser that were predicted by Einstein in 1917. In an optical laser, the bound electrons in an excited state of an atom can spontaneously decay to a lower state, emitting light with the wavelength set by the characteristics of the material (spontaneous emission). When a seed laser with the right wavelength associated with the atomic properties passes through the material, more photons

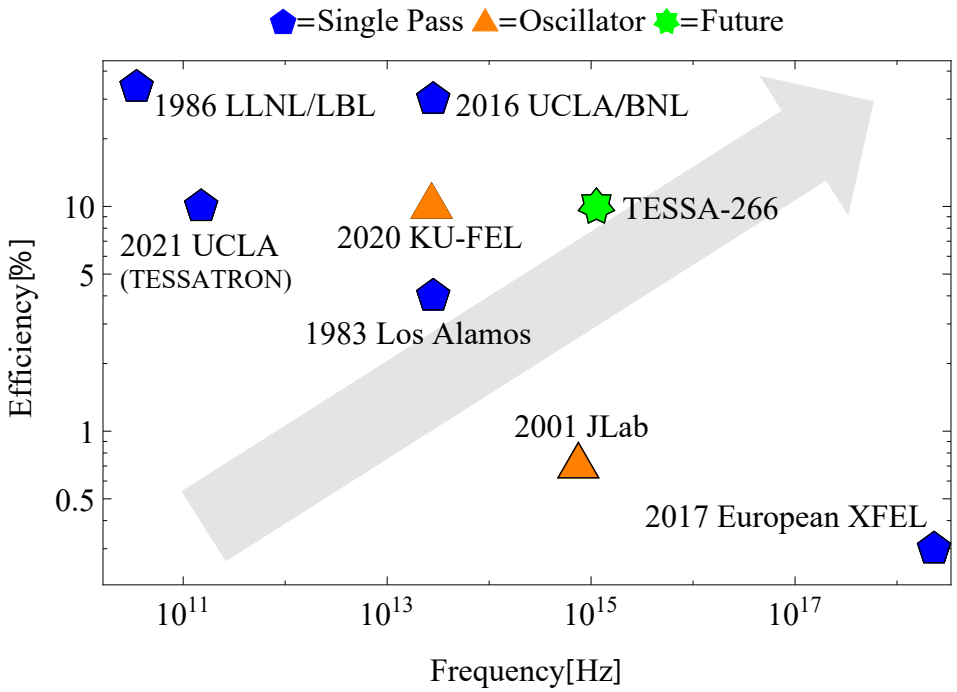

Figure 1.3: FEL extraction efficiency from past experiments. The blue pentagons represent single pass experiments that have been published, and the orange triangles represent oscillator experiments. The green star marks the theoretical results of the TESSA266 experiment (a planned experiment that will be discussed in this document).

will stimulate the emission process (stimulated emission). The phenomenon is similar in a free electron laser. The "free" electrons (as opposed to the bound electrons in an optical laser) passing through an undulator can spontaneously emit radiation due to the motion set by the undulator magnetic field. When a seed laser and electron beams pass through an undulator, based on the relative phase between the radiation and the electrons, the electrons can emit more light (stimulated emission) or absorb the light (absorption). A seed laser is already a necessary component in the TESSA system in order to prebunch the electrons within a short distance, and it also contributes to a higher extraction efficiency as will be shown later in this section.

The TESSA scheme uses a prebunched electron beam to increase the amplification. Prebunching the electrons refers to preparing the electron beam so that more electrons will be in phase with the radiation. While electrons with sufficiently high current passing through a long undulator can "self-bunch" because of the conversion from energy modulation to spatial modulation inherent in the FEL interaction, it is also possible to prepare the electrons within a shorter distance using a short modulator and a magnetic chicane. The coherent, bunched electrons contribute to the radiation intensity by N_e^2 instead of an N_e in spontaneous radiation.

The term "superradiance" has been used since the publication by Dicke in 1954 [25] for optical lasers to describe a system that emit radiation by N_e^2 due to coherence, and term has been used to describe a similar phenomenon in FELs since Bonifacio et al used the term in the 1980s [11]. The nomenclature was actually used when Bonifacio, et al studied the radiation intensity scale of $I \propto N_e^2$ caused by self-bunching instead of prebunching, the authors also indicated that the scale of $I \propto N_e^2$ is "definitory of superradiant-type processes."

The superradiant amplification process in an FEL system can be understood more clearly by A. Gover's theoretical work from 2005, [47, 46], in which the complex spectral energy is expanded in terms of important parameters like the radiation modes, electron phases, and number of electrons. While the amplification process due to bunched electrons is named as

"spontaneous superradiance" or just "superradiant," the presence of bunched electrons and a seed adds an additional amplification process named as "stimulated superradiance." While the superradiant term grows with the number of bunched electrons by N_b^2, the stimulated superradiant term grows with the number of bunched electrons by N_b. The TESSA process is from of both spontaneous superradiance and stimulated superradiance because the electrons enter the undulator prebunched, while there is also a seed that is used to prebunch the electrons and to help the amplification process.

1.5 The applications of high efficiency FELs

Increasing the efficiency of a high brightness, high average power, short wavelength radiation source will have a high impact on the science community and on society. Short wavelength radiation sources are essential components in research areas such as molecular imaging and lithography that are directly related to the advances in science and technology. The short wavelength source also has a potential usage in space technology.

In optical lithography, the resolution in producing the fine circuit patterns is dominated by the wavelength of the light source due to the Rayleigh criterion. A smaller light source will enable a greater number of transistors in an integrated circuit chip. Moore's law describes how the number of transistors used in an integrated circuit doubles every two years (Figure 1.4a). One of the earliest microprocessors was the Intel 4004 made in 1971; the chip had 2.3k transistors made at 10 μm minimum line width ("technology node"). Subsequently, the Pentium chip was made with 3.1 million transistors at 800 nm nodes. Fifty years later, the Apple M1 Max, made in 2021, uses 57 billion transistors made at 5 nm nodes. Figure 1.4b shows different processors produced from the earliest to the most recent.

An important factor in maintaining the trend of Moore's law is having the short wavelength light source necessary in order to develop a microchip with greater precision. As of 2022, the sole supplier of EUV lithography machines is ASML (Advanced Semiconduc-

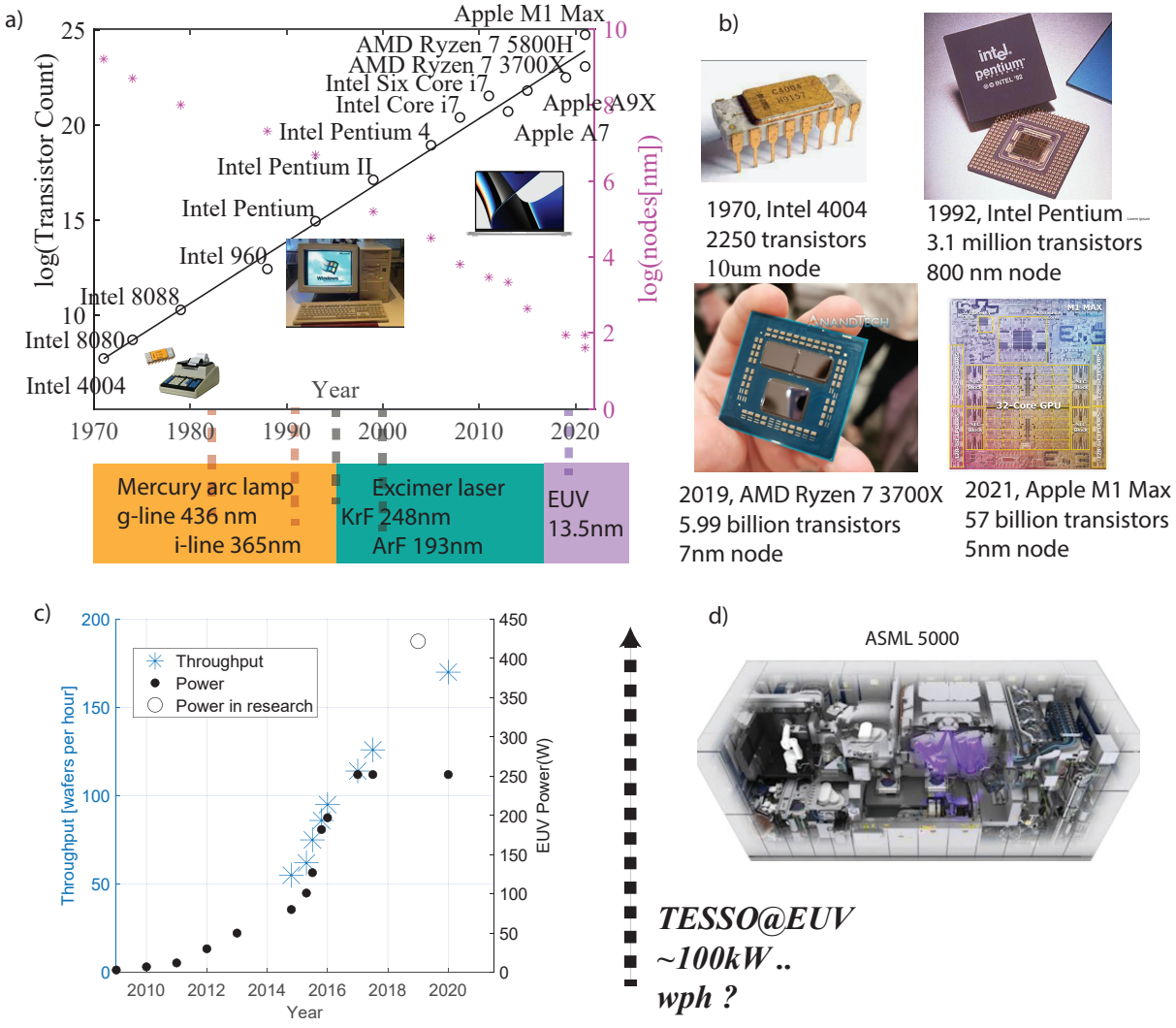

Figure 1.4: a) Moore's law trend shown from the number of transistors in an integrated circuit over the past fifty years b) A comparison of the earliest processors to the most recent shows the drastic improvement of the lithography resolution. The AMD Ryzen 7 3700 series is one of the first computer processors made from the EUVL. c) Average power and productivity (wafer per hour) of ASML EUV lithography systems based on the past presentations [43, 98, 104] d) a picture of ASML EUV lithography systes

tor Materials Lithography). In ASML's EUV lithography machine, using a laser-produced plasma light source generated from tin droplets, the 13.5 nm wavelength and 250 W average power light source can produce microchips with 5 and 7 nm nodes.

The significance of EUV Lithography in current society is self-evident from the company's market value of 270 billion dollars. TSMC has purchased approximately thirty-five of EUVL systems, each of which is worth between 150 and 340 million dollars, from ASML (ASML stated that TSMC had a half of all the ASML EUVL systems in the world as of 2020). Well-known companies such as Apple, AMD, and NVidea have been purchasing microchips from TSMC since 2019, and by 2024 all advanced semiconductor manufacturers such as Intel and Samsung will be producing using EUVLs by 2024 [104].

An important criterion for EUV light sources is the wafer throughput. ASML can produce 125-170 wafers per hour at 250 W (Figure 1.4c-d, [44]). The wafer throughput is related to the power per dose. A dose is the source energy per area, and the scanner takes time to reach the required dose for lithography. Having more photons available in a given time frame and area will increase the productivity. Therefore, a high average power of the light source is essential to increase the wafer throughput; the required dose can be reached within a shorter exposure time. Moreover, transporting the EUV laser requires multiple reflections, which results in a transmittance of around 2% [44], so high average power is essential for EUV lithography. While the EUVL researchers have worked on increasing the average power over the past years and have improved the power in research up to 420 W, the output power of the commercialized product has been 250 W for several years (Figure 1.4c) [98, 73].

A free electron laser oscillator has a great potential as a high average power, short wavelength light source. ASML has increased the average power over the past years by dealing with the inherent problems in the plasma process such as the debris created by the tin droplets, which was limiting the energy conversion [72]. Free electron laser oscillators operate in vacuum and are less prone to have factors that limit increasing the operation frequency. The TESSA program in an oscillator setup is expected to have a high average power in or-

ders of 100 kW [31] as of an initial simulation assessment, far exceeding that of the currently available EUV light sources. A speaker at the EUVL Workshop in 2017 described the TESSA program as a "disruptive technology"[55].

A high brightness, short wavelength, good quality, and high efficiency radiation source has also been a dream in the field of molecular and atomic imaging. The spatial resolution of imaging depends on the wavelength of an incident light. Light sources in x-ray wavelengths allow the resolution of the interatomic spacing. The number of photons per solid angle is related to the imaging resolution because each photon contains diffraction information. Enough photons has be scattered from a sample in order to produce an analyzable diffraction pattern [7]. For example, a protein nanocrystallography required 10^{12} photons per pulse with 10-200 fs pulse length[18], and a single mimivirus particle imaging required 10^{10} photons per pulse with 70 fs pulse length [99].

The pulse length is another important criteria in atomic and molecular imaging. Capturing the atomic or the molecular motion requires an ultra high speed photography time in orders of 100 fs for the atoms, which travel in orders of km/s, and 0.1-1 fs for the electrons, which travel around a hundred times faster than the atoms [22]. Ultrashort pulses also allow capturing the structural information before the sample is destroyed due to radiation damage which takes place within 10 fs. X-ray FELs can produce femtosecond and even sub-femtosecond pulses by different methods, such as shaping the electron bunches. With the combination of the required brightness for imaging and the required pulse length for capturing the image or avoiding significant radiation damage, molecular imaging can require peak power in the range of terawatts [79, 7].

Coherence of light is an important factor in imaging techniques that use phase information. In coherent diffraction imaging, a three dimensional holography of a sample such as biological structure is obtained based on the relative phases. Because a free electron laser radiates light from the deceleration of the trapped electrons, coherence is in inherent feature in FELs. In addition, the wavelength of an FEL can be tuned by changing the beam

energy based on the resonance condition. The wavelength tunability is also beneficial for imaging scientists because they can image at different resolutions of a sample, allowing them to observe both the overall structure and a detailed image.

Consequently, X-ray free electron lasers have been highly beneficial for molecular and atomic imaging due to theirs inherent factors such as the brightness, coherence, tunability, and pulse length. However, most X-ray FEL light sources are available in the city-sized national laboratories usually operated by staffs of hundreds. Improving the efficiency of the short wavelength light sources will increase their availability outside the large-scale laboratories, and can open the way to revolutionary methods of imaging that would allow medical researchers to better help the community.

Lastly, the FEL-based laser ablative propulsion that has been proposed recently shows another way that a high average power light source can become beneficial. In laser ablative propulsion, the laser energy is used to transfer momentum to propel an object instead of ejecting fuels in the opposite direction as in conventional propulsion. By reducing the object mass and increasing energy efficiency, it is possible to reduce the propulsion cost to hundreds of dollars per kilogram from the current cost of several thousands of dollars per kilogram [89].

In laser ablation, short laser pulses are imposed on an object, increasing the surface temperature due to the electron heat transfer. The heated layer due to electron heat conduction causes hydrodynamic expansion within orders of picoseconds. Pure pressure due to photons reflecting on a polished surface is 67 nN/W, but the pressure caused by the interaction of the photons with a layer of special materials such as gold can enhance the thrust to 100μN/W, almost three orders of magnitude larger [87, 88]. The external generation of power is advantageous because the aircraft weight is reduced and the danger from the fuel in the aircraft is also reduced. Although laser ablative propulsion will have a large thrust compared with other external propulsion methods [67, 82], the demonstration of the theory has been limited by the laser power availability. Myrabo, et al demonstrated light-based propulsion of

a 50 gram Lightcraft 71 meters using 10kW pulsed laser (CO2 laser, 1 kJ per pulse) using ablative propellent [78].

Demonstrating light based propulsion of a spacecraft would be more physically realizable with a better light source. Free electron laser oscillator is a good candidate for a high average power available because the pulse energy and the repetition rate are independent. In comparison, conventional diode lasers operate in a medium and the pulse energy decreases as the repetition rate increases [94]. Consequently, Phipps, Musumeci, et al have discussed the possibility of using a free electron laser oscillator setup to launch a 25 kg microsatellite. Given a reasonable set of parameters–1 J energy, 1 ps pulse length, and 1 MHz repetition rate–a series of pulses can be used to heat the surface for propulsion [88].

Alternatively, other recent projects that consider a laser-based propulsion consider using a large quantity of lasers to provide the necessary pulse energy. One example is Breakthrough Starshot (founded by Stephen Hawking, Mark Zuckerberg, Yuri Milner in 2016 [38]) in which an array of a million, kW level lasers would be put in phase to get 100 GW [117]. In addition, Duplay, Higgins, et al from McGill University discuss using an array of 10 meter diameter, 100 MW lasers to reach Mars in 45-days based on laser thermal propulsion technique [28]. While how to control the phase of such number of lasers is beyond the scope of this document, the recent interests of scientists in the space industry show that a high power, high average, and high efficiency light source would have a great impact.

In conclusion, the high efficiency, high average power, short wavelength light source achievable from the TESSA program will be revolutionary for many research areas such as EUV lithography, atomic and molecular imaging, and beam-based space exploration.

.

1.6 Tapered FEL theory using a helical undulator

This section will discuss some of the analytic aspects of the TESSA system that influenced the experimental design. The one-dimensional evolution of electrons in a tapered FEL will be introduced following the previous publications in [62, 108]. Then, the high gain regime of the one dimensional FEL theory will be discussed in a similar manner as previous publications [96, 36]. While the predecessor Nocibur experiment was in a low gain regime in which radiation does not grow significantly through the FEL process, the goal of the TESSA scheme is to amplify the radiation power from a moderate amount of seed and to see the high gain effects. The analytic aspects of a high gain FEL have already been discussed rigorously in past publications [11, 93, 96] and also in more recent UCLA dissertations [108, 34]. For this document, basic analytic studies of the FEL will be re-visited in order to bring attention to some of the key outcomes that influenced the experimental design.

1.6.1 One-dimensional motion of electrons in electromagnetic fields

The Hamiltonian of a charged particle in electromagnetic fields is

$$H_0 = c\sqrt{(\mathbf{P} - \frac{e}{c}\mathbf{A})^2 + m^2c^2} + e\varphi \tag{1.6}$$

where $\mathbf{P} = m\dot{\mathbf{v}} + \frac{e}{c}\mathbf{A}(\mathbf{x})$ is the canonical momentum, $\mathbf{A}$ is the vector potential, and φ is the scalar potential.

The vector potential can be expressed in terms of the vector potential parameters a_w and a_s

$$\begin{aligned} \mathbf{A_w}(z) &= a_w(\hat{x}\cos(\phi_w) + \hat{y}\sin(\phi_w)) \\ \mathbf{A_s}(z) &= a_s(\hat{x}\cos(\phi_s) - \hat{y}\sin(\phi_s)) \end{aligned} \tag{1.7}$$

where $\phi_w = k_w z$ and $\phi_s = k_s z - \omega_s t$.

Force exerted on the electrons follows the Lorentz equation:

$$\frac{d\mathbf{p}}{dt} = \gamma mc\dot{\beta} = e\left[\mathbf{E_s} + \beta \times (\mathbf{B_w} + \mathbf{B_s})\right] \tag{1.8}$$

where $\mathbf{B_w}$ is the field due to the undulator and $\mathbf{B_l}$ is due to the radiation. The on-axis field of a helical undulator can be expressed as:

$$\mathbf{B_w} = \boldsymbol{\nabla} \times A_w = -B_w(\hat{x}\cos k_w z + \hat{y}\sin k_w z), \tag{1.9}$$

where $B_w = a_w k_w$, while the electromagnetic radiation will have helical electric fields and corresponding magnetic fields:

$$\begin{aligned} \mathbf{E_s} &= -\frac{\partial \mathbf{A_s}}{\partial t} = -E_s(\hat{x}\sin(k_s z - \omega t) + \hat{y}\cos(k_s z - \omega t)) \\ \mathbf{B_s} &= \frac{1}{c}\hat{k} \times \mathbf{E_s} = \frac{E_s}{c}(\hat{x}\cos(k_s z - \omega t) - \hat{y}\sin(k_s z - \omega t)), \end{aligned} \tag{1.10}$$

where $E_s = a_s \omega$.

Assuming that magnetic fields due to the undulator dominantly affect the motion of the electrons, the acceleration and the velocity can be expressed as:

$$\dot{\beta} \approx \frac{e}{\gamma mc}\beta \times \mathbf{B}_w = -\frac{eB_w}{\gamma mc}\dot{z}(\hat{x}\sin(k_w z) - \hat{y}\cos(k_w z)). \tag{1.11}$$

The electrons entering the wiggler system can be assumed to have a minimal initial transverse velocity, so

$$\beta_\perp = \frac{K}{\gamma}(\hat{x}\cos(k_w z) + \hat{y}\sin(k_w z)), \tag{1.12}$$

where the undulator vector potential is defined as

$$K = \frac{eB_w}{k_w mc}. \tag{1.13}$$

The longitudinal velocity β_z can be written in terms of the beam energy and K:

$$\beta_z = \sqrt{\beta^2 - (\beta_x^2 + \beta_y^2)} = \sqrt{1 - \frac{1}{\gamma^2} - \frac{K^2}{\gamma^2}} \approx 1 - \frac{1 + K^2}{2\gamma^2} \tag{1.14}$$

assuming $K << \gamma$. Consequently, the electron velocity can be written as:

$$\beta = \hat{x}\frac{K}{\gamma}\cos(k_w z) + \hat{y}\frac{K}{\gamma}\sin(k_w z) + \hat{z}\left(1 - \frac{1 + K^2}{2\gamma^2}\right) \tag{1.15}$$

The undulator vector potential K is usually 1-3 for permanent magnets, while the beam energy is $\gamma = E/mc^2 >> 1$ for the relativistic particles. The flow of energy due to the field can be expressed as

$$\frac{dU}{dt} = \frac{d\gamma mc^2}{dt} = -\mathbf{j} \cdot \mathbf{E_s} = -e\mathbf{v} \cdot \mathbf{E_s}. \tag{1.16}$$

The electron energy equation, assuming a paraxial approximation such that $\frac{\mathrm{d}}{\mathrm{d}t} \simeq v_z \frac{\mathrm{d}}{\mathrm{d}z} \simeq c\frac{\mathrm{d}}{\mathrm{d}z}$, can be written as:

$$\frac{\mathrm{d}\gamma}{\mathrm{d}z} = -\frac{KK_l k_s}{\gamma}(\sin(k_w z)\cos(k_s z - \omega t) + \cos(k_w z)\sin(k_s z - \omega t)). \tag{1.17}$$

where the laser vector potential is defined as

$$K_l = \frac{eE_s}{k_s mc^2}. \tag{1.18}$$

Then, the energy equation can be written as

$$\frac{\mathrm{d}\gamma}{\mathrm{d}z} = -\frac{KK_l k_s}{\gamma}\sin((k_w + k_s)z - \omega t) \tag{1.19}$$

$$\boxed{\frac{\mathrm{d}\gamma}{\mathrm{d}z} = -\frac{KK_l k_s}{\gamma}\sin\theta} \tag{1.20}$$

where θ is the ponderomotive phase defined as

$$\theta := (k_w + k_s)z - \omega t. \tag{1.21}$$

Given that $\omega = ck_s$, the gradient of the ponderomotive phase can be shown as

$$\frac{\mathrm{d}\theta}{\mathrm{d}z} = (k_w + k_s) - \frac{k_s}{\beta_z} = k_w + k_s\left(1 - \frac{1}{\beta_z}\right) \approx k_w - k_s\left(\frac{1+K^2}{2\gamma^2}\right). \tag{1.22}$$

An important outcome of the longitudinal gradient in the ponderomotive phase is that in order for the phase to be constant, the following condition must satisfy

$$\boxed{\lambda_s = \frac{\lambda_w}{2\gamma_r^2}(1+K^2),} \tag{1.23}$$

where λ_s and λ_w are the wavelengths of the laser and the wiggler respectively. This is the resonance condition of the free electron laser system for a helical undulator. The resonant energy of electrons can be written as

$$\gamma_r^2 = \frac{\lambda_w}{2\lambda_s}(1 + K^2). \tag{1.24}$$

Then the derivative of the ponderomotive phase can be written as

$$\boxed{\frac{\partial \theta}{\partial z} = k_w \left(1 - \frac{\gamma_r^2}{\gamma^2}\right)} \tag{1.25}$$

As the electrons decelerate due to the FEL interaction, the energy of the beam decreases. Thus, the consequence of the resonance condition is that adjusting the undulator parameters helps keep more electrons in resonance. When the undulator period is kept constant and the undulator field is adjusted, the change in the undulator parameter K should follow

$$2\gamma \frac{\mathrm{d}\gamma}{\mathrm{d}z} = \frac{k_s K}{k_w} \frac{\mathrm{d}K}{\mathrm{d}z}. \tag{1.26}$$

After substituting the energy relation $\frac{\mathrm{d}\gamma}{\mathrm{d}z}$, the optimal tapering condition for helical undulators is

$$\boxed{\frac{dK}{dz} = -2k_w K_l \sin(\theta_r)} \tag{1.27}$$

where θ_r is the resonant phase. An important aspect of the formula is that K_l depends on the field intensity E_s. At a low-gain regime in which the radiation field intensity does not change significantly, K_l can be kept constant while determining the tapering. When the seed laser starts at a moderate amount and the tapering is optimized, the interaction enters a high-gain regime in which the radiation field intensity grows significantly. In this case, in the Eq. 1.27 one must take into account the change in the field intensity for determining an optimal tapering.

1.6.2 Phase space representation

In order to examine the interaction between electrons and radiation, one can consider the phase space with the coordinates of electron energy γ and ponderomotive phase θ. KMR derives the conserved quantity in the phase space of (θ,γ) from the Hamilton's equations found from the Hamiltonian of a charged particle in electromagnetic fields as in Equation 1.6. The conserved quantity can also be determined based on the longitudinal gradients found from the energy flow and Lorentz equations:

$$\begin{aligned} \frac{\partial H}{\partial \theta} &= -\dot{\gamma} = c\frac{KK_l k_s}{\gamma}\sin\theta \\ \frac{\partial H}{\partial \gamma} &= \dot{\theta} = c\left(k_w - k_s\left(\frac{1+K^2}{2\gamma^2}\right)\right). \end{aligned} \tag{1.28}$$

$$H = k_w\gamma + \frac{k_s}{2\gamma}(1+K^2) - \frac{KK_l k_s}{\gamma}\cos\theta. \tag{1.29}$$

In order to describe electron motion with energy near the resonant energy, one can define a new canonical momentum:

$$\gamma = \delta\gamma + \gamma_r \tag{1.30}$$

where $\gamma_r^2 = \frac{\lambda_w}{2\lambda_s}(1+K^2)$ is the resonant energy. The Hamiltonian of electrons near resonance will have an additional factor

$$\begin{aligned} H_1 &= H + \theta\frac{\mathrm{d}\gamma_r}{\mathrm{d}z} \\ H_1 &= k_w(\delta\gamma+\gamma_r) + \frac{k_s(1+K^2)}{2(\delta\gamma+\gamma_r)} - \frac{KK_l k_s}{\delta\gamma+\gamma_r}\cos\theta - \frac{KK_l k_s}{\delta\gamma+\gamma_r}\theta\sin\theta_r \\ &= k_w\gamma_r\left(1+\frac{\delta\gamma}{\gamma_r}+\frac{1}{1+\frac{\delta\gamma}{\gamma_r}}\right) - \frac{KK_l k_s}{\gamma_r}(\cos\theta+\theta\sin\theta_r)\left(1+\frac{\delta\gamma}{\gamma_r}\right)^{-1}. \end{aligned} \tag{1.31}$$

which can be approximated as

$$H_1 \approx \frac{k_w}{\gamma_r}\delta\gamma^2 - \frac{KK_l k_s}{\gamma_r}(\cos\theta+\theta\sin\theta_r). \tag{1.32}$$

The Hamiltonian is now in a more familiar form similar to that of a pendulum in the classical physics and that of an RF system in the accelerator physics. The latter term

$$F = -\frac{KK_l k_s}{\gamma_r}(\cos\theta + \theta\sin\theta_r) \tag{1.33}$$

is considered as the ponderomotive potential with local minima at $\theta_{rn} = \theta_r + 2\pi n$ and local maxima at $\theta_1 = \pi\mathrm{sgn}(\theta_r) + \theta_r + 2\pi n$. The term "ponderomotive" has been used since at least the 1850's to describe the nonlinear system of charged particles in oscillatory electromagnetic fields. The local troughs of the ponderomotive potential will trap the particles like buckets in which the particles will circulate in a closed orbit. The phenomenon is similar to the bound, oscillatory solution and unbound, rotating solution of a pendulum. A separatrix is a boundary that separates the bound and the unbound solutions of a nonlinear system. The Hamiltonian is constant on the separatrix, so a solution $H_{1,0} = H_1(\theta = \theta_1, \gamma = 0)$ at which the phase is at the edge of a bucket can be used to solve for the energy in terms of the ponderomotive phase.

$$H_{1,0} = -\frac{KK_l k_s}{\gamma_r}(-\cos\theta_r + (\pi\mathrm{sgn}(\theta_r) + \theta_r)\sin\theta_r) = H_1(\theta, \delta\gamma) \tag{1.34}$$

$$\delta\gamma^2 = \frac{KK_l k_s}{k_w}(\cos\theta + \theta\sin\theta_r + \cos\theta_r - (\pi\mathrm{sgn}(\theta_r) + \theta_r)\sin\theta_r) \tag{1.35}$$

The energy at the separatrix can therefore be written as

$$\delta\gamma = \pm\sqrt{\frac{KK_l k_s}{k_w}(\cos\theta + \cos\theta_r + (\theta - (\pi\mathrm{sgn}(\theta_r) + \theta_r))\sin\theta_r)} \tag{1.36}$$

Figure 1.5 illustrates the ponderomotive potentials and the separatrices plotted at different resonant phases. A resonant phase close to zero has a larger separatrix, and this means there is a larger area to trap the electrons. The colored region in (a) illustrates the potential well where the electrons get trapped. The size of the separatrix decreases as the resonant phase increases. It is possible to compute the bucket width, height, and area of the separatrix at different resonant phases, and such bucket parameters are associated with an

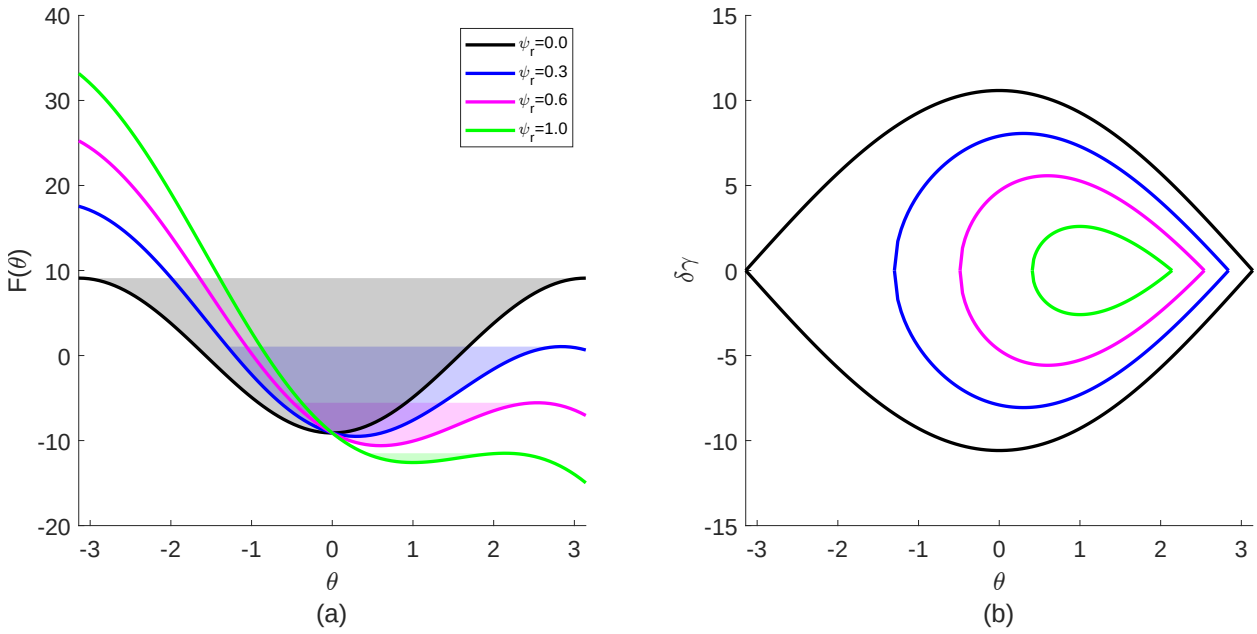

Figure 1.5: The ponderomotive potentials (a) and the separatrices (b) at different resonant phases.

expected trapping fraction. A larger resonant phase increases the tapering gradient as shown in Equation 1.27 and could sometimes help the deceleration. Meanwhile, the larger resonant phase makes the bucket size smaller, and the smaller bucket size causes a smaller trapping fraction, detrapping more particles within the same distance. While the bunched electron could fit in a separatrix with a resonant phase around 0.6-0.8, an ideal resonant phase for the best extraction efficiency is not as obvious. The next chapter will further discuss about the optimization of the resonant phase for the TESSA system.

The separatrix curve was a crucial factor in analyzing the optimal tapering because the field experienced by the trapped particles should be taken into account while considering the best tapering. The resonant phase influences the bucket size and the tapering strength, so it is an important parameter in the tapering optimization.

1.6.3 Electromagnetic wave dynamics in the high-gain FEL regime

The basic characteristics of the FEL interaction can be shown in one-dimensional theory in which the transverse effects are ignored. While the transverse effects are important for obtaining the final energy and the power, a one-dimensional treatment still shows some of the key factors that affect the design studies. This section will re-visit the high gain regime of 1D FELs which has been discussed in previous publications [11, 93, 96, 36, 34]. The high gain regime refers to a case when the radiation field grows significantly as an electron beam passes through the undulator. In the TESSA system, prebunched electrons and a moderate amount of seed passing through a strongly tapered undulator quickly lead to high-gain regime. The electromagnetic wave equation for an electric field in the presence of a current density is used to calculate the effects of the field growth:

$$\left[\nabla^2 - \frac{1}{c^2}\frac{\partial^2}{\partial t^2}\right]\mathbf{E}(\vec{r},t) = \mu_0\frac{\partial \mathbf{j}}{\partial t} + \frac{1}{\epsilon_0}\nabla\rho \tag{1.37}$$

As shown earlier, the electric field due to the radiation is dominantly transverse like the vector potential due to the seed. For helical undulators it is preferable to replace the Cartesian basis vectors by the complex conjugate pairs $\hat{e}_\pm = \frac{1}{\sqrt{2}}(\hat{e}_1 \pm i\hat{e}_2)$.

$$\begin{aligned}\vec{E}_\perp(z,t) &= (\tilde{E}_x\hat{x} + \tilde{E}_y\hat{y})e^{i(kz-\omega t)}\\ \vec{E}_\perp(z,t) &= (E_+\hat{e}_+ + E_-\hat{e}_-)e^{i(kz-\omega t)},\end{aligned} \tag{1.38}$$

where $E_\pm = \frac{1}{\sqrt{2}}(E_x \mp iE_y)$. It can be shown by substitution that the wave equation in terms of the complex amplitude is

$$\left[\frac{\partial^2}{\partial z^2} - \frac{1}{c^2}\frac{\partial^2}{\partial t^2}\right]E_\pm(z,t) = \mu_0\frac{\partial j_\pm}{\partial t}. \tag{1.39}$$

When the electric field slowly grows in longitudinal direction while oscillating in time, the complex amplitudes of the transverse electric field can be written as

$$E_\pm(z,t) = \frac{1}{\sqrt{2}}(E_x \mp iE_y) = i\frac{1}{\sqrt{2}}\tilde{E}_\pm(z)e^{\pm i(k_s z-\omega t)}. \tag{1.40}$$

The magnitude of the transverse current can be approximated based on its dependence on the charge density and the transverse velocity, which can be written as

$$j_{\pm} = \rho(\mathbf{r}) v_{\pm} \tag{1.41}$$

where $v_{\pm}$ is the transverse velocity in the complex basis vectors. Given the transverse electric field and the velocity that were derived in the previous section, the complex amplitudes of the transverse velocity are

$$v_{\pm}(z) = \frac{1}{\sqrt{2}}(v_x \mp i v_y) = \frac{K}{\gamma\sqrt{2}} e^{\mp i k_w z}. \tag{1.42}$$

The results indicate that the transverse velocity rotates counter-clockwise, or the left-hand circular direction, while the transverse electric field rotates clockwise, or the right-hand circular direction. These directions have been chosen so that the change in the electron energy would be negative; a different polarization would have described a system in which the particle energy oscillates rapidly in z, resulting with no energy loss on average or a system in which the particle energy increases in z.

Then, the wave equation can be written as

$$\left[2ik_s \tilde{E_{\pm}}' + \tilde{E_{\pm}}''\right] = -\sqrt{2} i \mu_0 \frac{\partial j_{\pm}}{\partial t} \exp[\mp i(k_s z - \omega_s t)]. \tag{1.43}$$

The fact that electric field growth is not outstandingly rapid allows us to use the slow varying envelope approximation (SVEA) in which the amplitude and the slope of the amplitude do not change significantly within one radiation wavelength:

$$\begin{aligned} |\tilde{E_{\pm}}'|\lambda_s << |\tilde{E_{\pm}}| \qquad & |\tilde{E_{\pm}}''|\lambda_s << |\tilde{E_{\pm}}'| \\ |\tilde{E_{\pm}}'| << k_s|\tilde{E_{\pm}}| \qquad & |\tilde{E_{\pm}}''| << k_s|\tilde{E_{\pm}}'|, \end{aligned} \tag{1.44}$$

from which the wave equation can be written as

$$\frac{\partial \tilde{E}_{\pm}}{\partial z} = \sqrt{2} \frac{\mu_0}{2k_s} \frac{\partial j_{\pm}}{\partial t} \exp[\mp i(k_s z - \omega_s t)]. \tag{1.45}$$

In the TESSA system, the electrons are prebunched by the prebuncher system. The electrons gain density modulation as they interact with the seed laser in the modulator, which is a shorter version of the TESSA undulator with the same undulator period. Therefore, the number density and the charge density will have a density modulation at the undulator entrance. The charge density of the electrons can be written as

$$\rho = \rho_0 - \frac{e}{(2\pi)^{3/2}\sigma_x^2\sigma_z}\sum_{j=1}^{N_e} e^{-i\phi_j} \tag{1.46}$$

where ρ_0 is the uniform charge density and the next term is the modulated charge density. While there would be a total number of eN_e in a Gaussian volume with transverse and longitudinal rms beam size σ_x and σ_z if all particles were in phase, the density is modulated according to the radiation wavelength by $\phi_j = (k_s z_j - \omega_s t)$. The transverse current density can be expressed

$$j_\pm = \rho_0 c - \frac{eK}{(2\pi)^{3/2}\sigma_x^2\sigma_z\sqrt{2}}\sum_j^{N_e}\left(\frac{e^{\mp i(k_s z_j - \omega_s t)}}{\gamma_j}\right) e^{\mp i k_w z}\delta(z - z_j) \tag{1.47}$$

The density modulation of the particles causes temporal dependence in the bunch current density, where the time-derivative of the bunch current is

$$\frac{\partial j_\pm}{\partial t} = \pm i\omega_s\frac{eK}{(2\pi)^{3/2}\sigma_x^2\sigma_z\sqrt{2}}\sum_j^{N_e}\left(\frac{e^{\mp i(k_s z_j - \omega_s t)}}{\gamma_j}\right) e^{\mp i k_w z}\delta(z - z_j). \tag{1.48}$$

The slowly varying envelope approximation implies that averaging over a short distance like a undulator period will not influence the system. The wave equation can be written as

$$\left.\frac{\partial \tilde{E}_\pm}{\partial t}\right|_{SVEA} = \mp i\frac{\mu_0\omega_s}{2k_s}\frac{eK}{(2\pi)^{3/2}\sigma_x^2\sigma_z}\sum_j^{N_e}\frac{e^{\mp i((k_s+k_w)z - \omega_s t)}}{\gamma_j}. \tag{1.49}$$

In terms of the peak current of a Gaussian distribution $I = \frac{eN_e}{\sqrt{2\pi}\sigma_z}$, the above can be written as

$$\left.\frac{\partial \tilde{E}_\pm}{\partial t}\right|_{SVEA} = \mp i\frac{\mu_0\omega_s}{2k_s}\frac{KI}{2\pi\sigma_x^2}\sum_j\frac{e^{\mp i((k_s+k_w)z - \omega_s t)}}{\gamma_j}. \tag{1.50}$$

Taking the real part of the field, the above can be written as

$$\boxed{\frac{\partial \tilde{E}_{\pm}}{\partial z} = \mp c_2 \frac{KI}{\sigma_x^2} \left\langle \frac{\sin\theta_j}{\gamma_j} \right\rangle} \tag{1.51}$$

where $c_2 = \frac{1}{4\pi\epsilon_0 c}$.

1.6.4 Extraction efficiency computed from the 1D FEL Equations

The electromagnetic interaction between electrons and radiation can be described by the particles energies γ and the ponderomotive phases θ and the electric field complex amplitude $E_{\perp}$. A summary of the assumptions that have been made for the one-dimensional analysis is: (1) the electrons arrive at the undulator without initial transverse velocities, dominantly moving in the longitudinal direction, (2) the vector potentials of the undulator and the radiation are independent of the transverse coordinates, (3) the electron beam size and radiation spot size are ideal for FEL interaction, ignoring the diffraction and refraction effects of the radiation, (4) the radiation field grows slowly compared to the radiation and the undulator wavelength, allowing the slowly varying amplitude assumption, (5) the electrons arrive bunched with the density modulation periodic in the resonant wavelength.

Based on these assumptions, the evolution of j-th electrons and the radiation at position z can be written as:

$$\begin{aligned}
&\frac{\partial \gamma_j}{\partial z} = -c_1 KE \sin(\theta_j) \quad \text{phase modulation and radiation} \rightarrow \text{energy modulation} \\
&\frac{\partial \theta_j}{\partial z} = k_w \left(1 - \frac{\gamma_r^2}{\gamma_j^2}\right) \quad \text{energy modulation} \rightarrow \text{phase modulation} \\
&\frac{\partial E}{\partial z} = -\frac{c_2}{\sigma_e^2} KI \left\langle \frac{\sin\theta_j}{\gamma_j} \right\rangle \quad \text{phase and energy modulation} \rightarrow \text{field growth,}
\end{aligned} \tag{1.52}$$

where $c_1 = \frac{e}{m_e c^2}$ and $c_2 = \frac{1}{4\pi\epsilon_0 c}$. The equations show how the ponderomotive phase θ_j and the energy γ_j of the electrons and the radiation E interact to amplify the FEL light.

From the initial total energy of electrons $U_o = N_e \gamma_0 m_e c^2$, the electrons lose energy as they pass through the undulator. Only the electrons that remain trapped in the separatrix remain in resonance with the electromagnetic field and contribute to the radiation.

Consequently, the FEL extraction efficiency can then be written as

$$\eta = \frac{\Delta U_1}{U_o} = \frac{1}{\gamma_0}\int_0^{L_w} f_t(z)\frac{\mathrm{d}\gamma(z)}{\mathrm{d}z}dz \tag{1.53}$$

where $f_t(z)$ is the trapping fraction at position z. The average energy of the trapped electrons that participate in the FEL interaction can be approximated as the resonant energy as if the system is a single particle with energy γ_r and phase θ_r, which is referred to as the "resonant particle approximation (RPA)" [69]. Then, the rate of the decrease in the electron energy can be approximated as the rate of the decrease in the resonant energy

$$\begin{aligned} \frac{\mathrm{d}\gamma}{\mathrm{d}z} &\approx \frac{\mathrm{d}\gamma_r}{\mathrm{d}z} \\ \frac{\mathrm{d}\gamma}{\mathrm{d}z} &\approx -\frac{KK_lk_s}{\gamma}\sin\theta_r = -\frac{eK}{mc^2}\frac{E(z)}{\gamma_r}\sin\theta_r. \end{aligned} \tag{1.54}$$

Then, the FEL extraction efficiency can be approximated as

$$\eta \approx \frac{1}{\gamma_0}\frac{e}{mc^2}\sin(\theta_r)\int_0^{L_w}\frac{f_t(z)K(z)E(z)}{\gamma_r(z)}dz. \tag{1.55}$$

We will consider a simple case when the resonant phase is constant throughout the interaction. This assumption should not affect the system significantly because even in the three-dimensional FEL simulation the constant resonant phase showed sufficient amount of amplification. The equations with the resonant phase approximation with the constant resonant phase in the case of as tapered FEL can be written as

$$\begin{aligned} \frac{\mathrm{d}K}{\mathrm{d}z} &= -\xi_1 E & \xi_1 &= \frac{2}{m_e c^2}\frac{k_u}{k_s}\sin\psi_r \\ \frac{\mathrm{d}\gamma_r}{\mathrm{d}z} &= -\xi_2\frac{KE}{\gamma_r} & \xi_2 &= \frac{e}{m_e c^2}\sin\psi_r \\ \frac{\mathrm{d}E}{\mathrm{d}z} &= \xi_3\frac{K}{\gamma_r} & \xi_3 &= \frac{1}{4\pi\epsilon_0 c}\frac{f_t I}{\sigma_x^2}\sin\psi_r = c_2\frac{f_t I}{\sigma_x^2}\sin\psi_r \end{aligned} \tag{1.56}$$

where $\frac{\mathrm{d}\theta_r}{\mathrm{d}z}$ is zero assuming RPA $\gamma \sim \gamma_r$, and a fraction of the electrons trapped in the separatrix f_t contribute to the change in the radiation. The equations written in the above format show how the important parameters $K(z), \gamma_r(z)$, and $E(z)$ influence each other in the RPA approximation.

We will now make additional assumptions to extract simple scalings for the system efficiency. We will consider a case where the ratio of $\frac{K}{\gamma_r} \equiv \frac{K_0}{\gamma_0} \equiv s_0$ is a constant and the trapping fraction is a constant. This technically implies that the electric field grows linearly in z based on the above equations. It will be shown that the field growth in the TESSA system will be much more complicated, but we do see in the three-dimensional FEL simulation an initial region where the field appears to grow linearly. Eventually, the growth is hindered as the 3D transverse effect become dominant. In a system with tapering optimization (discussed in chapter 2), $\frac{K}{\gamma}$ is initially $\cong 0.007$ and decreases by 10 % throughout the system. The trapping fraction also decreases over z in a real system. In the case that s_0 and f_t are constant in the longitudinal distance, we can see that

$$\begin{aligned} \frac{\mathrm{d}\gamma_r}{\mathrm{d}z} &= -\xi_2 s_0 E \\ \frac{\mathrm{d}E}{\mathrm{d}z} &= \xi_3 s_0 \end{aligned} \tag{1.57}$$

and integrating the field,

$$E(z) = \xi_3 s_0 z + E_0 \tag{1.58}$$

we can write the efficiency as

$$\begin{aligned} \eta &= \frac{f_t}{\gamma_0}\xi_2 s_0 \int_0^{L_w} E(z)dz \\ \eta &= \frac{f_t}{\gamma_0}\xi_2 s_0 \int_0^{L_w} (\xi_3 s_0 z + E_0)dz \\ \eta &= \frac{f_t}{\gamma_0}\xi_2 s_0 \big(E_0 L_w + \xi_3 s_0 L_w^2\big) \end{aligned} \tag{1.59}$$

The initial field intensity shown here can be written as $E_0 = \sqrt{\frac{P_0 Z_0}{2\pi\sigma_s}}$ where σ_s is the radiation spot size, so the electric field can be written as

$$E(z) = \frac{f_t I}{8\pi\epsilon_0 c}\frac{1}{\sigma_x^2}\frac{K_0}{\gamma_0} z \sin\psi_r + E_0, \tag{1.60}$$

and the 1D FEL efficiency can be written as

$$\begin{aligned}\eta(z) &= \frac{f_t}{\gamma_0}\left(\frac{e}{m_e c^2}\sin(\psi_r)\frac{K_0}{\gamma_0}\right)\left(zE_0 + z^2\frac{K_0}{\gamma_0}\frac{f_t I}{8\pi\epsilon_0 c\sigma_x^2}\sin\psi_r\right)\\ \eta(z) &= f_t\frac{e}{m_e c^2}\frac{K_0}{\gamma_0^2}E_0 z\sin(\psi_r) + z^2\frac{K_0^2}{\gamma_0^3}f_t^2\frac{I}{8\pi\epsilon_0 c\sigma_x^2}\frac{e}{m_e c^2}\sin^2(\psi_r).\end{aligned} \tag{1.61}$$

The equations show the basic contribution of the seed laser $E_0 z$ to the efficiency in the first part and the $N_t z^2$ dependent high gain term in the second part. One important relation that is shown in this equation is that the superradiant contribution is larger with smaller beam size by a factor of an inverse-square. The above equation can be used to find the output radiation power because the FEL efficiency is

$$\eta(z) = \frac{P_{\text{rad}} - P_0}{P_{\text{beam}}} \tag{1.62}$$

$$P_{\text{rad}}(z) = P_0 + \eta(z)P_{\text{beam}} = P_0 + \eta(z)N_e\gamma_0 m_e c^2 \tag{1.63}$$

$$P_{\text{rad}} = P_0 + \frac{f_t N_e e K_0}{\gamma_0}\sqrt{\frac{P_0 Z_0}{2\pi\sigma_s}}\sin(\psi_r)z + f_t^2 N_e^2\frac{1}{\sqrt{2\pi}\sigma_z\sigma_x^2}\frac{1}{8\pi\epsilon_0 c}\frac{K_0^2}{\gamma_0^2}\sin^2(\psi_r)z^2. \tag{1.64}$$

Radiation power scales by N_e^2 as expected for a superradiant system.

Figure 1.6 shows visualizations of the 1D efficiency obtained in Equation 1.61. The trapping fraction and the resonant phase are fixed at 0.26 and 0.65 respectively, in order to match the 1D-efficiency with the efficiency obtained from the 3D simulation that is discussed in the next chapter. The electron beam size matched to the undulator natural focusing changes with K, so a ratio to the matched beam size was plotted. The electron beam energy is varied to match the resonance condition while the resonant wavelength and the undulator period are fixed at 257.5 nm and 32 mm respectively. The efficiency grows by inverse-square of the beam size, so smaller electron beam size improves the efficiency significantly. Figure 1.6b shows how the 1D efficiency varies with the undulator vector potential and the resonant wavelength. The electron beam energy is varied in order to match the resonance condition, while the undulator period is fixed at 32 mm. The plot shows that the efficiency decreases with the smaller resonant wavelength, which poses some challenges to the TESSA program aiming at smaller resonant wavelengths.

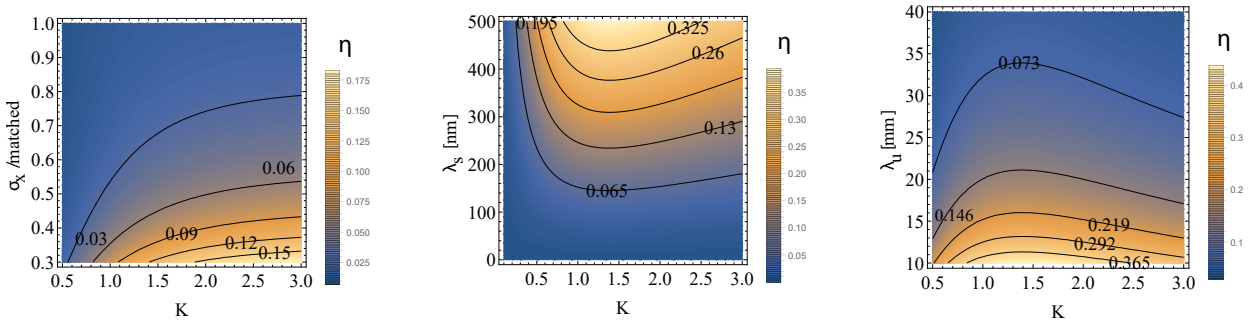

Figure 1.6: Visualization of 1D radiation efficiency and power (Equations 1.61,1.64) estimated at f_t=0.3 and ψ_r=0.7. (a) Energy efficiency is plotted by varying the undulator parameter K and the electron transverse beam size. The transverse beam size is varied in comparison to the matched beam size at the given undulator parameter K. The resonance condition is matched by varying the beam energy with the undulator parameter, while the radiation wavelength is kept constant at 257.5 nm and the undulator period at .032 m. The efficiency is increased significantly with the smaller beam size, while the K strength also increases the efficiency. This is because the efficiency depends on the beam size by inverse-square. (b) The efficiency is plotted while varying the resonant wavelength and the electron beam energy. The undulator vector potential is also varied to match the resonant condition at the given radiation wavelength and beam energy, while the undulator period is kept constant at .032 m. (c) The efficiency is plotted while varying the undulator period and the undulator vector potential, while the beam energy is varied by the resonance condition. The resonant wavelength is kept constant at 257.5 nm.

1.6.5 The 3D effects on a strongly tapered system

The one-dimensional analysis that has been discussed in this chapter ignored important transverse effects of electron beam and radiation spot sizes. Since the tapering the FEL was first discussed in 1980's, extensive discussion regarding the relation between optimal tapering and optical guiding have continued [62, 95, 105, 57, 70]. For the main simulation studies discussed in this document we used a three-dimensional FEL code to compute the optimal tapering instead of the analytical studies involving the optical effects. This section will still introduce the basic concepts about the transverse effects that were neglected in the previous sections. The wave equation for the radiation field should contain the effects of the electron beam acting as a refractive medium

$$\left(\nabla^2 - \frac{n^2}{c^2}\frac{\partial}{\partial t}\right)\mathbf{E} = \mu_0 \mathbf{J} \tag{1.65}$$

which is in the paraxial wave equation

$$\nabla_\perp^2 E + 2ik_s\frac{\partial E}{\partial z} = k_s^2(1 - n^2(r_\perp, z))^2)E. \tag{1.66}$$

The index of refraction n due to the refractive effects of the electron beam [105]

$$n = 1 + \frac{1}{2}\frac{\omega_{b0}^2}{\omega_s^2}\left(\frac{r_{b0}}{r_b(z)}\right)^2 e^{-r^2/r_b^2(z)}\left\langle\frac{e^{-i\psi}}{\gamma}\right\rangle \tag{1.67}$$

$r_b(z)$ represent the final and the initial electron beam radius, $r_{b0} = r_b(0)$, $\omega_{p0} = \sqrt{\frac{4\pi n_{e0}e^2}{m_e}}$ is the initial plasma frequency, $a_w = \frac{eB_w}{k_w mc^2}$ and $a_s = \frac{eE_s}{k_s mc^2}$ are the normalized vector potentials of the undulator and the radiation field, ψ is the electron ponderomotive phase, and γ is the beam energy. The index of refraction can also be written as [95]

$$\begin{aligned} \Re(n) - 1 &= \frac{1}{k}\frac{\mathrm{d}\psi}{\mathrm{d}z} &&= \frac{2\pi e J a_w}{mc^3 a_s}\left\langle\frac{\cos\psi}{\gamma}\right\rangle \\ -\Im(n) &= \frac{1}{ka_s}\frac{\mathrm{d}a_s}{\mathrm{d}z} &&= \frac{2\pi e J a_w}{mc^3 a_s}\left\langle\frac{\sin\psi}{\gamma}\right\rangle \end{aligned} \tag{1.68}$$

where J is the current density. The authors followed the equations derived in [90]. The real part of the refractive index describes the refractive guiding, while the imaginary part

describes the gain focusing. Sprangle, et al. derived an envelope equation for the radiation beam based on the Laguerre polynomials obtained from the wave equation

$$r_s'' + K^2 r_s = 0 \tag{1.69}$$

where K can be written as [57]

$$K^2 = \frac{4}{k_s^2 r_s^4}\left(-1 + V^2 G + \frac{1}{4}V^4 G^2 \frac{\langle \sin\psi \rangle^2}{\langle \cos\psi \rangle^2} + \frac{1}{4}k_s r_s^2 \langle \sin\psi \rangle \frac{\mathrm{d}}{\mathrm{d}z}\left(\frac{V^2 G}{\langle \cos\psi \rangle}\right)\right) \tag{1.70}$$

where

$$V^2 = (n^2 - 1)k_s^2 r_b^2 \tag{1.71}$$

is the refractive guiding fiber parameter,

$$G(z) = \frac{1-f}{(1+f)^2}, \quad f(z) = \left(\frac{r_b}{r_s}\right)^2 \tag{1.72}$$

is a ratio of the filling factor $f(z)$. In a tapered FEL, the system soon reaches a regime in which the real part reaches 1 while the imaginary part reaches 0. In this case, fiber parameter can be approximated as [57]

$$V^2 \approx \frac{\omega_{p0}^2 r_{b0}^2}{c^2}\frac{a_w}{a_{s0}}\frac{\langle \cos\psi \rangle}{\gamma_r}. \tag{1.73}$$

Because the above are still in the linear regime, they are not applicable for the radiation growth in the TESSA system. Because the strongly tapered, prebunched, high-gain FEL system is challenging to solve analytically, we exploit the modern computing resources available to optimize the extraction efficiency.

1.7 Simulation Tools

While the one-dimensional approach could provide an initial approximation of a system, the FEL interaction between electron beam and radiation in a strongly tapered undulator should involve longitudinal and transverse evolution of particle dynamics. The work presented in this document mainly used GENESIS simulation[92] to evaluate the FEL interaction for the design studies. The input distribution for the FEL was simulated using ASTRA[42] and ELEGANT[13]. The undulator design used RADIA[19] simulation to compute the on-axis field from a three-dimensional magnetic design.

1.7.1 Genesis

GENESIS is a time-dependent three-dimensional code used to simulate free-electron lasers[92]. The electron beam in this simulation is a set of macroparticles, each with six-dimensional phase space coordinates. The simulation evolves the beam according to the ponderomotive phase $\theta = (k + k_w)z + \omega t$. Along with the ponderomotive phase, the beam energy γ, the transverse positions x and y, and the transverse momenta p_x and p_y are evolved at every integer multiple of an undulator period. The longitudinal coordinates are evolved by the fourth order Runge Kutta method, while the transverse coordinates are evolved by the first order matrix multiplication. The radiation is defined on a mesh and is evolved at an integer multiple of an undulator period according to the radiation field equation $\nabla_\perp^2 + 2ik(\frac{\partial}{\partial z} + \frac{1}{c}\frac{\partial}{\partial t} = S$. The code uses the Crank-Nicholson scheme, which is a finite difference method that is more numerically stable than other explicit or implicit methods.

The script reads an input seed as a single numeric input or as a time-dependent profile defined at every slice. A user can define a series of undulator vector potentials K and quadrupole gradients at each undulator period in a magnetic lattice. Because the code is limited to calculating the evolution at each undulator period, the magnetic lattice should also be set at every undulator period. The simulation consequently deviates from a physical

setup if the element length is not a multiple of an undulator period. As of the version 1.3 which was used, the simulation does not allow a bending magnet as an input, so a chicane has to be treated externally. The newer version written in C++ has a dipole option, but this was not used for the project discussed in the document.

The parameter DGRID sets the grid size of the radiation field, while the parameter NCAR sets the number of grid points. The total number of a radiation mesh is therefore NCAR^2. In the TESSA simulation, DGRID was set to 3 mm with *ncar* of 151. The transverse variables of a GENESIS simulation without an input distribution can be set to a Gaussian, uniform, or parabolic distribution by an input parameter ITGAUS. The parameter was usually set to an uniform distribution for the time-independent simulations that are presented in this document, while the time-dependent simulations used an input distribution that does not require this parameter.

In GENESIS simulation, the temporal profiles are determined by the slices, in which the first slice of a temporal distribution represents the tail of a bunch. The simulation can also read an input distribution with x, y, px, py, t, p, in which a smaller t represents the tail of a bunch. The head of the bunch in this convention arrives earlier at a given position than the tail, and has a larger t. The conventions in ELEGANT and GENESIS are opposite to each other, so the bunch has to be reversed to move between the two simulations. The parameter NTAIL is used to determine the first simulated slice, in which a distribution can be shifted towards the tail by a negative integer or towards the head by a positive integer. The parameter IOTAIL suppresses the slippage length at a value of zero and outputs the entire distribution at one. The next chapter discusses how the time-dependent mode of GENESIS was used to study the effects of the pre-optimized tapering.

1.7.2 GIT

Genesis Informed Tracking simulation (GIT)[1] is a Matlab code that reads GENESIS output to compute the best tapering for the next period. The simulation calculates the tapering using Equation 1.27 based on the field intensity calculated from the GENESIS field distribution and the separatrix calculated from Equation 1.34. In a low gain regime, the parameter K_L in Equation 1.27, which depends on the electric field does not change significantly, so the optimal tapering can be approximated more easily. Meanwhile, in a high gain regime, the field magnitude evolves over the longitudinal distance so the optimal tapering cannot be found without knowing the field at each period. Therefore, the GENESIS simulation is run for an undulator period, from which the laser vector potential is calculated. Then, the optimal tapering calculated in the code is fed into the next period.

The code makes it possible to find a good tapering scheme without calculating a K vs. z fit analyzed from the FEL equations as discussed in some of the previous tapering studies [57, 69]. More optimization of the FEL parameters still helps in increasing the extraction efficiency. The studies of the tapering optimization are presented in the next chapter.

1.7.3 Elegant

An ELEGANT simulation is a particle tracking code widely used for accelerator physics simulations. The code can evolve a six-dimensional distribution (x, xp, y, yp, t, p) through a beamline defined by many useful elements such as a bending magnet, a RF cavity, a quadrupole, a sextupole, and an octupole.

The input and the output distribution are in a format called sdds. The sdds (self describing data sets) files are managed by SDDS Toolkit, which is distributed along with the ELEGANT simulation. The command PLAINDATA2SDDS can convert large ascii files written

[1]The GIT simulation is unrelated to the Git software that is used to track the changes in codes, but the Git link for the GIT simulation is `https://github.com/pietromux/GIT_2019.git`.

in a csv format into compact binary files. Each column is defined with its own name (such as p for a momentum in ELEGANT simulation), along with its unit and descriptions, and parameters like a charge can be stored. The software has many useful functions such as SDDSQUERY to view all the columns and parameters defined in a file, SDDS2STREAM to output the columns into the command line, and SDDSPROCESS to select a specific element in a beamline by matching the element name. Commands such as SDDSPLOT and SDDSPFIT can be used to generate a plot directly from the command line without using an external environment like Python. A combination of the commands SDDS2STREAM and SDDSPROCESS can be used in an ELEGANT input script to read an input parameter processed from a SDDS file. The smoothening commands DOUBLEDIST6 and SMOOTHDIST6S were also used for the project to increase the particle distribution number and smoothen the distribution.

An input distribution in the ELEGANT simulation can be set by BUNCHED_BEAM which has several options such as the distribution profile, Twiss parameters, energy spread, bunch length, and momentum chirp. Alternatively, the input distribution can be read from an external file by SDDS_BEAM.

The simulation has an easy option to generate the analysis of the Twiss parameters (beta function, alpha function, dispersion, chromaticity, etc.) and the distribution parameters (transverse beam size, emittance, energy spread) throughout the longitudinal distance. The simulation can also generate the matrix elements up to the third order evolved throughout the longitudinal distance. The options TWISS_OUTPUT and MATRIX_OUTPUT are very useful since they can create a quick analysis of a beamline without running the entire distribution.

The RF wave in ELEGANT is in the form of $V_0 \sin(k_{rf} z + \phi)$, in which the phase between $[0, 180]$ degrees has higher energy in the tail than in the head. In ELEGANT convention, $z_{head} < z_{tail}$ and $t_{head} < t_{tail}$, so the tail has travelled further than the head. The element RFCW was used for the RF linac structures with the transverse and the longitudinal wake.

There are elements that define the bending magnets. The simplest form is a rectangular dipole and a sector dipole set by RBEN and SBEN. The space charge effects (LSC) and the

coherent synchrotron radiation (CSR) effects are important nonlinear effects that usually increase the beam emittance and the energy spread. The effects are computed in CSRCSBEND element.

The drift can also be defined by a simple DRIF or DRIFT element. The nonlinear effects can be computed by setting a LSCDRIFT or a CSRDRIFT in place of DRIFT. The drift elements after the bending magnets are influenced by the CSR effects, so they should use CSRDRIFT in order to see the overall CSR effects caused by a set of bending magnets.

The optimizer function in the ELEGANT simulation can be used to match the matrix elements or the Twiss parameters. The optimizer can read from the Twiss output file or the matrix output file to generate the cost function. The optimizer can read the final position, or an element called MARKER can be used to set a position within the beamline to read a parameter to optimize. The optimizer in ELEGANT was used to match the transverse beam from the APS beamline to the TESSA beamline. The optimizer was also used for a bunch compressor and a sextupole simulation, in which a user can change the bending magnet strength along with the quadrupoles to optimize the matrix elements and the dispersion. Meanwhile, using the ELEGANT optimizer for a six-dimensional distribution is more difficult, because the energy spread or the emittance will not be read by the optimizer in a conventional format, so the TESSA collaborators from Radiasoft developed an external python script called RSOPT[2] to optimize based on the distribution.

Recent updates in ELEGANT simulation allows backtracking of a beamline. A user can take an ideal distribution and feed it backwards to get an estimated input distribution. Although not discussed in this document, the backtracking option was one of the methods that was used to evaluate the problem regarding the optimization of the distribution.

[2]RSOPT: `https://github.com/radiasoft/rsopt`

1.7.4 Astra, Opal, and GPT

On the front-end side of a beamline where the electrons are injected, the beam dynamics are strongly influenced by the three dimensional space charge effects at the low energy. ASTRA, GPT[112], and OPAL[26] are some of the usual codes that are used to simulate a photoinjector. The simulations set a three dimensional mesh to compute the space charge effects, and a greater number of meshes in each dimension is necessary with a greater number of particles, significantly increasing the computation time.

The start-to-end simulation presented in this document used ASTRA simulation to the end of the first linac structure. Afterwards, the simulation at a higher energy was done in ELEGANT. The ASTRA simulation was chosen over the others because the previous APS researchers had already used ASTRA. The researchers at Advanced Photon Sources (APS) have done ASTRA simulations throughout the beamline and have matched the transverse beam size throughout the beamline.

An ASTRA simulation has its own GENERATOR script that creates an initial distribution, in which one can define different shapes such as an uniform, radial, radial uniform, or Gaussian distribution for each of the x, y, z, px, py, pz coordinates. The RF cavity in ASTRA is defined by $V_0 \cos(\omega t + \phi)$. The AUTOPHASE function can be used to input a phase calculated from the maximum energy, in which a negative phase makes the tail at a higher energy than the head. Otherwise, the phase for the cavity will be calculated from the zero of a cosine function. The head and the tail in an ASTRA simulation are in the opposite convention of an ELEGANT simulation.

The way the lattice is defined in all of ASTRA, OPAL, and GPT is that a user defines a longitudinal position of an element. This allows stacking different elements such as a quadrupole and a linac at the same position. The linac structures at APS have quadrupoles, so in ELEGANT the elements are looped with small elements to account for the stacked elements.

Other TESSA collaborators from Radiasoft used OPAL instead because OPAL is a freely distributed code. They benchmarked the OPAL input script based on the ASTRA results provided by APS. Their start-to-end optimizer RSOPT can optimize ELEGANT, OPAL, and other Python codes in one input file. Recent progress in OPAL also allows a backtracking option, so a user can track an ideal output distribution to estimate an ideal input distribution.

The GPT simulation was seldomly used for the TESSA simulations presented in this document because the conversion of the APS linac written for ASTRA was not straightforward. However, the custom elements function in which a user can define an element greatly increases its potential usage. A. Fisher, P. Musumeci, and S. B. Van der Geer have worked on an FEL element that uses GPT to compute the FEL radiation without using external codes like GENESIS[40], so the TESSA simulation technically can be done in one script in the future.

1.7.5 Radia

The RADIA simulation is a three-dimensional magnetostatics computer code that is optimized for undulators [19]. RADIA uses boundary integral methods to calculate magnetic fields around source objects such as magnetized volumes or current coils. Magnets can be designed as three-dimensional objects from which the simulation can calculate the three-dimensional magnetic fields. The best results are obtained by subdividing the objects into smaller grids, in which computation time increases greatly. The simulation result gives magnetic fields and field integrals.

CHAPTER 2

LEA-TESSA Experiment

This chapter discusses the TESSA experiment planned to be conducted at the Argonne National Laboratory. First, this chapter introduces the overall layout and the transverse beam parameters of the TESSA beamline. Then, the design choices made for the magnetic design and the quadrupole lattice are the first subjects of the chapter. The design for the injection chicane and the prebuncher chicane utilizing currently available dipoles are then discussed. Afterwards, the intra-undulator break section that incorporate the quadrupole lattice system for reducing the beams and the phase shifter is described. The next part of the chapter discusses the simulation methods of tapering optimization, time-dependent FEL studies, and tolerance studies. Details on the post-undulator diagnostics designed for the TESSA experiment are also provided.

While FELs in the X-ray regime are important in a variety of scientific research such as molecular imaging and lithography that utilize from high power short wavelength laser sources, the efficiency of radiation production from electron beams is low. FEL extraction efficiency is generally around the Pierce parameter which usually amounts to 0.1%. In recent experiments UCLA has conducted high efficiency extraction experiments from prebunched electron beams and high power seed. In the Nocibur experiment electron beam energy of 50 MeV and a seed laser of 100 GW and 10.3 μm was used to produce radiation amplification at efficiency in range of 30 % with prebunched electron beams and 0.54 m helical permanent magnet undulator[107, 108]. This proof-of-concept experiment motivated the researchers to move forward with the high extraction efficiency experiments at shorter wavelengths.

Because the large initial seed in the Nocibur experiment complicated direct measurement of the amplified radiation, as a next experiment we would use a moderate amount of seed, around 1 GW and study the high-gain regime in which the amplified signal is far larger than the seed.

Meanwhile, most of mechanical design of the helical Halbach arrays for the permanent magnet undulator followed those of the Rubicon undulator built for the previous experiment on Rubicon IFEL and Nocibur IIFEL [30]. With tapered helical undulators, a prebunched beam, and a moderate amount of seed, the Tapering Enhanced Stimulated Superradiant Amplification (TESSA) experiment at 257.5 nm will study the extraction efficiency of radiation amplification in mid-range wavelength. The experiment was named "TESSA-266" because the initial design of the experiment was at 266 nm until the seed laser purchasing was finalized.

To achieve a wavelength in the mid-range, we would need an electron beam energy in the range of 200-400 MeV. The best available facility for the experiment was the electron beam energy of 375 MeV at the Linac Extension Area (LEA) of Argonne National Laboratory (APS). The beam will utilize an upgraded LCLS-type photoinjector that can provide high brightness, low emittance beams that are available in interleaved mode, sharing the usage with the APS ring which uses electron beams produced from two thermionic guns. The electron beam will have peak current of 1 kA with 2 mm-mrad transverse emittance and energy spread of 0.1 %. The design parameters are summarized in Table 2.1.

For the rest of the chapter we will discuss the experimental designs considering utilization of electron beam from LEA beamline for the TESSA experiment. The reader should note that a change of plans at ANL and other circumstances (including the onset of the COVID-19 pandemic) conflicted with the original timeline for the experiment, so it is likely that the actual experiment of "TESSA-266" will be held at a different location. Some details of the future plans would be mentioned in the next chapter, but electron beam parameters discussed in this chapter will only consider the scenario of LEA-to-TESSA beamline.

Parameter	Unit	Value
Beam Energy	MeV	343
Bunch Charge	pC	300
Peak Current	A	1000
Bunch Length, FWHM	ps	0.3
Normalized Emittance	mm-mrad	2
Uncorr. energy spread, FWHM	keV	300
Rel. energy variation along bunch	%	<0.5
Linac rep rate	Hz	10
Seed laser wavelength	nm	257.5
Seed laser peak power	GW	1
Seed laser pulse energy	mJ	0.5

Table 2.1: TESSA-266 Design Parameters

Figure 2.1 and Table 2.2 shows the overall design of the TESSA experiment. Electron beams from the LEA beamline enters the injection chicane, which bends the e-beam so that the seed laser would enter the system via an injection mirror. The electrons and the seed laser enter the prebuncher followed by a prebuncher chicane, which prepares the electron beams for the superradiant interaction. The coherence of the electrons is diagnosed by the microbunching diagnostics installed before the undulator. Then, there are four strongly tapered undulators named THESEUS I-IV (Tapered HElical SEgmented Undulator System). The intra-undulator break sections consist of a set of doublet quadrupoles and a dipole magnet, which are to increase focusing of the electrons and to correct the phase of the electrons. Finally, Then the post-undulator diagnostics consist of five quadrupoles, a deflecting cavity, and a spectrometer magnet. This chapter discusses the details of each section of the TESSA beamline.

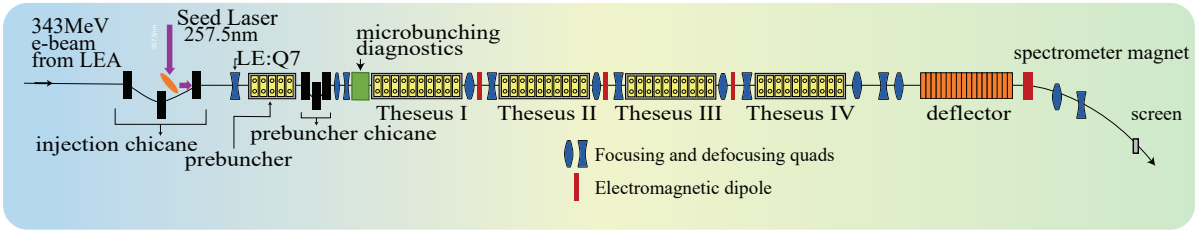

Figure 2.1: TESSA Beamline layout.

Figure 2.2 shows beta function throughout this beamline, where the first three green rectangles in the figure represent the last three quadrupoles (LE:Q5, LE:Q6, and LE:Q7) that are currently installed in the LEA tunnel. The first three black rectangles represent the injection chicane magnet. The beta function simulated in the ELEGANT lattice from the linac L2 to the end of the LEA-TESSA beamline is shown in Figure 2.3. These three quadrupoles, along with the new quadrupoles in the beamline (LE:Q8, TE:Q1, and TE:Q2) were optimized to the set of Twiss parameters matched for the periodic TESSA undulator beamline.

Table 2.2: A list of TESSA-266 beamline elements, including magnetic lengths, magnetic strengths and distances from the last reference quadrupole (LE:Q7) on the LEA beamline. The third column specifies the magnetic field for the dipoles and the integrated gradient for the quadrupoles. The physical length of the undulators is 25 mm longer than the one specified due to the end plates.

TESSA-266 Beamline			
Element Name	Length	B[T]	Center from LE:Q7
Injection and Prebuncher			
Injection Chicane Dipole 1	0.146	0.09	1.78
Injection Chicane Dipole 2	0.146	0.18	2.80
Injection Chicane Dipole 3	0.146	0.09	3.82
LE:Q8	0.153	0.189	4.40
Prebuncher	0.324		5.20
Prebuncher Chicane Dipole 1	0.146	0.08	5.60
Prebuncher Chicane Dipole 2	0.146	0.16	5.75
Prebuncher Chicane Dipole 3	0.146	0.08	5.90
TE:Q1	0.153	2.8	6.08
TE:Q2	0.153	-2.8	6.30
Microbunching Diagnostics	0.340		
THESEUS Undulators			
THESEUS I	0.964		7.19
TE:Q3	0.0307	5.62	7.72
TE:D1	0.0263	0.25	7.76
Diagnostics Cross:YAG2	0.0254		7.80
TE:Q4	0.0307	5.62	7.82
THESEUS II	0.964		8.35

TE:Q5	0.0307	5.62	8.88
TE:D2	0.0263	0.25	8.92
Diagnostics Cross:YAG3	0.0254		8.95
TE:Q6	0.0307	5.62	8.98
THESEUS III	0.964		9.51
TE:Q7	0.0307	5.62	10.04
TE:D3	0.0263	0.25	10.08
Diagnostics Cross:YAG4	0.0254		10.11
TE:Q8	0.0307	5.62	10.14
THESEUS IV	0.964		10.67
Post-Undulator Diagnostics			
TT:Q1	0.104	-2.85	11.4
TT:Q2	0.104	2.26	12.2
TT:Q3	0.104	-1.76	12.5
Deflecting cavity	1.2		13.3
Spectrometer magnet	0.25	0.4	14.2
TT:Q4	0.104	-1.08	14.5
TT:Q5	0.104	1.34	15.0
Diagnostics Cross:YAG5			16.7
DUMP			18.9

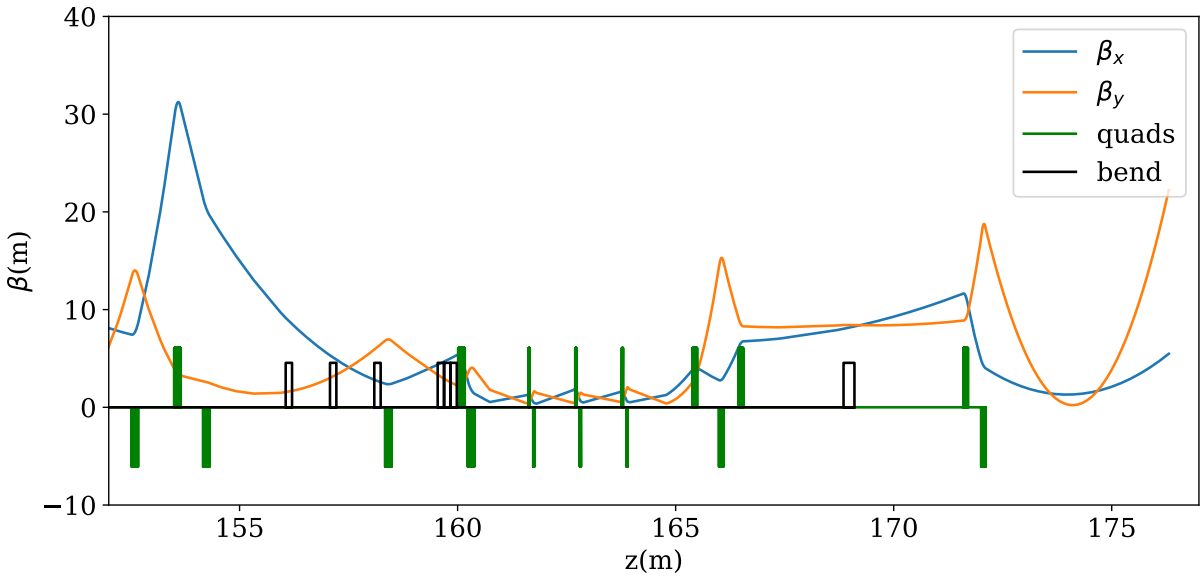

Figure 2.2: Beta functions in the TESSA266 beamline. The first three green rectangles are the three quadrupoles (LE:Q5, LE:Q6, and LE:Q7) that are currently installed in the LEA tunnel. The next three black rectangles represent the injection chicane magnets.

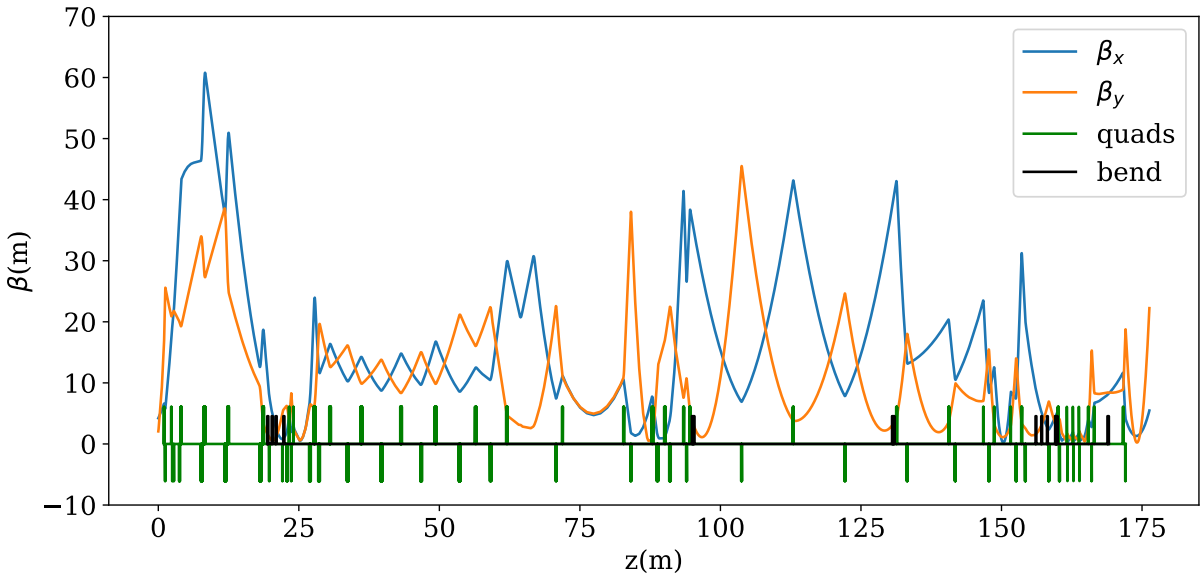

Figure 2.3: Beta functions from the linac L2 in the ELEGANT simulation to the end of the beamline. The first three black rectangles represent the bunch compressor. Then there are two dipole magnets that guide the beam to the LEA tunnel.

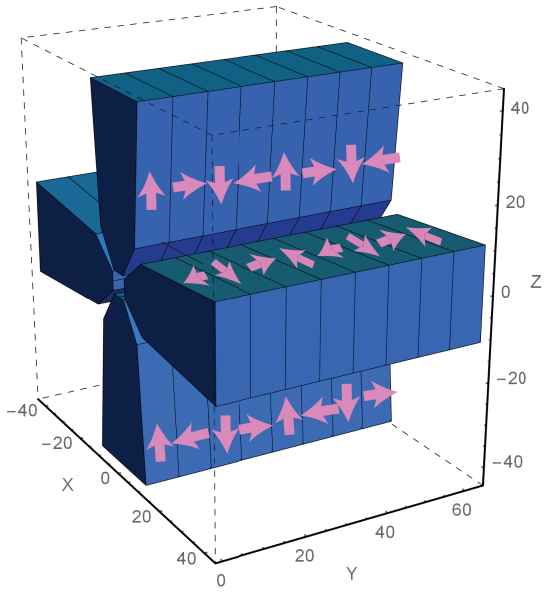

Figure 2.4: Magnetization direction in a Rubicon-type helical undulator.

2.1 Undulator magnetic design

The undulator for the TESSA experiment is composed of four permanent (NdFeB) Halbach magnet arrays in which magnetic fields alternate transversely outward, longitudinally inward, transversely inward, and then longitudinally outward. While planar undulators with two magnet arrays have been used in past permanent magnet FEL experiments, we use four arrays to form the helical beam trajectory as shown in Figure 2.4. In comparison to typical sinusoidal undulation in a planar undulator, helical undulators give an extra factor of amplification by guiding electrons in helical trajectories to continuously change direction.

In designing the undulator magnet, key parameters to consider were undulator gap, magnetic field, and period. Magnetic field and period must satisfy the undulator resonance condition :

$$\lambda_s = \frac{\lambda_u}{2\gamma^2}(1 + K^2) \tag{2.1}$$

where λ_s=laser wavelength, λ_u=undulator period, and γ=electron beam energy, and K =

$eB/k_u m_e c^2$ (undulator vector potential). Figure 2.5a shows the range of energy that can be reached at resonant wavelength of 257.5 nm given physical constraints on a permanent magnet. The strengths of permanent magnets are usually around 1 T, while actual on-axis magnetic strength is lower due to the magnetic gap. Undulator periods are usually limited to 25 mm because the thickness of each magnet would be a quarter of the undulator period, and the entrance and the exit magnets are smaller. Dashed, blue lines on Figure 2.5a indicate the nominal undulator period of 32 mm. The period was chosen based on the achievable undulator gap and the target resonant wavelength based on RADIA simulation.

A physical design of the TESSA undulator was simulated in RADIA, which is a 3D-magnetostatics code in which boundary integral methods are used to simulate the magnetic strength of magnetic devices such as undulators [20]. Magnets were designed with slanted angles on the edges in order to prevent the magnets from slipping out of their holders. The magnets were initially designed with sharp edges, but for safety reasons the edges were chamfered as the strong magnetic field of NdFeB can be dangerous while handling (Figure 2.6). Figure 2.5c compares two cases of resonant energy at 343 MeV and 375 MeV. The two lines indicate the higher nominal energy of 375 MeV during the initial phase of the experiment, and the actual energy adjusted after the undulator construction. We measured a lower undulator field because the magnets that arrived were inherently lower than expected and also because of the chamfering.

Figure 2.5c compares the resonant condition (black) with the RADIA simulation of the undulator. While a smaller undulator gap and period would result with stronger K and higher efficiency, the magnetic gap must be reasonably larger in order to fit a vacuum chamber. Consequently, we chose around 6 mm for the initial magnetic gap with a undulator period of 32 mm, and the final minimum magnetic gap was measured to be 5.58 mm after the construction. The on-axis magnetic field was measured 0.67-0.83 T. The undulator gap can be increased by the tuning screws and also by adding shims underneath the tuning plates, so there is not a significant lower limit in the undulator on-axis field. Figure 2.5a) shows

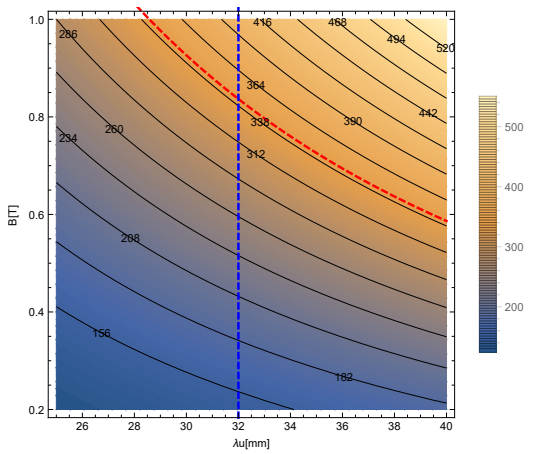

(a)

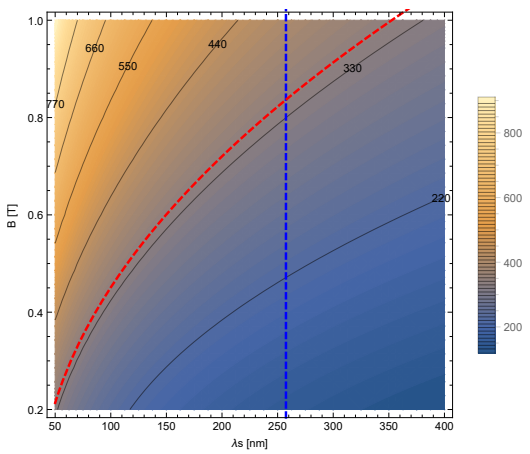

(b)

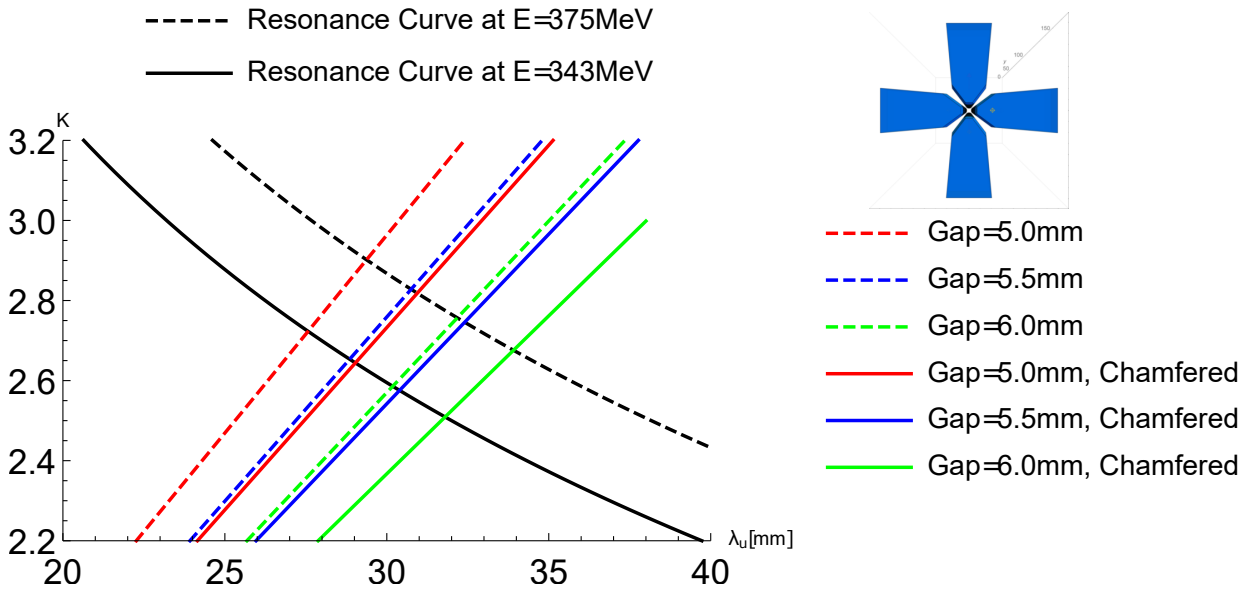

(c)

Figure 2.5: Consideration of the resonance condition for undulator design. The upper plots show the beam energy in MeV for possible range of permanent magnet undulator parameters (a) at the laser wavelength 257.5 nm and (b) at the undulator period of 32 mm. The lower plot (c) shows the undulator resonance condition (black) plotted with undulator period vs. magnetic strength of RADIA simulation, where undulator gap is shown to decrease with smaller undulator period. The blue magnetic design is the nominal design of the undulator in RADIA simulation. Solid, color lines show simulation of the final design with chamfered magnets, whereas dashed lines represent preliminary design without chamfering. In a and b, the maximum field measured is where the two dashed lines cross.

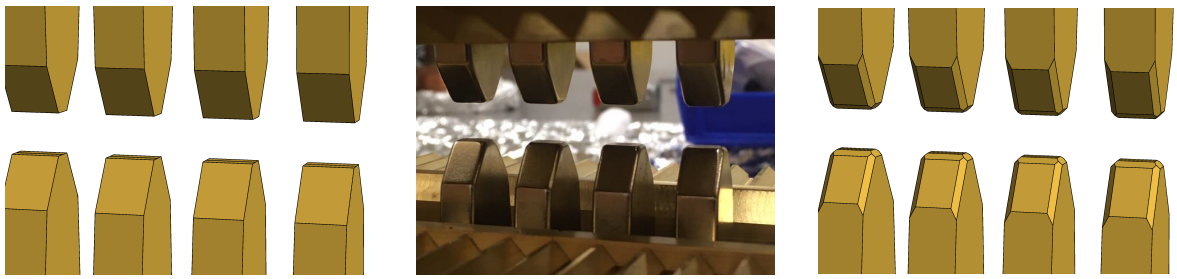

Figure 2.6: Chamfering in the TESSA undulator.As a final design the magnets had grooves on edges of the magnet, which lowered overall magnetic field. (a) RADIA simulation without chamfering, (b) a photo of the undulator magnets, (c) RADIA simulation with chamfering.

the ranges of beam energy and radiation wavelength that can work with different undulator on-axis field. The blue vertical line indicate an undulator period of 32 mm which is the final design, and the red curve indicate the nominal resonant energy of 343 MeV. With a lower undulator on-axis field and larger undulator gap, electron beam energy of 150 MeV is also a feasible option as shown in this plot.

With the tight undulator magnetic gap, the vacuum chamber for the undulator was OD/ID of 5.55/4.55 mm, which was custom-designed from MDC. While it was commonly asked whether the entire undulator should be surrounded in a vacuum chamber, vacuuming a undulator with permanent magnet arrays is not a simple task, and a pipe is commonly necessary for measuring the undulator for moving the probe in a straight path.

The entrance and the exit magnets were designed based on a system of 1/4, 3/16, 1/8, and 1/16 length of an undulator period that cancels field integrals as suggested in literature [21]. The final design of 2 mm, 4 mm, 6 mm, and 8 mm entrance magnets increase the total length about one undulator period. One can also see that for a helical undulator the period of 32 mm is close to the achievable size due to the thinnest entrance magnet of 2 mm. One would either need to order a magnet as thin as a paper or consider a non-traditional ways to correct the trajectory.

The tuning plates have holes for 7/64" hex keys that are adjustable by 800 μm per full revolution of tuning bolts, and strongbacks are made of 360 brass. Engineering details have been published by the TESSA collaborator [15]. Figure 2.7d,e shows the two TESSA undulators that have been built.

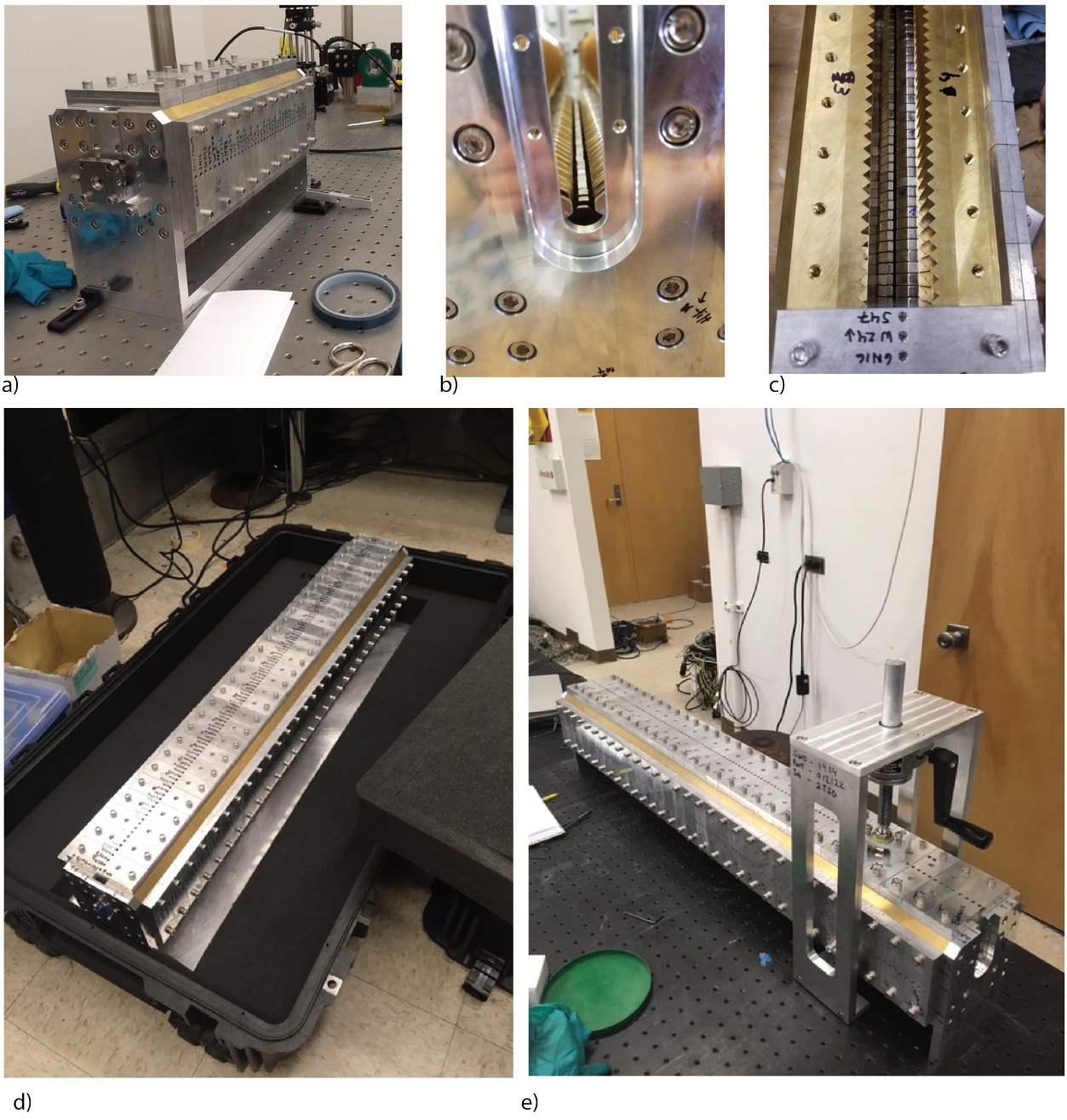

Figure 2.7: Pictures of the constructed prebuncher and undulators. (a) the prebuncher, (b) a front view of the prebuncher, (c) a top view of the prebuncher (d) the first undulator (e) the second undulator. The prebuncher shown in a-c is also a preliminary, shorter design for the TESSA undulators in d-e.

2.2 Electron beam spot size minimization

As shown previously from 1D TESSA analysis (Equation 1.64), FEL extraction efficiency depends on several parameters such as undulator on-axis field strength, undulator period, peak current, and beam energy. Reducing the spot size would improve the efficiency by a factor of inverse-square of beam size. In order to study the effects of reducing the spot size, we explored different ways to focus the beam using the transport matrices. Evolution of transverse beam matrices can be written in terms of 2x2 matrices where the matrices for drifts M_d, quadrupoles M_q, and undulators M_u are written as:

$$\begin{aligned} M_d &= \begin{pmatrix} 1 & d \\ 0 & 1 \end{pmatrix} \\ M_q &= \begin{pmatrix} \cos(k_q z) & \frac{1}{k_q}\sin(k_q z) \\ -k_q \sin(k_q z) & \cos(k_q z) \end{pmatrix} \\ M_u &= \begin{pmatrix} \cos(k_{z,u} z) & \frac{1}{k_{z,u}}\sin(k_{z,u} z) \\ -k_{z,u} \sin(k_{z,u} z) & \cos(k_{z,u} z) \end{pmatrix} \end{aligned} \tag{2.2}$$

where d=drift length, $k_q = \sqrt{G\frac{300}{E[MeV]}}$ where G is quadrupole gradient and $k_{z,u} = \frac{1}{\sqrt{2}}\frac{kK}{\gamma}$. At each position in z of a FODO lattice a corresponding matrix should apply, and the evolved beam should obey

$$\sigma_f = M_{tot}\sigma_0 M_{tot}^T. \tag{2.3}$$

Given a transformation matrix of a periodic lattice written as

$$M(z) = \begin{pmatrix} C & S \\ C' & S' \end{pmatrix}, \tag{2.4}$$

a set of Twiss parameters $(\beta_0, \alpha_0, \gamma_0)$ that is matched at both ends of the periodic lattice can be found by solving for the eigensolutions of the transformation matrix constructed as

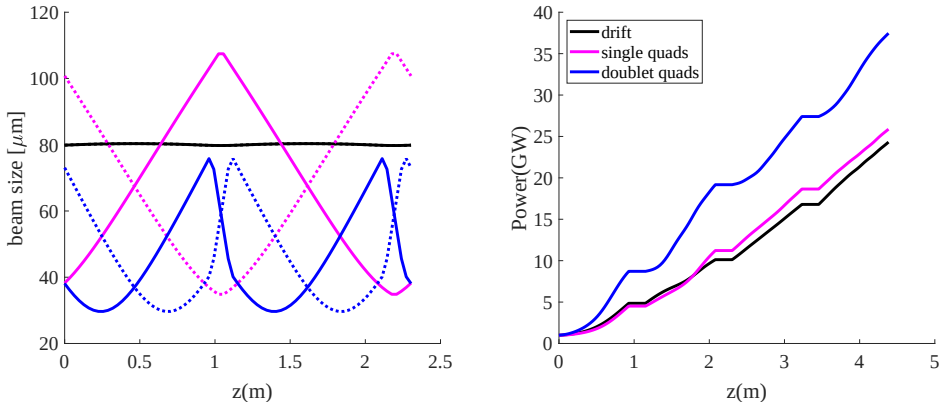

Figure 2.8: (a) transverse beam size (x=solid, y=dashed) in an undulator and break section when there is no quadrupoles (black), single quadrupole (magenta), and doublet quadrupoles (blue). (b) amplified radiation power through four undulator sections obtained from optimized tapering.

[116]:

$$\begin{pmatrix} C^2 & -2CS & S^2 \\ -CC' & CS'+C'S' & -SS' \\ C'^2 & -2C'S' & S'^2 \end{pmatrix} \begin{pmatrix} \beta_0 \\ \alpha_0 \\ \gamma_0 \end{pmatrix} = \begin{pmatrix} \beta_0 \\ \alpha_0 \\ \gamma_0 \end{pmatrix} \tag{2.5}$$

Figure 2.8a shows beam size obtained from matrix multiplication for different focusing systems. Transverse analysis showed that average spot size is 80 μm without quadrupoles (black curve), 68 μm with one quadrupole (magenta curve), and 46 μm with two quadrupoles (blue curve). Each single and double quadrupole system was assessed by finding the optimal quadrupole gradient with the smallest average transverse beam. Afterwards, each optimal lattice was simulated via the tapering optimization by GIT, and we found that the best system was indeed the doublet quadrupole system with the smallest average spot size (Figure 2.8b).

2.3 Laser Parameters

The seed laser for TESSA-266 is a diode-pumped ultrafast laser of 5 mJ energy with up to 100 MHz at 1030 nm wavelength with pulse duration 500 fs to 10 ps. The laser will be synchronized with less than 250 fs jitter. The system will be on an optical table of 1200x800 mm where a synchronized oscillator, a long cavity amplifier, and a compressor will be installed. The laser will be converted to 257.5 nm by two β barium borate (BBO) crystals.

A β-BBO crystal that will be used for the wavelength conversion is a low-temperature phase of a barium metaborate crystal. As opposed to an α-BBO which is a high-temperature phase with symmetric properties, a β-BBO has a $\chi^{(2)}$ type of optical nonlinearity that is used for the frequency doubling. Due to its transmission range (190-3500 nm), phase matchable range (410 to 3500 nm), and high damage threshold, a β-BBO is widely used to double the frequency.

The laser system will be located in a laser room being prepared two walls behind the main LEA tunnel (Figure 2.32c). Because permission to access the tunnel would need to follow the national laboratory schedules, we decided to have UV conversion in the laser room instead of in the tunnel. A downside to this decision is the potential for nonlinear effects due to the long transport of the laser in UV. The optical setup for transporting from the laser room through the tunnel and to the injection mirror was designed to reduce the nonlinearity effects.

Initially the laser beam size will be 1.9 mm in $1/e^2$-radius, but because laser beam energy of 5 mJ is rather strong and may damage the crystal, we would expand the beam size to $1/e^2$-radius of 5 mm.

To consider how large a crystal or other optical component should be, one can approximate the beam diameter to be around π times the $1/e^2$-radius.

Due to the larger spot size, the crystal will be 15 mm x 15 mm in transverse dimension. It

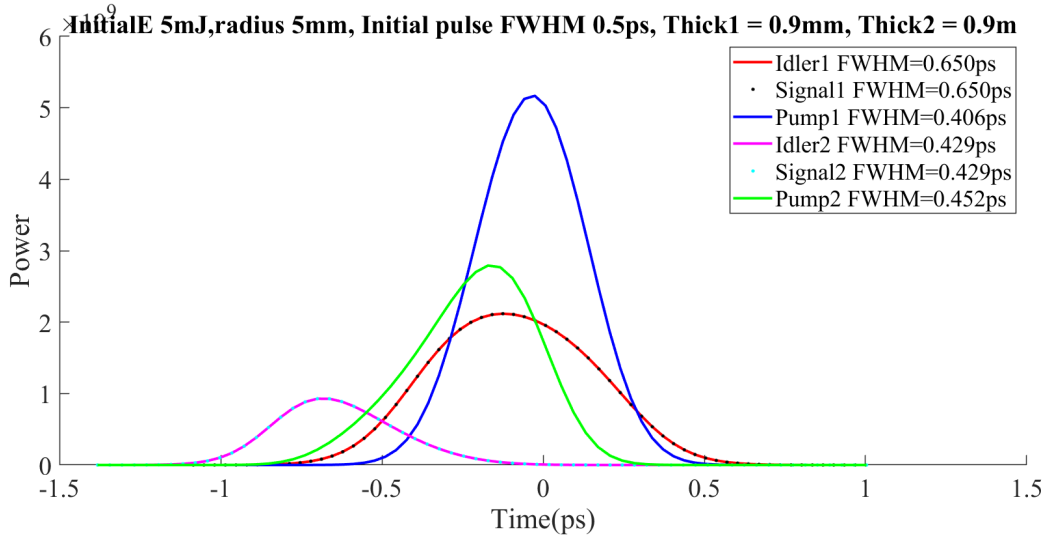

Figure 2.9: SNLO Output for two crystals of 0.9mm thickness. Initial energy was 5 mJ, with $1/e^2$-radius of 5 mm and initial pulse of 0.5 ps (FWHM).

was undetermined at the point of the design whether the laser system will have a capability to change the laser spot size, so this section will discuss both cases where in one case the laser spot size starts at 5 mm, and the other at 1.9 mm.

With initial energy of 5 mJ and laser spot size of 5 mm, two 0.9 mm thick crystals would provide peak power of 2.8 GW and a pulse length of 0.45 ps (Figure 2.9).

The pulse length is not conserved in this system, but the long transport in air may increase the pulse length. A system of 3mm and 0.9mm crystals consecutively for 1030 nm and 575 nm would provide a conserved pulse length, but a thicker crystal was not preferred due to the possibility of nonlinear effects.

The first 0.9 mm crystal that will convert from 1030 nm to 515 nm will have an multi-layer anti-reflective (AR) coating, and the second crystal will have a single layer protective (PR) coating. The manufacturer (Newlight Photonics Inc.) recommended a PR coating for the second crystal because UV may damage the AR coating. The crystal can be mounted on an 1" optical mirror mount and post.

2.4 Laser Transport

After the wavelength conversion the laser will be transported through approximately 50-meters and will enter the beamline of the experiment in the injection chicane area. The total path length was assumed to be 50-meters to the best of the knowledge of the engineers at the moment, but actual distance may vary based on the engineering details. Meanwhile, the optical design discussed here will not vary significantly with a small change in distance.

There will be eight mirrors transporting the beam from the laser room to the injection position. All the mirrors except the injection mirror are 2" diameter, 1/4" thick, and double-coated by HfO2 and SiO2 for 257.5 nm (seed laser) and 532 nm (alignment laser) from CVI Laser Optics. The peripheral equipment such as cubes and mounts will be purchased from Thorlabs. The mount system will consist of a rotatable and kinematic platform. The long pipe in the tunnel was yet to be designed.

An important aspect of this transport design was how to predict the nonlinear effects arising from the transport and how to reduce them. B-integral is a measure of nonlinear phase shift defined as:

$$B = \frac{2\pi}{\lambda} \int n_2 I(z) dz \tag{2.6}$$

By taking the integral of the intensity $I(z)$ with a factor of the nonlinear refractive index n_2 nonlinear effects throughout the path can be estimated. Nonlinear refractive index depends both on wavelength and intensity. While its quantity with a laser with 257.5nm and 1 GW should be around $2 - 4 * 10^{-16} cm^2/W$ based on different sources [3, 74], it is difficult to predict for the specific laser that we have. When the B-integral is larger than 1, nonlinearity can significantly influence the beam quality due to self-focusing. Because of its dependence on intensity there would be less nonlinearity if the beam were transported in a larger spot size.

The beam size will be expanded to 12 mm for the transport after the wavelength conversion in order to decrease the nonlinear effects due to travelling through a non-vacuum

Focal Length	Diameter (in)	Thickness (mm)
-0.2	2”	6.35
0.5	2”	6.35
3	2”	6.35
-0.3	1”	2

Table 2.3: Table of lenses used in the transport. The lenses are double coated to be used for both 257.5 nm (seed laser) and 532 nm (alignment laser). The refractive index at 266 nm is 1.5.

medium and the laser fluence imposed at the transport mirrors. A beam size of 12 mm is the maximum spot size that will fit in 2” optics. If any larger lenses were used the thickness would need to be increased which would increase the nonlinear effects.

Then the expanded beam is transported through the tunnel and is matched to 344 μm waist using one or two lenses placed closer to the injection. When a single lens is used the focal length has to be has to be around 10-50 meters to match the waist size and position. Alternatively, two lenses can be used. In this case the focal lengths are smaller and easily available in the market. There are more versatility due to having two lens positions to adjust, as the total path length can be adjusted without changing the focal strength. Figure 2.10 shows beam size and fluence in this optical transport calculated from the ABCD ray transfer matrix analysis.

The B-Integral in the system can be up to 3 in air-transport and up to 2 in vacuum. This effect should be better studied in the lab rather than from analytic assessment because the nonlinear refractive index for specific laser parameter is not known and the nonlinear effects can vary with different circumstances such as laser or lens quality or the atmosphere.

Finally, there is also a possibility that we would need to add two additional lenses in order to increase the beam size from the initial size to the recommended beam size at the BBO

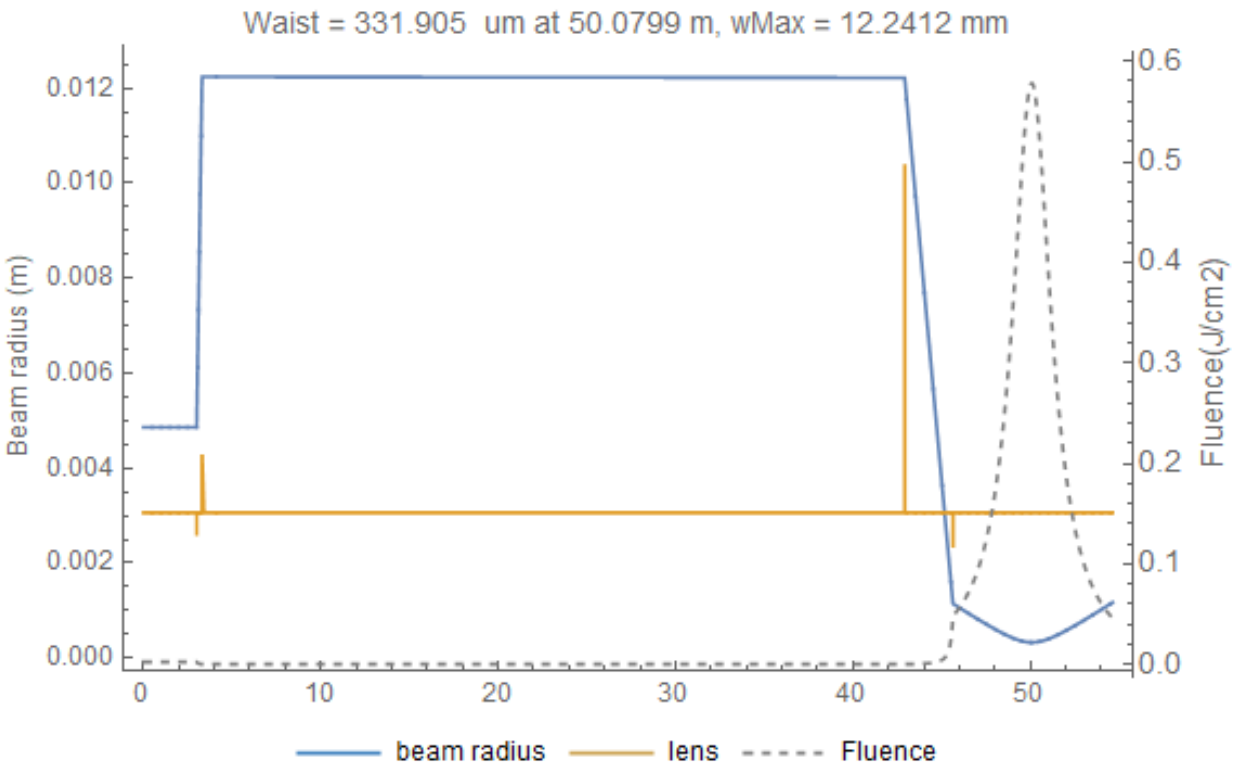

Figure 2.10: Laser Transport Setup using four lenses. The beam size is in $1/e^2$-radius and focal lengths of -0.2m, 0.5m, 3m, -0.3m are used to match from the initial beam size 5mm to the final beam size of 344um

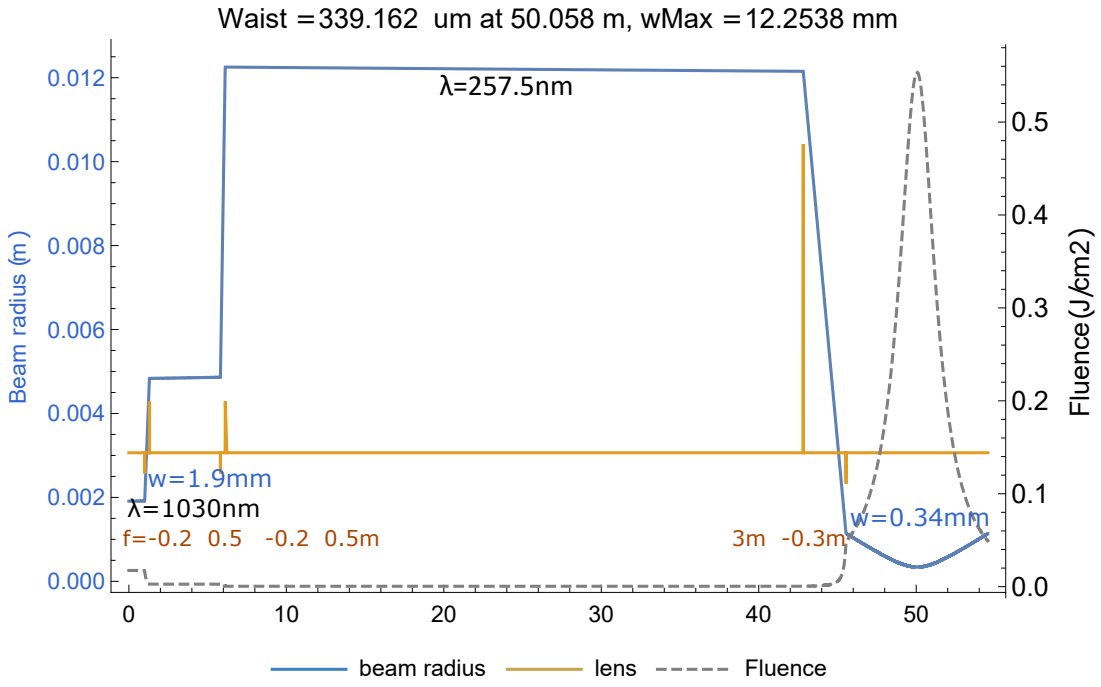

Figure 2.11: Two pairs of lenses with focal lengths of -0.2 and 0.5 meters were used to increase the beam size to 5 mm in the crystal and 12 mm in the transport. Then two lenses of 3m and -0.3 m focal lengths were used to match the beam size from 12 mm to 344 um. Laser wavelength is initially at 1030 nm, then in the second step wavelength changes from 1030 nm to 515 nm to 257.5 nm.

crystal. The laser system may include this function but there was not enough information at the point of design. In the case that we need to achieve this externally we can use the spare lenses that will be ordered along with the other four lenses. Figure 2.11 shows an optical setup for six-lenses. The first set of lenses with focal lengths of 500 mm and -200 mm was used to increase the beam size from 1.9 mm to 5 mm. Then, another set of lenses with 500 mm and -200 mm focal lengths were used to increase the beam size from 5 mm to 12 mm. Throughout the long transport in the tunnel the beam size remains constant, then a final set of lenses with 3 m and -0.3 m focal lengths were used to match the beam size from 12 mm to 344 um.

2.5 Injection Chicane

In order to bring the seed laser into the APS-LEA electron beamline, we plan to install an injection chicane to bump the electron trajectory and make a space for an injection mirror. This section will discuss the physical design and general requirements of the injection chicanes.

The dipole magnets that will be used for this system are the same as those used in the prebuncher chicane (Figure 2.15). Two of the three are edged by 12° on one side because they were used previously for focusing the e-beam in a lower-energy experiment. As the effects of the edge angle are minimal at the higher energy and as the injection chicane is further away from the main experiment system than the prebuncher chicane, we use the magnets with the edge angles for the injection chicane.

The e-beam is offset by around 12 mm by the magnetic chicane, and a cube system with a 45-degrees injection mirror is placed in the beamline axis. This mirror will reflect the laser beam that has been transported through the tunnel into the electron beamline.

Figure 2.12 shows the three magnets with corresponding nipples, bellows, and cubes. The cube was placed with a minimal displacement from the center magnet as the e-beam trajectory is maximum at the center. In this system there are three bellows placed so that the pipes can be slightly tilted horizontally to follow the e-beam trajectory. Figure 2.12 also shows how the e-beam trajectory is compared with the pipe offset.

At the cube position the laser spot size is less than 1 mm (RMS) and the e-beam spot size is less than 0.8 mm (RMS). We expect that the e-beam can be 3 times the spot size away from the surface of the pipe because closer distance can cause the wake field or other nonlinear effects. Consequently we expect that the e-beam can be offset at a maximum of 4.1 mm from the center of the pipe.

When the electron beam is offset by 12 mm from the electron beam axis at the position of the second dipole magnet, the beam will offset from the center of the pipe by 4 mm. Then,

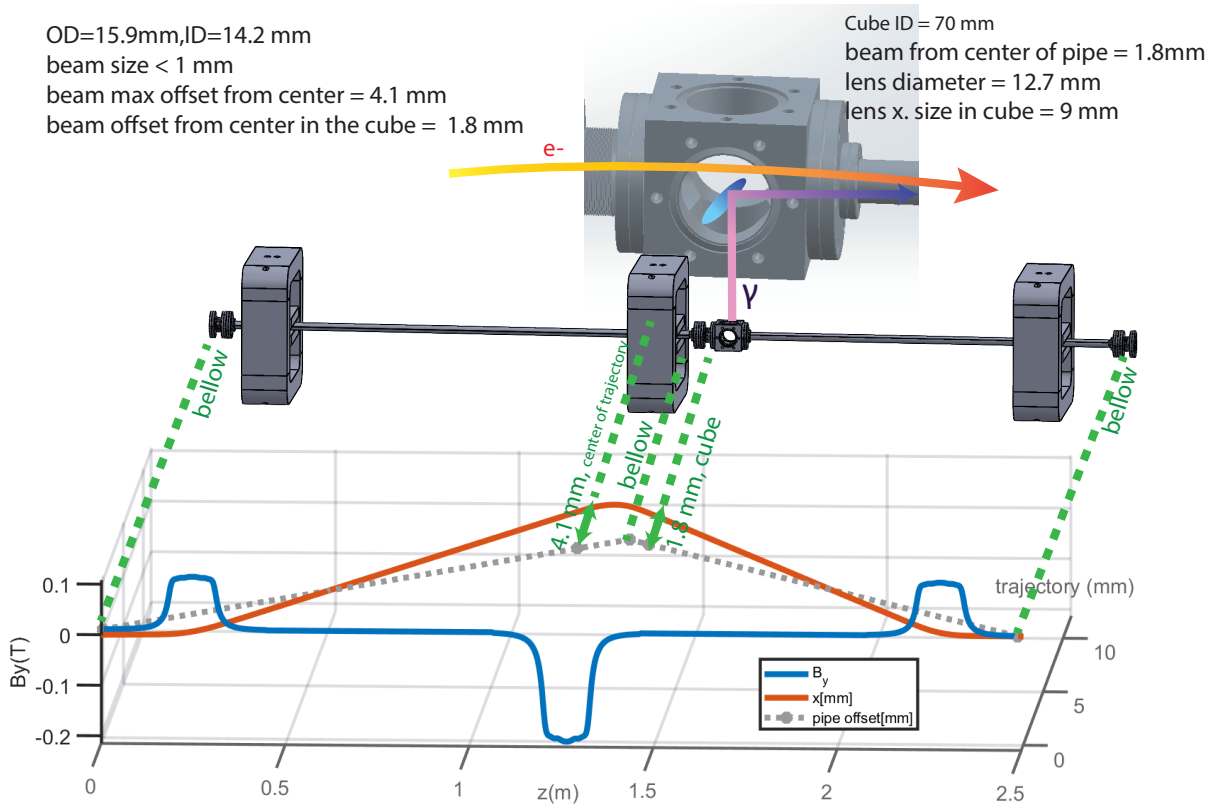

Figure 2.12: The magnetic field and the e-beam trajectory offset due to the injection chicane.

with the same dipole field, the electron beam will be offset from the beam axis by 10 mm when it passes through the cube, and the beam will be offset from the center of the cube by 1.8 mm. This shows that it would be possible to place a 1/2" lens in the beamline.

The cube will be placed at 188.63 mm from the second chicane magnet. This position was decided based on engineering considerations to place the mirror the closest to the second magnet. With the 12.7 mm diameter lens rotated by 45.4° mounted inside the cube as shown in Figure 2.12, the projected diameter will be 9 mm in the transverse space.

2.6 Prebuncher System

This section will discuss how the electron beam will be bunched for the TESSA scheme. One of the key components of TESSA-266 is the prebunching system in the upstream of the undulator system. More electrons will be in resonance with radiation with more of them in phase, i.e. with larger bunching factor:

$$b(k_s) = \frac{1}{N}\sum_n e^{ik_s\psi}. \tag{2.7}$$

The prebuncher system consists of a modulator that is a shorter version of TESSA undulators and a three-magnet magnetic chicane. The prebuncher did not have to be helical or gap-adjustable, but we meant for the module to serve as a preliminary design for the TESSA undulators which are helical and gap-adjustable. With eight periods and four arrays of NdFeB undulator magnets with entrance and exit magnets of 2, 4, 6 mm, and 800 μm per revolution tuning plates, slanted magnet holders, and 5.58 mm minimum magnetic gap, assembly and measurement of the prebuncher helped to finalize undulator design and improve construction protocols [15]. Some problems such as the difficulty of inserting magnets because of the sharp edges on the holders and the strong magnetic strengths were ameliorated for undulator construction.

Figure 2.7a-c shows fully assembled and tested prebuncher.

Previous studies about manipulation of electron beam and radiation interaction showed that using a modulator followed by a chicane is a good way to increase the bunching factor [53]. UCLA has studied the effects of prebunchers at low-gain [107]. Given energy deviation factor $p = (E - E_0)/\sigma_E$ and ponderomotive phase θ, electrons passed through a modulator will deviate by:

$$\begin{aligned} p' &= p + A\sin(\theta) \\ \theta' &= \theta \end{aligned} \tag{2.8}$$

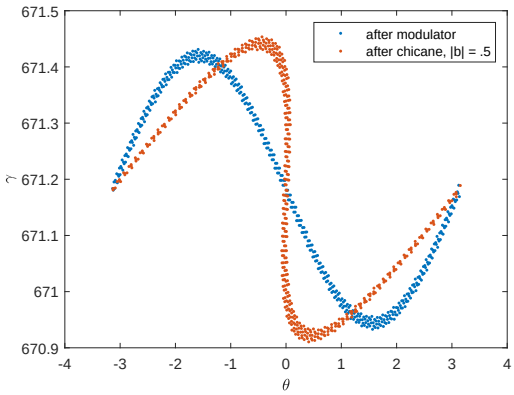

Figure 2.13: An example of a modulated (blue) and a bunched beam (red).

where $A = \Delta E/\sigma_E$. Followed by a magnetic chicane of dispersion strength R_{56}, particle positions will shift depending on their energy:

$$\begin{aligned} p'' &= p' = p + A\sin(\theta) \\ \theta'' &= \theta' + Bp'. \end{aligned} \tag{2.9}$$

From the coordinate transformation one can estimate the best R_{56} and bunching factor. Figure 2.13 shows an example of a modulated electron beam (blue) and a beam shifted by a chicane (red) through this coordinate transformation.

The modulation amplitude A represents energy deviation due to a modulator, which can be expressed in terms of the undulator vector potential parameter K and the laser vector potential parameter parameter K_l as:

$$A = \frac{\Delta\gamma}{\sigma_\gamma} \approx -\frac{kK_l}{K\gamma_r\sigma_\gamma}\sin(\theta_r)\Delta z \tag{2.10}$$

where δz is modulator length. Laser vector potential $K_l = qE/k_s m_e c^2$ depends on the field and the period of the seed.

Determining an optimal set of parameters for buncher length, chicane parameters, or laser parameters is complicated. The details of the optimization will be discussed in a later section, but in general a longer modulator could improve bunching factor with the larger

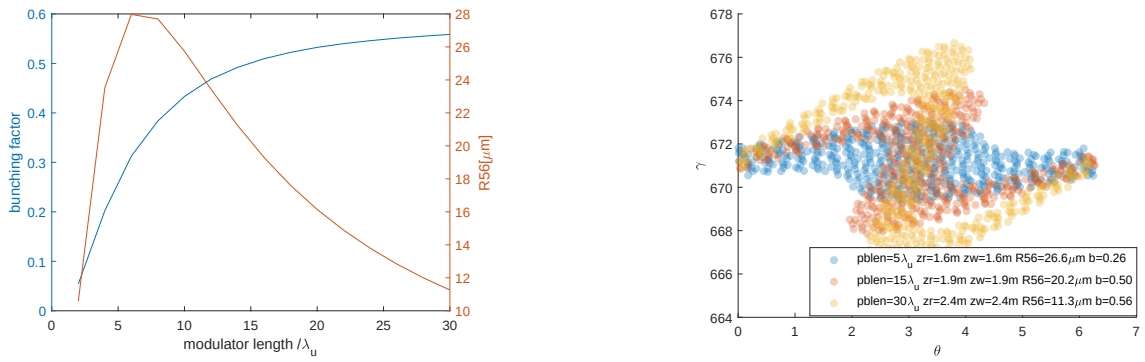

(a) (b)

Figure 2.14: Studies of modulator length, with Rayleigh range and waist position shifted by an additional length. A larger bunching factor than that of the current setup was a possibility (a) with the larger bucket height (b). The energy spread of the beam was fixed at 0.1%.

modulation amplitude, but it will put the main experiment further away from the laser injection. Longer drift to the experiment would reduce the laser field for the modulator and increase the laser waist.

Figure 2.14a compares ideal bunching factor calculated from the A,B coordinate transformation. With the changes in modulator length the waist position and Rayleigh range were increased by the same amount. The bunching factor is larger with longer prebuncher length due to the larger modulation amplitude as shown in Figure 2.14b. Meanwhile, the current configuration of $9\lambda_u$ is near saturation, so bunching would not increase as significantly with a longer system. The ideal R_{56} and corresponding modulation shown in Figure 2.14a,b at each undulator length is based on the A,B coordinate transformation.

The prebuncher chicane for TESSA system will use three rectangular electromagnetic dipole magnets of 146 mm magnetic length and 120 mm physical length with a gap of around 20 mm. The field saturation in a simulation is around 0.7 T, while we measured that

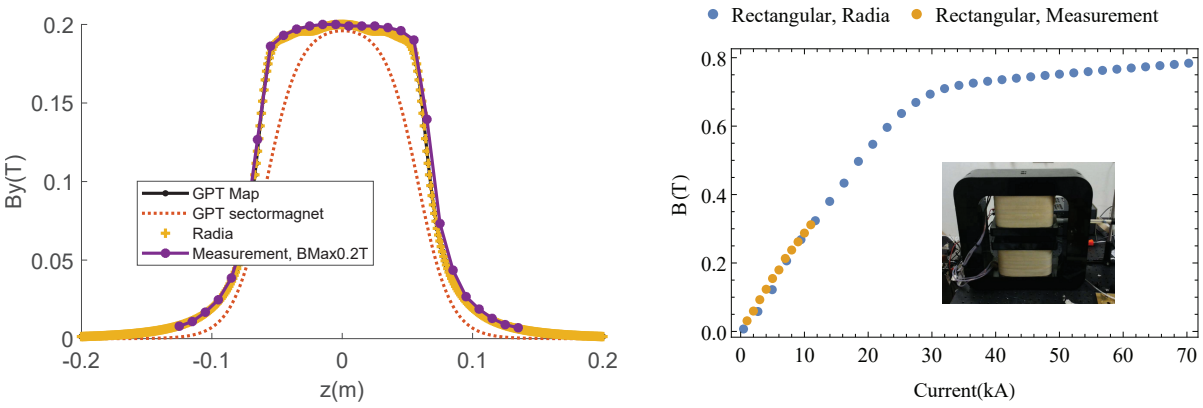

Figure 2.15: Black chicane magnet characteristics. GPT map was obtained from RADIA simulation of the dipole magnet and was measured data points in (a), and saturation curve in simulation and measured data was obtaind (b).

current to dipole strength was linear up to 0.3 T (Figure 2.15).

The drift section between the modulator and the first undulator needs to be compactly designed with quadrupoles and a magnetic chicane as well as steering magnets, YAG, BPM, and microbunching diagnostics for full assessment of the electron beam entering the TESSA undulators. As shown in the engineering drawing of the system in Figure 2.17, it is difficult to make the drift space any shorter unless there were significant re-assessment of the components. Consequently, the chicane magnets were placed so that the magnetic lengths barely touch each other. Figure 2.16 presents R_{56} computed from the ELEGANT simulation when dipole strength of the three chicane magnets were varied in ratio. The simulation showed maximum R_{56} of the system would be well above the predicted range considering 0.3 T of saturation dipole strength.

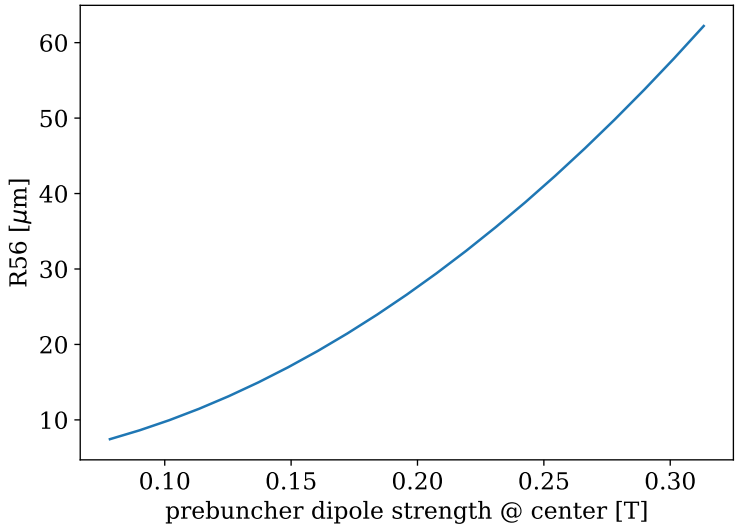

Figure 2.16: Dipole strength of prebuncher chicane and resulting R_{56}. The x-axis represents the strength of the center dipole which is twice that of the other two dipoles in the opposite direction.

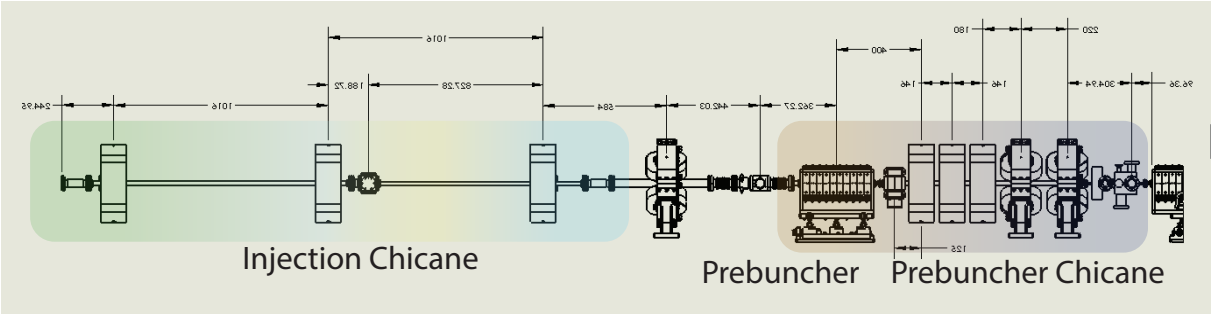

Figure 2.17: An engineering drawing from the injection chicane to the end of the prebuncher drift (before the first undulator entrance).

2.7 Undulator Break Section Design

The optimal length for the undulator and for the break section would be to have a longer undulator and a shorter break section. There would be amplification throughout the tapered undulator if the necessary conditions (resonance condition, energy spread, emittance, coherence length, etc.) were met, while the power does not increase and the spot size diffracts throughout the drift section. The undulator length then depends on the capability of the construction facility to cut and assemble the undulator components and how the undulators will be transported. Based on the capabilities of the Radiabeam's facility at the time, 29 λ_u of magnetic and 964 mm of mechanical length were determined. Meanwhile, the length of the break section needed be as short as possible while housing all the required components for the experiment.

Essential to designing a break section among a set of segmented tapered undulators would be accounting for the phase difference between electron and light through the break section.

While the electrons moving through the undulator evolve according to the ponderomotive force due to the electrons and the radiation, the electrons in the drift will lag due to the lower speed causing overall phase shift. Electrons outside the undulator travel by $D/2\gamma^2$ through a drift length D, and the corresponding phase shift is $\frac{2\pi}{\lambda_s}\frac{D}{2\gamma^2}$. Therefore, if the drift length is $2\lambda_s\gamma^2$, electrons and radiation will be back in phase at the entrance of the next undulator. If the drift length were not exactly an integer-multiple of $2\lambda_s\gamma^2$, the electron beam will enter the next undulator at a different phase. For a tapered undulator system, the energy of the beam must be different at the end of each undulator, so the ideal break section would vary based on electron beam energy. Having to change the drift length is not an ideal experimental setup, so it is necessary that a tapered undulator system has a phase shifter in the break section. Consequently, there was a need to build the shortest possible break section in order to reduce the effects of radiation diffraction while still housing a phase shifter as well as a pair of quadrupoles discussed previously in order to reduce the electron

beam size. The TESSA break section was designed with a phase shifter made of a dipole and a set of quadrupoles capable of horizontal offset. Figure 2.18 shows the final design of the intra-undulator system with a mechanical drift length of 170 mm from the end plates of undulators.

Quadrupoles for the experiment are hybrid, adjustable quadrupoles designed by UCLA. The quadrupole design consists of four steel poles with low carbon content (<0.06%), and two NdFeB (1.45 T remanence) wedge sectors. When the shims are pulled away from the magnet, the magnetic circuit is severed, and the pole tips are maximally magnetized, still below the saturation limit. The shims are mounted to the steel poles and their positions are controlled with thumbscrews. (Figure 2.19a). The hybrid quadrupole design was preferred in order to fit in the space-limited break section. With the physical length of 26.2 mm, we measured the magnetic length of 30.9 mm and the integrated gradient of 6.2 T, sufficiently below the required gradient of 5.62 T optimized for the smallest average beam size (Figure 2.20a,b). We designed the shortest possible dipole magnet that would fit in the clearance space of 28 mm longitudinal and 38 mm transverse avoiding conflicts with quadrupoles and the diagnostics assembly. We initially considered a conventional C-shaped dipole magnet and an H-shaped dipole magnet, but both designs were insufficient to reach the target dipole field due to the interference with quadrupoles and diagnostics. Consequently a dipole magnet with a protruded pole was designed in order to increase the field at the center (Figure 2.19b). We measured up to 0.35 T at current of 6 A with magnetic length of 24 mm, which is above the required dipole strength of 0.25 T for a full phase shift (Figure 2.20c).

2.7.1 Break Section Length

By optimizing the time-independent GIT simulation, one can assess how the drift length affects overall efficiency. Figure 2.21a shows how the output power decreases by the rate of around 1.3% per undulator period. The simulation was done with the phase shift corrected after each undulator differently for each section length as shown in Figure 2.21b.

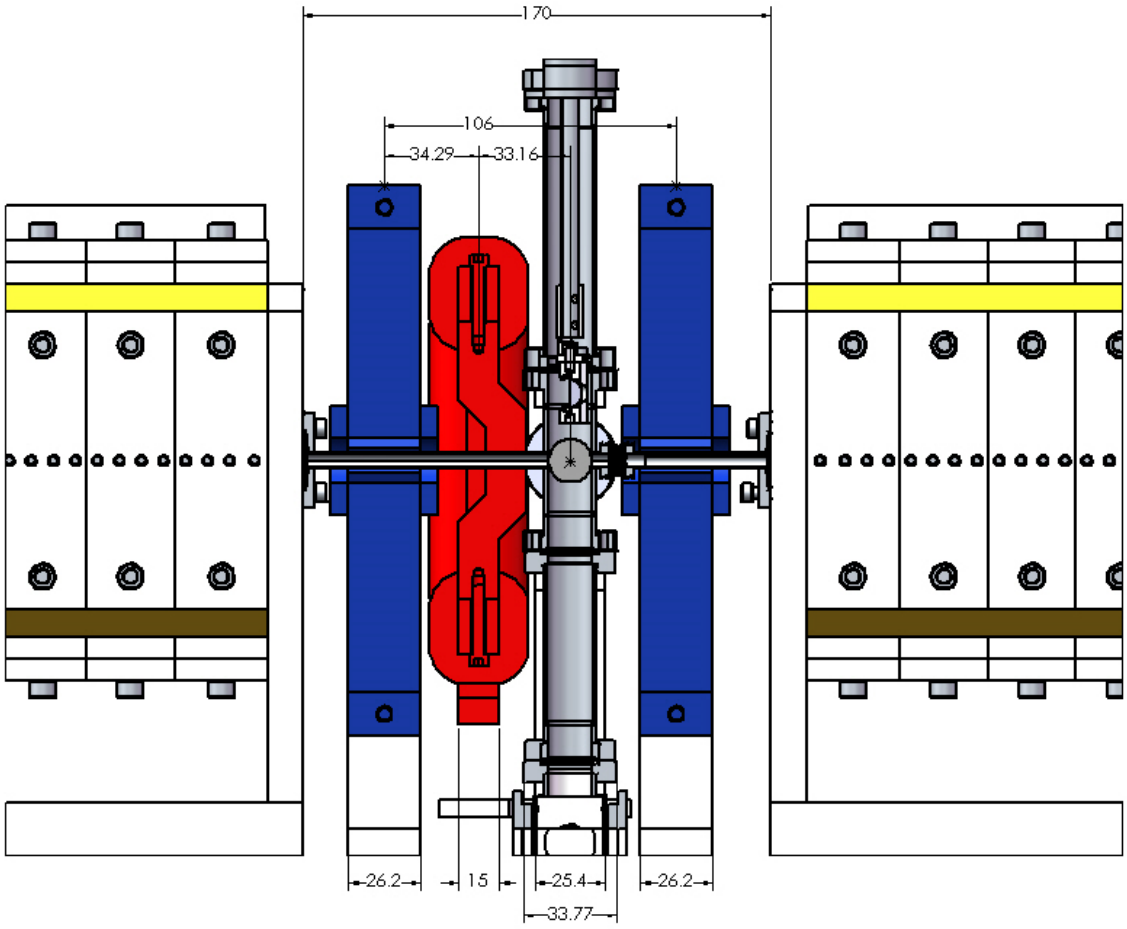

Figure 2.18: Break section design with a doublet of quadrupoles (blue) and an electromagnetic dipole (red). Grey assembly in the center is diagnostics assembly that contains YAG screen.

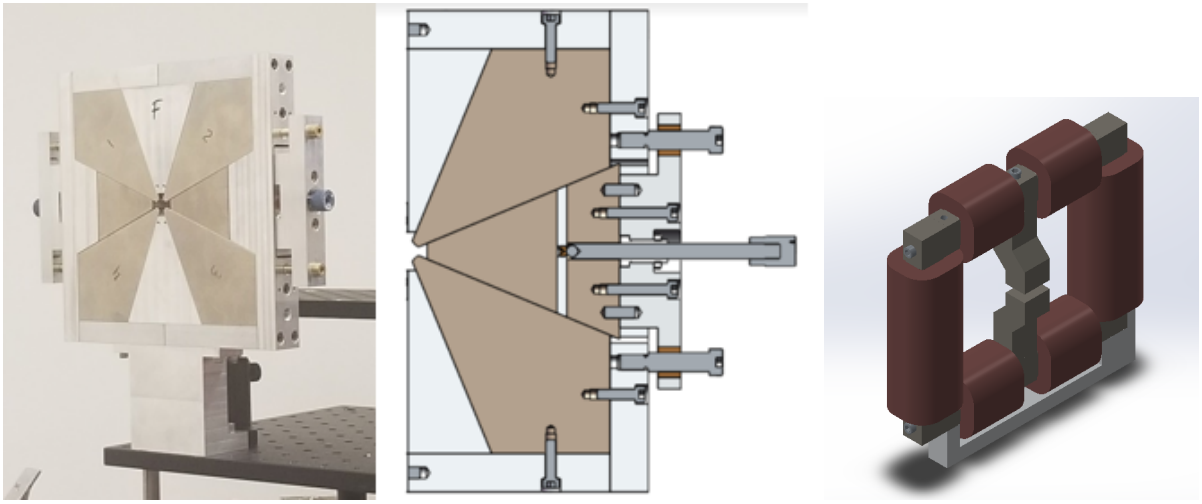

(a) (b)

Figure 2.19: (a) Hybrid, gap-adjustable quadrupole magnet for TESSA-266 (b) H-shaped electromagnetic dipole with a protruded pole

2.7.2 Phase Shifter Design

Because of the strong energy dependence per distance due to the strongly tapered system, a full phase shift capability would be beneficial. As the break section for this experiment already includes a doublet of quadrupoles, an space-efficient way to design the break section was to add an electromagnetic dipole. One can create the dipole field by shifting the quadrupoles transversely, and with the electromagnetic dipole the three components will make a three-magnet mini-chicane. The optimal quadrupole shift can be assessed for a given magnet position and strength based on the e-beam trajectory in a phase shifter.

The phase shift due to the path difference caused by dipoles is

$$\Delta\delta = \frac{2\pi}{\lambda}\Delta s \approx \frac{\pi h^2}{\lambda}\left(\frac{1}{z_1}+\frac{1}{z_2}\right) \tag{2.11}$$

for $h << z_1, z_2$ where the rest of the distances are described in Figure 2.22. Given the bend

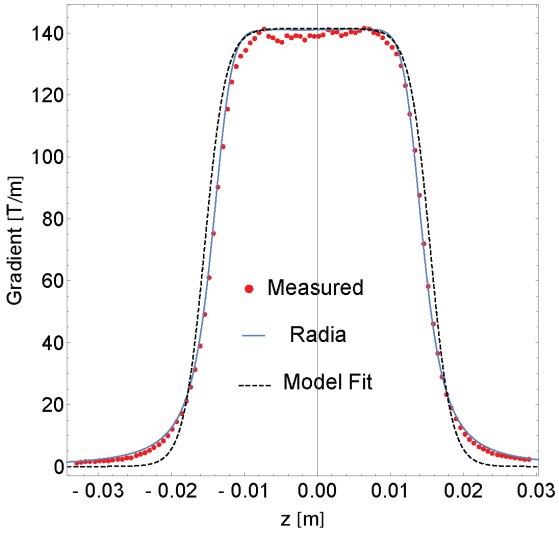

(a)

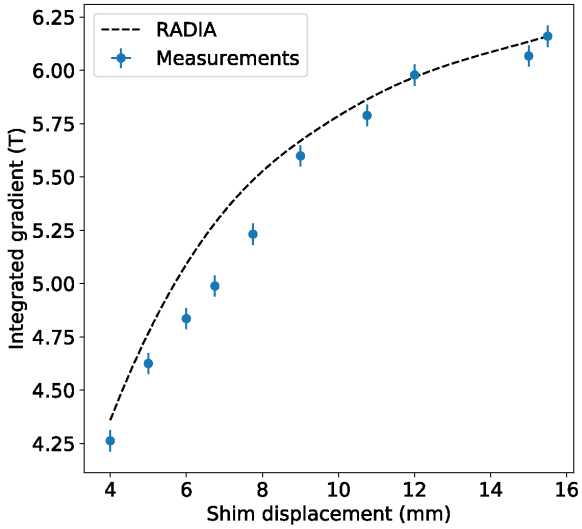

(b)

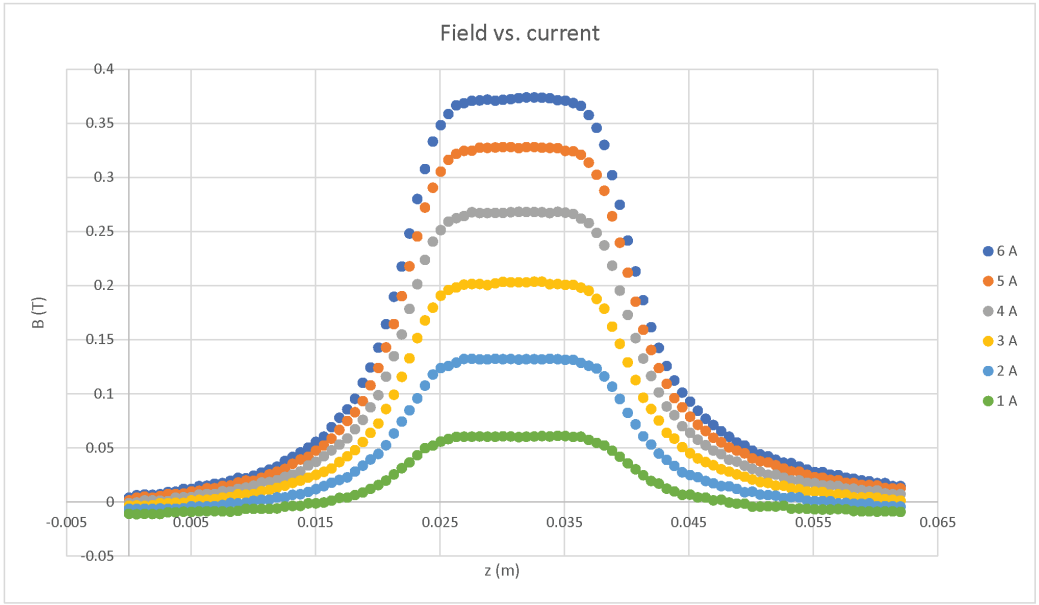

(c)

Figure 2.20: Magnetic measurements of the breaksection elements. (a) Measured longitudinal gradient profile of the hybrid adjustable quadrupole compared with RADIA and model fit with shims all the way in. (b) Comparison of measured integrated gradient of the hybrid adjustable quadrupole as a function of shim displacement and RADIA simulation. (c) Measured longitudinal profile of the electromagnetic dipole.

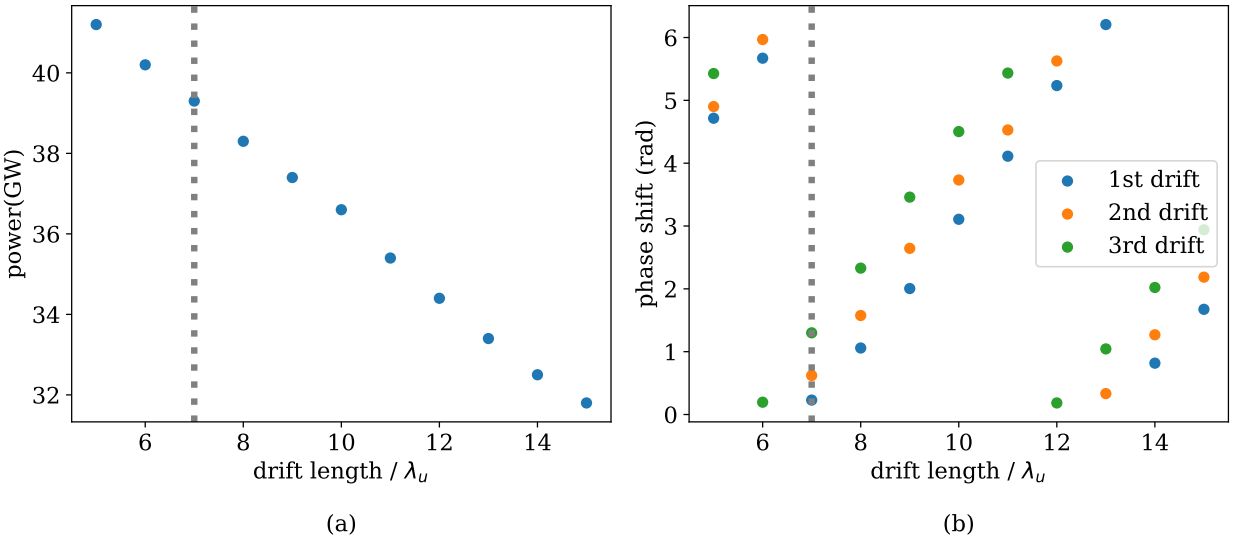

Figure 2.21: Power output from four-undulator GIT simulation at different break section lengths, in which the phase shifts were corrected differently for each drift.

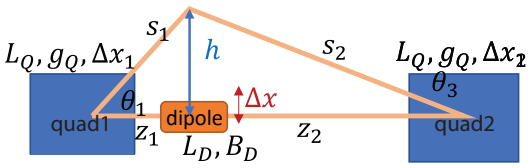

Figure 2.22: A phase shifter system with two quadrupoles and a dipole in the center.

angles for each elements:

$$\begin{aligned}\theta_1 &= L_Q g_Q \Delta x_1 \frac{E}{p} \\ \theta_2 &= L_D B_D \frac{E}{p} \\ \theta_3 &= L_Q g_Q \Delta x_2 \frac{E}{p}\end{aligned} \tag{2.12}$$

where $\theta_2 = \theta_1 + \theta_3$, L_Q, g_Q are the lengths and the gradient of the quadrupoles, and L_D, B_D are the lengths and field strength of a dipole. One can approximate the e-beam trajectory offset as:

$$h = z_1 \tan(\theta_1) \approx L_Q B_Q \frac{E}{p}. \tag{2.13}$$

Consequently, the phase shift due to dipole magnet in terms of magnet position and strength can be approximated as:

$$\Delta\delta = \frac{\pi}{\lambda}\left(\frac{E}{p}\right)^2 (L_D B_D)^2 \frac{z_1 z_2}{z_1 + z_2}. \tag{2.14}$$

Based on such considerations, the quadrupole shift required for a given magnet position and strength is:

$$\Delta x_1 = \frac{L_D B_D}{L_Q g_Q} \frac{z_2}{z_1 + z_2}. \tag{2.15}$$

From these initial approximations, the parameters were further optimized in GPT simulation to straighten the trajectory. Running the simulation at different dipole strengths and corresponding ideal quadrupole offsets showed that the dipole strength should be greater than 0.25 T where the quadrupole is offset around 0.6 mm in the first quadrupole (closer to the dipole) and around 0.4 mm in the second quadrupole. Figure 2.24 shows an example of the offset quadrupoles and dipole field and e-beam trajectory from GPT simulation at 0.25 T.

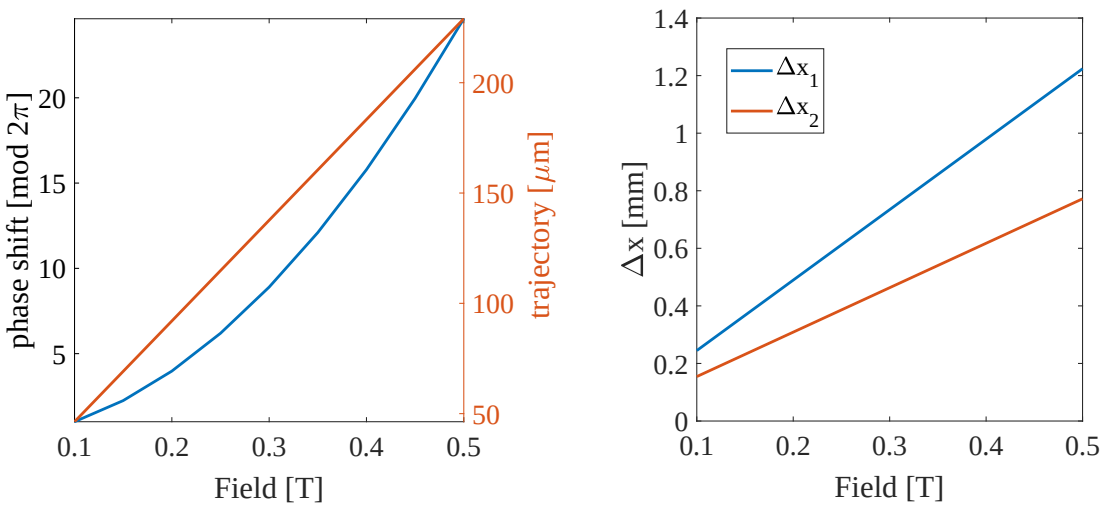

(a) (b)

Figure 2.23: Phase shifter simulation of the three-magnet mini-chicane made of two quadrupoles and a dipole, showing a full-phase shift of 2π for the dipole field (x-axis) greater than 0.25 T, with quadrupole offsets < 0.6 mm.

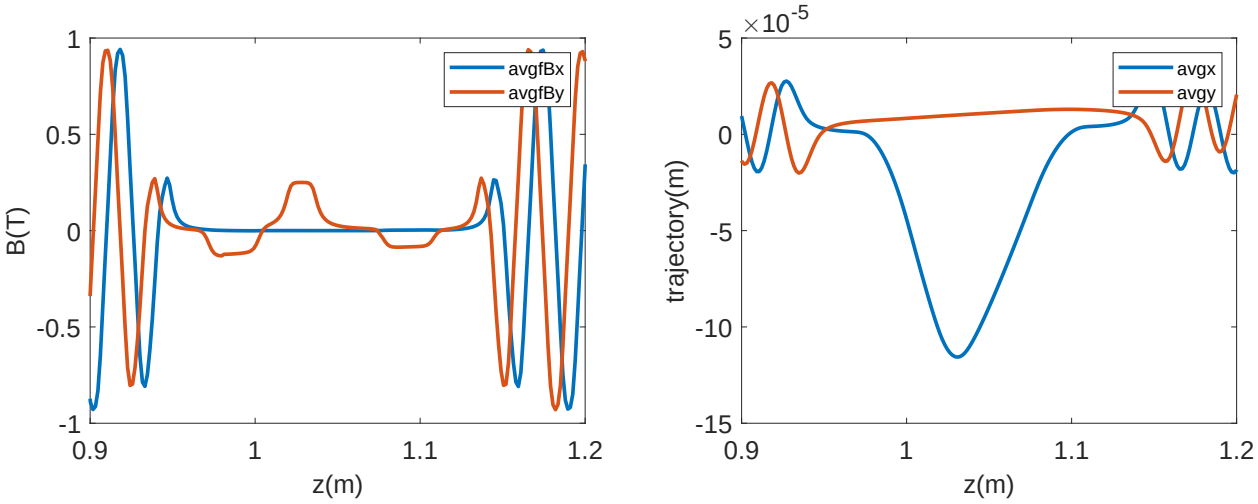

Figure 2.24: Field and e-beam trajectory offset in the break section simulated from GPT

2.8 Time-independent Simulation

For the initial studies involving magnetic designs of the undulator, quadrupoles, and phase shifters, time-independent GENESIS was used. In the time-independent mode of GENESIS, electron beam distribution is considered as a constant current and only the evolution of a single beam slice is followed during the evolution as the assumption is that the slice is representative of the entire beam. This allows a much shorter computation time and the simulation shows the three-dimensional effects of amplification, refraction, and diffraction of radiation, as well as the interaction with transverse electron beam evolution.

The laser waist and the Rayleigh range need to be optimized so that the laser intensity is sufficiently high at the prebuncher and the undulator entrance. Figure 2.25 shows the on-axis field and the radiation spot size computed at different waist position and Rayleigh range. It was found that having the waist position around the undulator entrance is ideal for this scenario. This was because the laser would be too diffracted in the undulator if the waist position were at the prebuncher, and the laser spot size would be too large for prebunching if the waist position were further in the undulator system. The Rayleigh range had a higher tolerance than the waist position as shown in Figure 2.25. Because the FEL optical effects dominate the transverse profile in the undulator, larger Rayleigh range did not change the system as much. Meanwhile, too small Rayleigh range would diffract the laser profile and consequently degrade the FEL interaction.

Meanwhile, the tapering strength is a determining factor of the efficiency. The tapering strength is controlled by the resonant phase which changes the size of the separatrix. When the resonant phase is larger, the tapering is stronger and there is more deceleration, but fewer particles remain trapped in the ponderomotive bucket. Previous studies have shown that the resonant phase of 0.5-1.0 would be reasonable to keep the particles trapped while decelerating. There are many ways to vary the resonant phase, such as to vary linearly or quadratically through out the system or to change based on the trapping fraction. Figure2.26

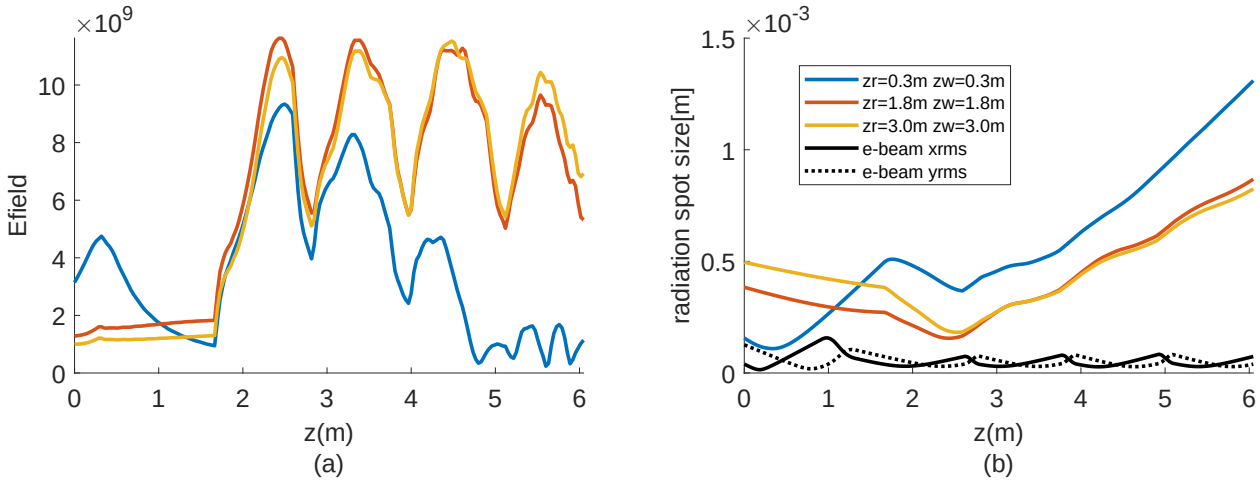

Figure 2.25: Electric field (a) and radiation spot size (b) when the Rayleigh range and the waist position were 0.3 m (blue), 1.8 m (red), and 3.0 m (yellow). The black solid and dashed lines represent the electron beam size.

compares a case of fixed resonant phase at a constant of 0.6 rad (blue) and a varied resonant phase at each undulator period (purple). In both cases, the Rayleigh range and the laser waist were set at 1.8m. In the case of the varied resonant phase, the initial and the final phase were adjusted for each undulator section, optimizing eight parameters. The resonant phase optimization increased the overall power by 2-3 GW.

As shown in the fitted functions, the tapering strength was more linear and rapid when the resonant phase was fixed at 0.6, while with the varied resonant phase the tapering was varied more slowly to the third undulator, and tapered more linearly and rapidly through the last undulator. The fit lines presented above were plotted as grey dotted lines over the simulation results in 2.26b. Slowly varying the resonant phase reduced the particle loss as shown in Figure 2.26f.

Figure 2.27 shows the phase space plotted with a separatrix drawn for the resonant phase at the given position, when the resonant phase was varied throughout z. The figures are plotted with separatrices 0, 0.3, and 0.6 radians of resonant phase (pink, dotted blue, green) for illustration. The figures show how the given resonant phase helped with the amplification.

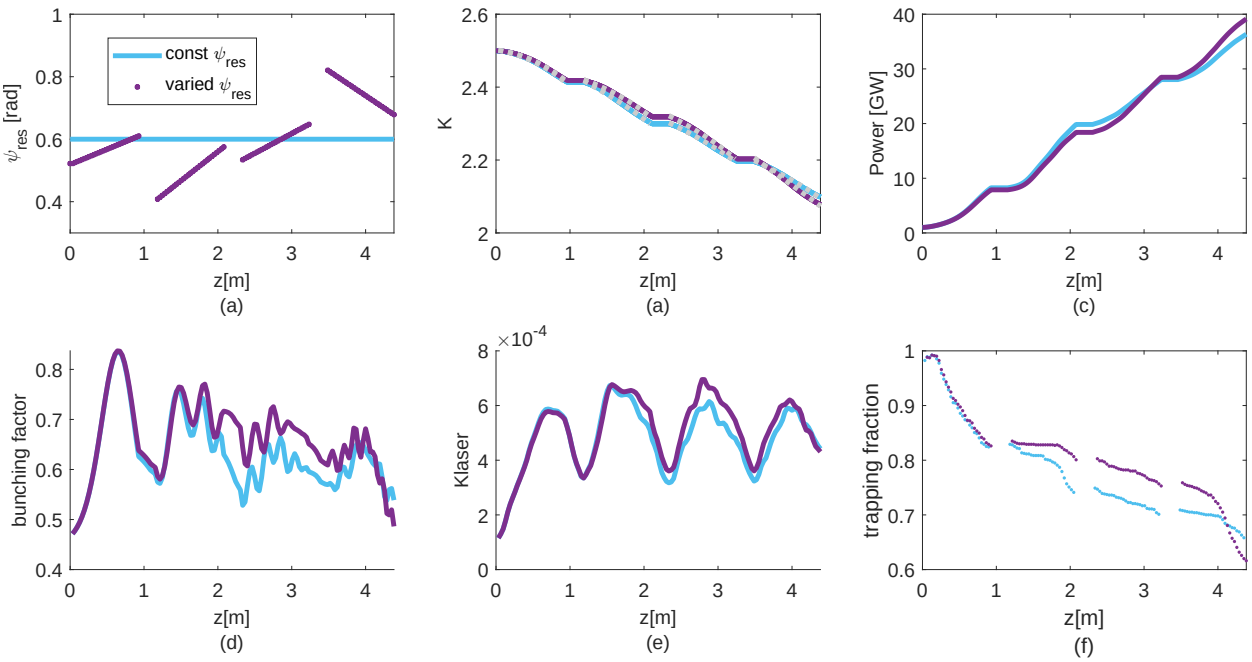

Figure 2.26: Time-independent GIT tapering results for constant resonant phase (blue) and varied resonant phase (red).

With the resonant phase selected by the optimizer, the particles initially fit loosely in the bucket until they reach the third undulator, and then the particles are fit more tightly, extracting more power towards the end. Given the relatively short length of the system, one would expect a tighter bucket to taper more rapidly throughout the modules, but the particular optimization showed that it is preferable to slow down initially and rush at the end. There have been different attempts to vary the resonant phase by solving for more tightly fitting bucket at each period, but there have been no interesting results.

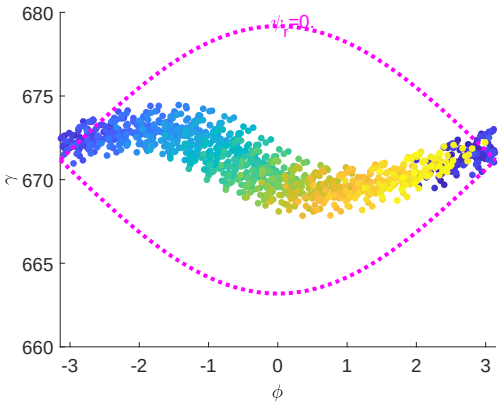

(a)

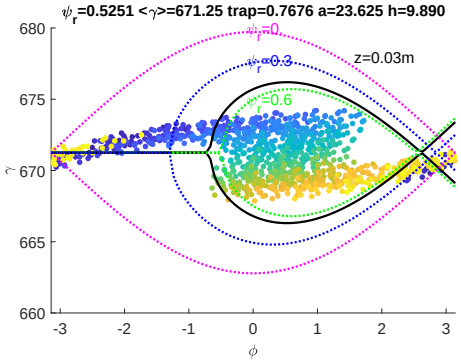

(b)

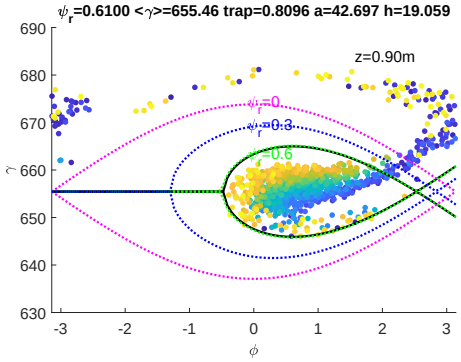

(c)

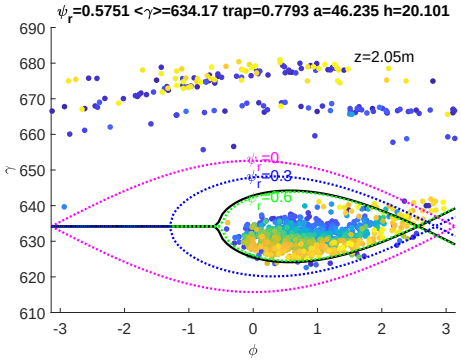

(d)

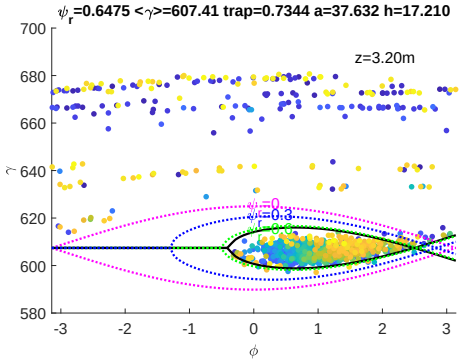

(e)

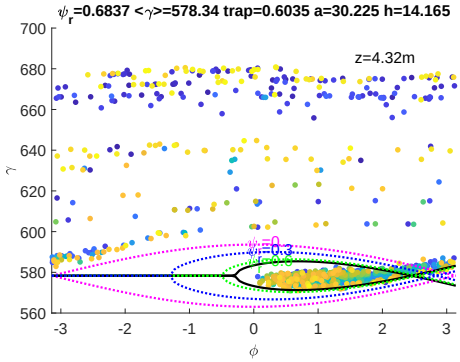

(f)

Figure 2.27: e-beam phase space obtained from the GIT simulation (a) after the modulator (b) at the undulator entrance (c) after THESEUS I (d) after THESEUS II (e) after THESEUS III (f) after THESEUS IV. In the title, ψ_r=resonant phase, $\langle\gamma\rangle$=average energy, trap=trapping fraction, a=bucket area, h=bucket height

2.9 Time-dependent Simulation

In an electron beam the head and the tail of the beam arrive at different times. This section will discuss the time-dependent effects of different temporal distribution given a tapering profile optimized as described in previous sections.

Figure 2.28a,d illustrates examples of electron bunch distributions where in each dimension the beam has Gaussian distribution. In practice due to various effects in the linac transport, the energy distribution can be expressed in terms of the temporal coordinates as

$$p = p_0 + c_1 t + c_2 t^2 + c_3 t^3 + ... \tag{2.16}$$

where the first coefficient c_1 is referred to as the chirp of the distribution, and the rest of the coefficients as nonlinear coefficients. Figure 2.28b,d show a chirp of 1% per mm is applied to the beam, and Figure 2.28c,e show when a nonlinear coefficient is added. Figures (d)-(f) show the current distribution profile in x-axis and the momentum density in y-axis, plotted with a contour plot of time and momentum deviation from average. The current distribution is calculated based on the temporal density and a known value of charge (300 pC). In GENESIS simulation, a six-dimensional distribution file of (x,px,y,py,t,p) can be read into each slice of the distribution. The temporal coordinate of each particle can be converted into the ponderomotive phase according to the laser wavelength. In every slice, which is a temporal width of an integer multiple of the radiation wavelength, the ponderomotive phase corresponds to the temporal deviation from the center of the beam. Conversely, a ponderomotive phase output from GENESIS can be converted to temporal coordinates for ELEGANT or ASTRA.

As of GENESIS version 2, the number of particles in a distribution is limited to 1250k particles. The simulation will read the input distribution of (x,px,y,py,t,p) to create a current profile at each slice as well as the initial particle distribution.

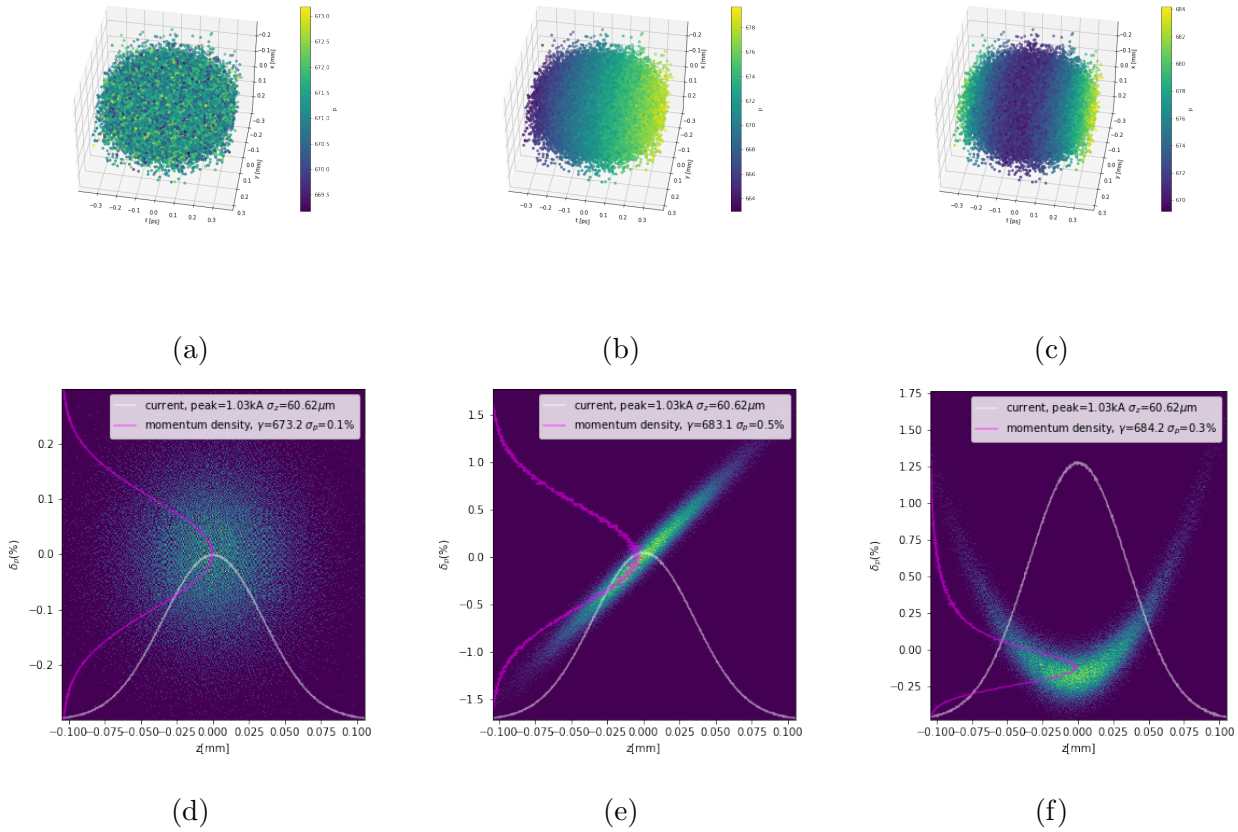

(a) (b) (c)

(d) (e) (f)

Figure 2.28: An illustration of a Gaussian bunch with a bunch length of 36μm with an energy spread 0.1% of the bunch length (a), chirped by 1% (b), and with additional nonlinearity (c).

2.9.1 Initial time-dependent simulation with ideal electron beam distribution

In the initial studies a Gaussian distribution and a flatter distribution were studied to examine basic effects added by temporal dependence. After initializing all of the six-dimensional coordinates of a Gaussian distribution, the temporal profile was flattened by an nth order super gaussian function $\lambda(t) = I_0 \exp[-(t/\sigma_t)^n]$ where n is an even number, adjusting the other parameters to keep the peak current around 1 kA (Figure 2.29a). It was found that with increasing order n, the efficiency increased as a flatter beam more closely resemble the steady-state case assumed in time-independent simulations (Figure 2.29c).

Figure 2.31 shows the details of GENESIS output in time-dependent mode when a flattened current distribution was run through the undulators. As shown in (a) and (b), the particles with sufficient current density participated in amplifying the radiation power. The radiation slippage of around 120 fs agrees with the expected slippage, calculated from $9\lambda_u$ of modulator, $29\times4\lambda_u$, and around $53 + 3\times7\lambda_u$ of drift for a total slippage of nearly 40 μm. Presented in Figure 2.30a and c is the radiation amplification through longitudinal space in z, in which the radiation was amplified to 34 GW. The radiation energy amplification computed from the power was compared with the electron beam deceleration in (d). While the transverse beam size of the electron beam distribution increases slightly over the four undulators due to the tapering, the radiation diffracts dominantly as shown in (f). As already described in the earlier sections about the laser parameter optimization, the radiation waist shown here was not the waist of the seed laser but rather the radiation refraction due to the electron beam distribution behaving as a refractive medium [62, 95, 105]. Figure 2.31a shows the longitudinal phase space computed from the particle distribution output of GENESIS simulation obtained by converting a particle in a temporal slice into a particle at time t. The distribution shows how the particles that were at the right timing maximally decelerate while the other particles that were not trapped experience less deceleration. Figure 2.31b shows how the spectral density grows both in height and width at the position of each undulator exit . The width of the final spectrum was around $\Delta\lambda/\lambda \sim$ 2e-3.

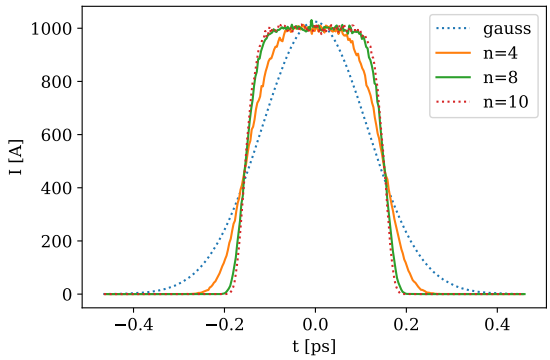

(a)

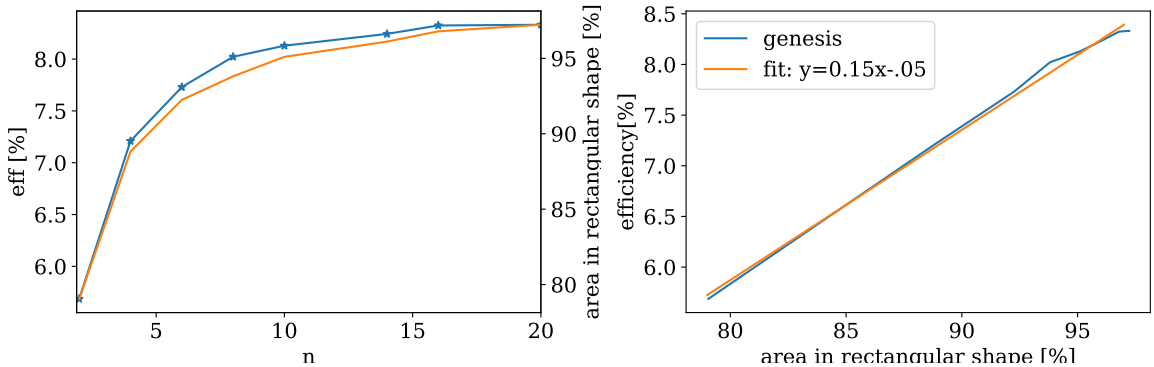

(b) (c)

Figure 2.29: Super-gaussian distributions of n-th order where $n = 2$ represents a Gaussian distribution and the higher order makes a flatter distribution as shown in (a). The peak current and the charge were kept at 1 kA and 300 pC. Distributions with the temporal profiles at different n-th order were run in the time-dependent mode of GENESIS, and showed higher efficiency as the current distribution was flattened. The right-hand side of (b) shows a ratio of the area of the pulse that fills a rectangular pulse, indicating the flatness of a distribution. (c) shows a fit between the distribution flatness and the efficiency, where [FEL efficiency] = 0.15 [flatness] -0.05

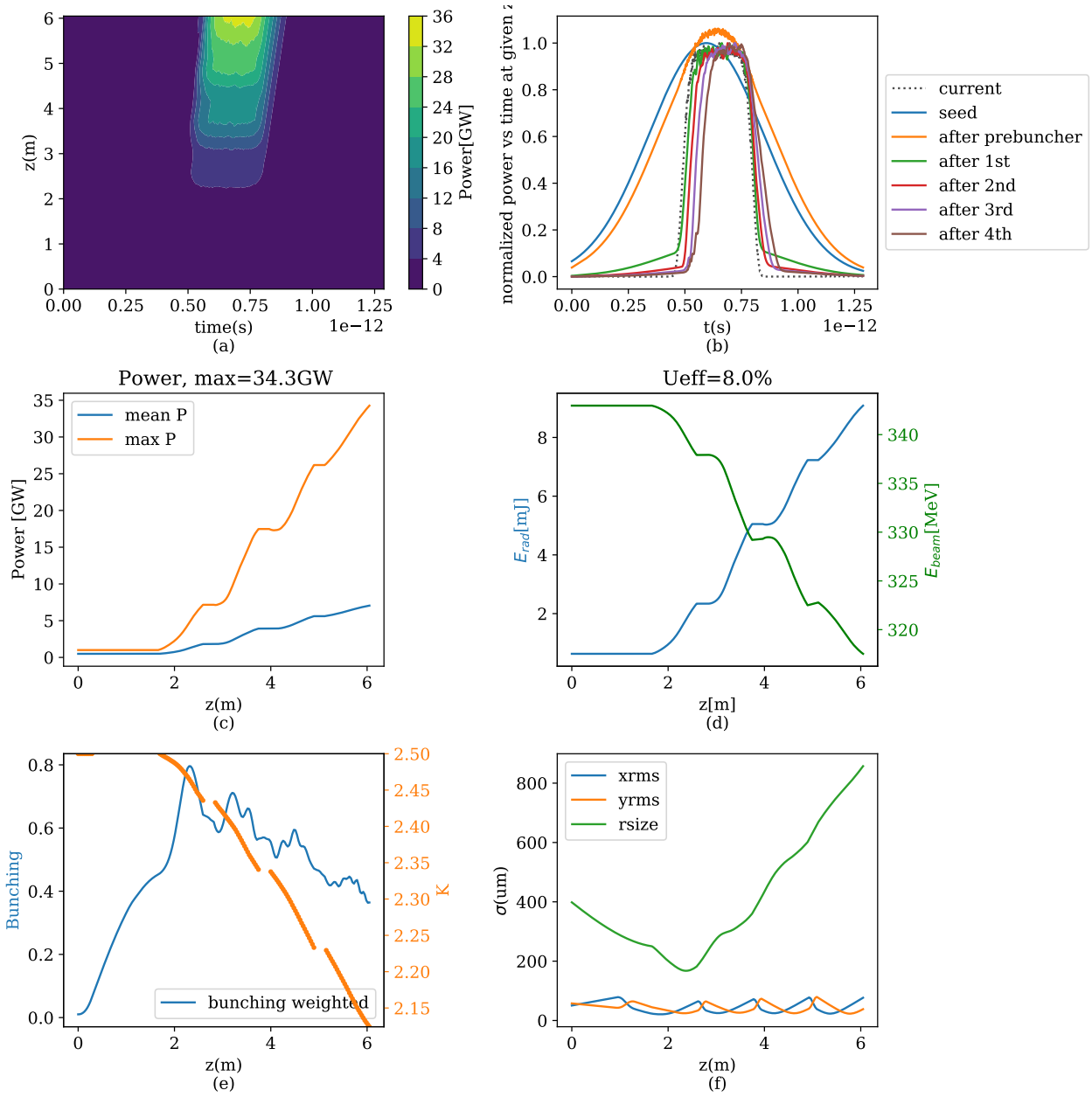

Figure 2.30: GENESIS simulation results in time-dependent mode. Ideal electron distribution with rectangular-pulse shaped current was passed through a prebuncher and four tapered and segmented undulators in the presence of a seed laser.

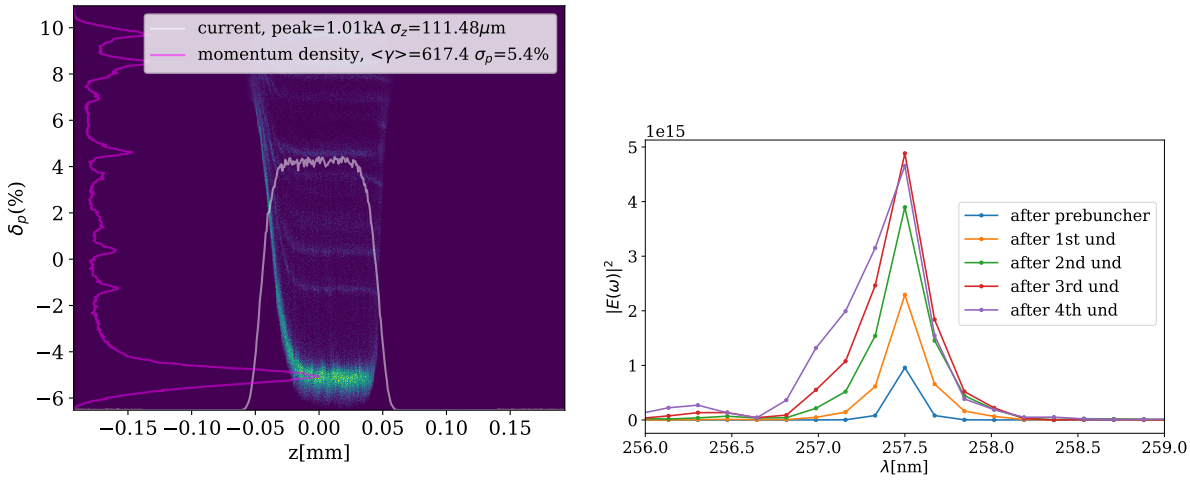

(a) (b)

Figure 2.31: Time dependent GENESIS simulation. (a) Longitudinal phase space output of time-dependent simulation of an electron beam that passed through the four undulators (b) spectral density distribution at the exit of each undulator.

2.9.2 Longitudinal phase space simulation of LEA-TESSA

The beamline in the Linac Extension Area (LEA) starts with a 1.6 cell 2856 MHz photoinjector that operate at 150-300 pC and QE of around 5e-5. Out of the photoinjector the electron beam has a low emittance of around 2mm mrad. The beamline has a single module linac L1 and alpha magnets which are used to bring in the beam from the thermionic RF gun for the APS ring. Depending on the experiment schedule either the beam would run in interleaving mode with APS ring or would run the beamline from the upgraded photoinjector [102]. The next linac L2 brings the energy to 150 MeV, which is the nominal beam energy to operate the bunch compressor. The bunch compressor has four rectangular dipoles that are asymmetrically placed to reduce the CSR growth [14] and has nominal R56 of -.065 m. Then the electrons pass through two more sections of linacs L4 and L5. The nomenclature of L3 is taken by the bunch compressor area. The beam passes through four vertical ramps to reach the Linac Extension Area (LEA), which is a tunnel around 50 meters long that is

used to host various experiments. Currently installed components in the tunnel fill about 17 meters of the space; the last element is a dipole that will be turned off for the TESSA experiment. Figure 2.32 shows an illustration of the electron beam in the TESSA experiment and relevant photos in the beamline.

In the current beamline configuration the electron beam going through the accelerating cavities acquires a strong second order nonlinearity after the bunch compressor.

This can be understood as follows. A Gaussian beam (z_i, γ_i) goes through the gun (amplitude A_g, phase ϕ_g) and the linacs (amplitudes A_1, A_2 and phases ϕ_1, ϕ_2) following the equation:

$$\gamma_f = A_g \sin(kz_i + \phi_g) + A_1 \sin(kz_i + \phi_1) + A_2 \sin(kz_i + \phi_2) \tag{2.17}$$

where the distribution is chirped according to the linac phases ϕ_1 and ϕ_2, and then pass through a bunch compressor with parameters R_{56},T_{566}, and U_{5666}:

$$z_f = z_i + R_{56}\delta_\gamma + T_{566}\delta_\gamma^2 + U_{5666}\delta_\gamma^3 \tag{2.18}$$

where R_{56}, T_{566}, and U_{5666} represent the matrix elements of a bunch compressor and $\delta_\gamma = (\gamma - < \gamma >)/ < \gamma >$. The resulting current distribution becomes skewed because of the nonlinear terms before the bunch compressor.

If one subtracts out the second and the third order terms and passes the beam through the chicane with the same matrix elements, the final distribution becomes less skewed and more compressed. Neglecting the collective effects, one can also completely cancel out all nonlinearities by setting up the system according to the coefficients d_1, d_2, d_3 expanded from the distribution before the bunch compressor:

$$\begin{aligned} \delta_\gamma &= d_1 z_0 + d_2 z_0^2 + d_3 z_0^3 \\ z_f &= (1 + d_1 R_{56}) z_0 + (d_2 R_{56} + d_1^2 T_{566}) z_0^2 + (d_3 R_{56} + 2 d_1 d_2 T_{566} + d_1^3 U_{5666}) z_0^3 + \ldots \end{aligned} \tag{2.19}$$

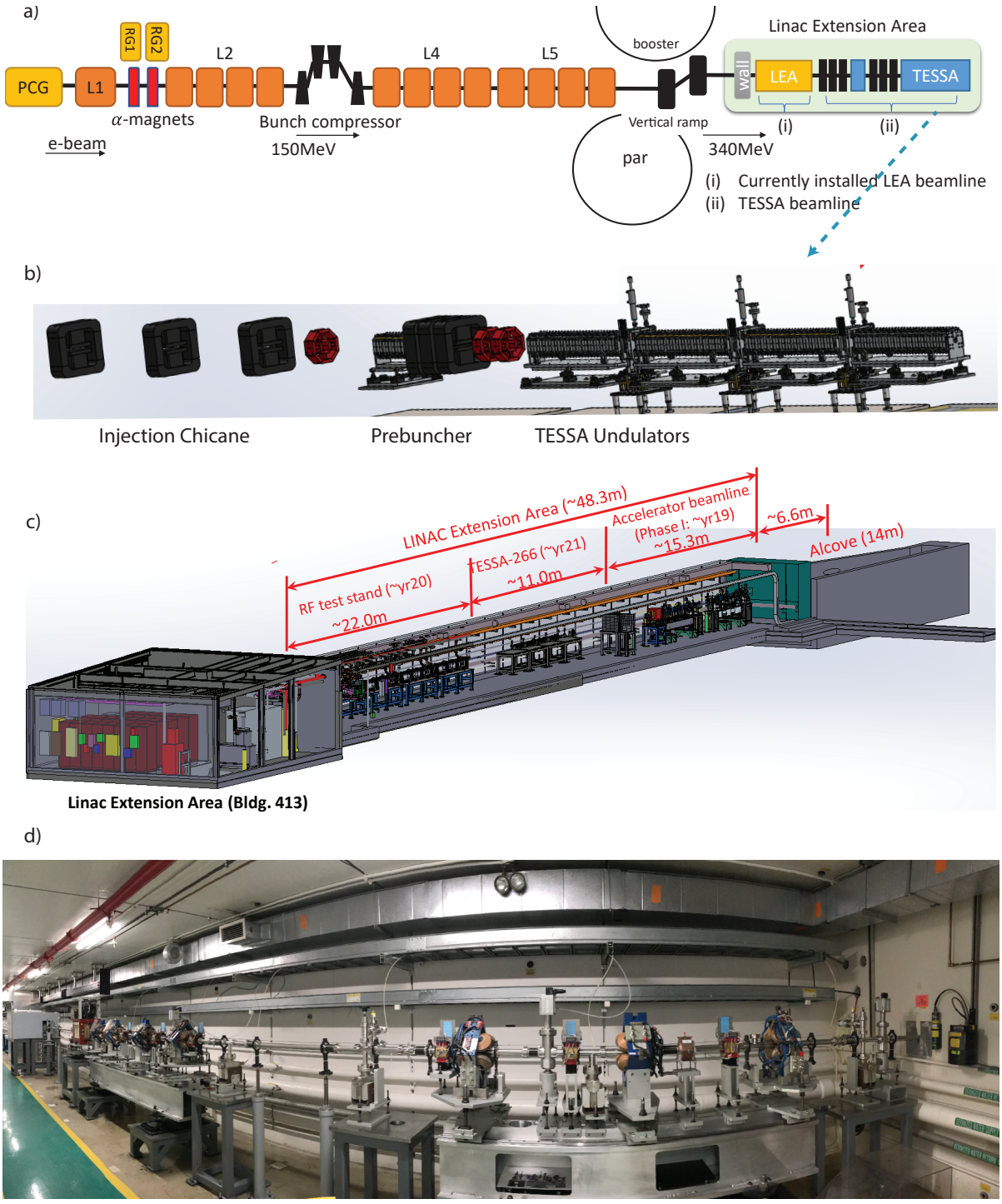

Figure 2.32: APS Photoinjector to LEA Beamline. (a) A schematic drawing illustrating the beamline elements from the photoinjector to the LEA-TESSA setup. (b) A Solidwork assembly view of the beamline elements in the LEA-TESSA setup. (c) A Solidwork assembly view of the LEA tunnel with the experimental setup. (d) A photo of the LEA tunnel.

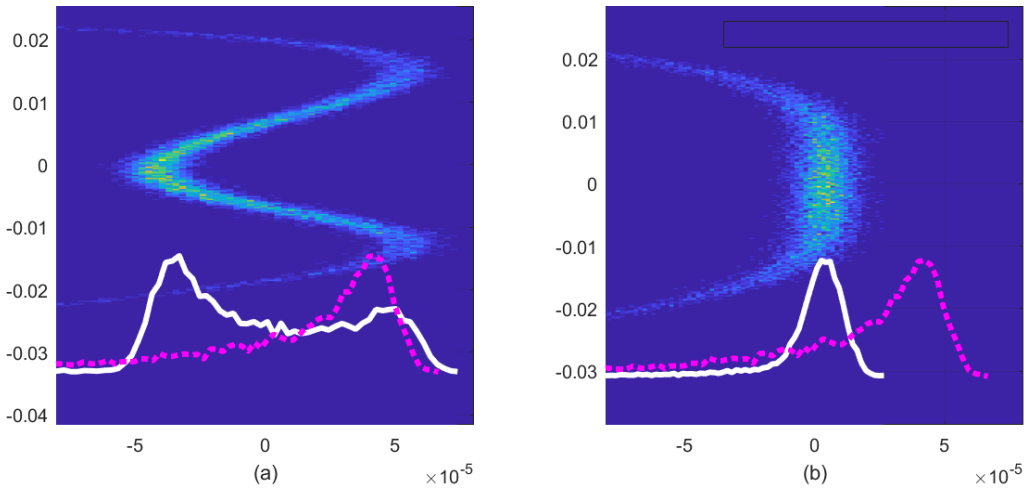

Figure 2.33: Single particle tracking considering a linearizer preceding the bunch compression in LEA beamline shown with different amplitudes and wave vectors (left: $A = 1.2, k = 2500m^{-1}$, right: $A = 0.5, k = 1700m^{-1}$). The white solid lines indicate the current distribution, and the red dashed lines indicate current without the linearization.

In a practical scenario, correcting the terms before the bunch compressor can be done by adding a linearizer to the system to manipulate the distribution before passing through the bunch compressor, and changing the matrix elements corresponds to adding magnets like a sextupole or an octupole to correct the matrix elements T_{566} and U_{5666} to cancel out the RHS of Equation 2.19.

There would be numerous solutions to help with the longitudinal distribution that could be made depending on time and resources available. For the LEA-TESSA system discussed in this document, we chose to investigate a corrugated flat pipe as a linearizer because it was the more convenient option.

Previous studies have shown that longitudinal wake effects due to a corrugated pipe can be used to manipulate the nonlinear terms [5]. A slab structure can be designed to have an adjustable gap size, which can be used to control the amplitude of the wake, while the wave vector is influenced by both the gap and the corrugation characteristics. The transverse

wake effects cause an emittance growth, but positioning two slab structures horizontally and vertically will cancel out the effects to minimize the emittance growth [119].

The single mode wake due to a flat linearizer can be expressed as [4]:

$$w(s) = \frac{Z_0 c}{2\pi a^2} L \cos(kz) \tag{2.20}$$

where $k = \sqrt{\frac{2p}{a\delta g}}$ is the wave vector of the linearizer corresponding to the period p, depth δ, and gap g of the periodic corrugation, and a is the radius or the half-gap of the linearizer. Figure 2.33 shows how the wave amplitude and vector influence the longitudinal phase space computed in single-particle tracking. Compared to the red dashed line, which indicates the current distribution without the linearizer, the distribution can be made more centered or flatter according to the wave amplitude and the wave vector.

The details of an optimal amplitude and wave vector become complicated once the collective effects are considered. There are around 100 meters of drift space to reach the LEA tunnel, and the longitudinal space charge effects add up as the beam passes through the drift space. The coherent synchrotron radiation effects caused by the dipole magnets in the chicane and the vertical ramp also influence the energy spread and the emittance of the beam. Optimization with the collective effects was studied by running ELEGANT simulation from the entrance of linac L2 to TESSA entrance. The input distribution from the photocathode and the first linac L1 was optimized in an ASTRA simulation taking into account the transverse emittance and the beam size needed for the beamline. The best possible distribution without a linearizer (left side) is compared with the best possible distribution with a linearizer (right side) in Figure 2.34. Figure 2.34a shows the initial distribution before the bunch compressor without linearization. The phase and the amplitude of the linac were adjusted to get a smaller nonlinearity, but the second order is still concave down while the first order coefficient would be positive. Considering $R_{56} \sim -1/d_1$ this means $T_{566} > 0$ while $d_2 R_{56} > 0$, so the two will not cancel out the second order nonlinear term in Equation 2.19. In the case shown in Figure 2.34b, the second order term is small and positive (around 50

m^{-1}) and helped with the asymmetry of the distribution. The final distribution shown in (e) and (f) are input distribution for the FEL simulation. The increased noise in both cases is due to the longitudinal space charge effects causing microbunching instability and density modulation due to travelling at high current through 150 m. The noise can be suppressed in simulation depending on the filter parameters, but it is undetermined whether the effects are physical. The microbunching instability has been known to degrade the seeded FEL interaction. Adding a laser heater (a setup of four-magnetic chicane and a short undulator) can improve the beam quality in the case the effects are physical[120].

Distribution with the linearizer can give up to 3% extraction efficiency in the longitudinal phase space. The longitudinal phase space matching could improve up to 5% with the same current distribution if the energy spread were controlled, but the energy spread from optimized settings remained around 1-2%, an order of magnitude greater than ideal. The high double-hump peak current can be improved by adjusting the chicane matrix elements with an octupole [106], but just as a sextupole it would be difficult to adjust the phase advance and the emittance growth with the limited space available.

Alternative solutions that were considered during the LEA/TESSA project period were placing sextupoles and an octupole in the bunch compressor, placing a x-band linearizer in place of the bunch compressor and moving the bunch compressor to the LEA, adding a sextupole in the vertical ramp to the LEA, or adding a secondary bunch compressor. Nevertheless, the emittance growth due to adding a sextupole and/or an octupole will be difficult to control due to the lack of space in the currently installed bunch compressor. Ideally it should be possible to reduce the emittance growth by adjusting parameters such as the betatron phase advance and the chromaticity.

TESSA collaborators also explored the solution of utilizing the vertical ramp by installing a sextupole in the dogleg system, but energy spread and emittance growth needed more evaluation. Other solutions like moving the bunch compressor, adding a x-band linearizer, or adding a secondary bunch compressor were too costly for the project period.

Without considering the monetary and the time-line aspects of the project, using two-stage bunch compressors with nonlinearity correction would be another good solution for an FEL experiment [109, 106]. Sending a low peak current through the 150 m to the LEA tunnel and then compressing the beam for the TESSA experiment will also help reducing the space charge effects.

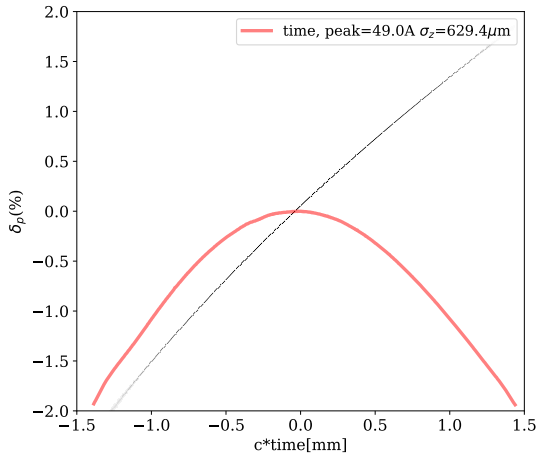

(a)

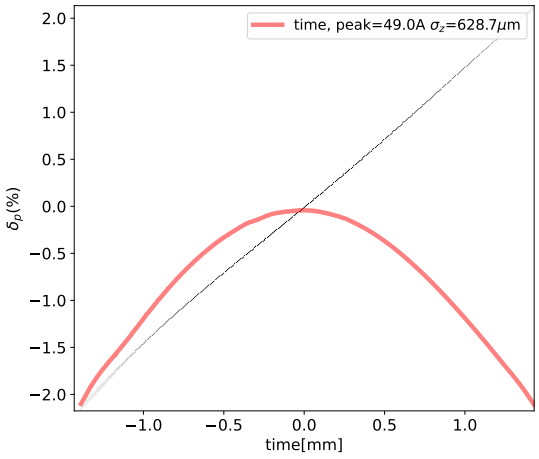

(b)

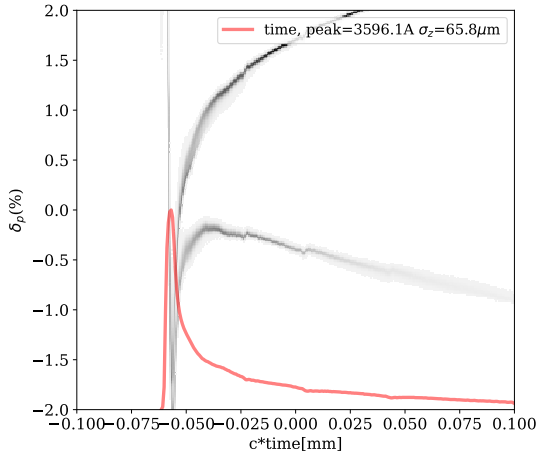

(c)

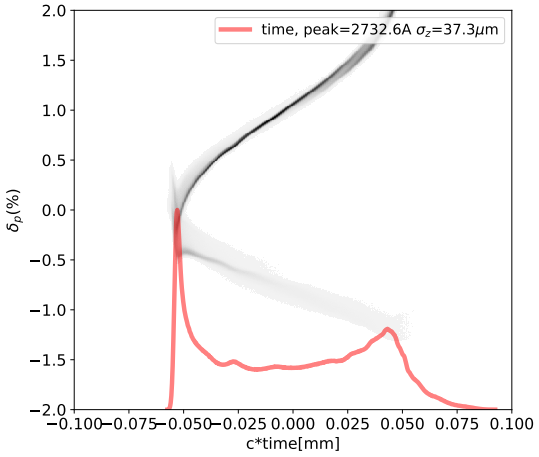

(d)

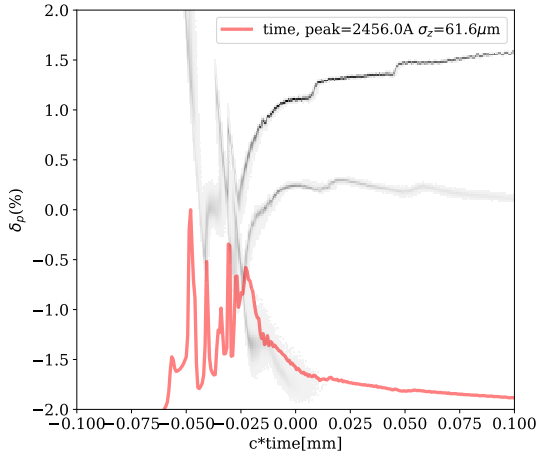

(e)

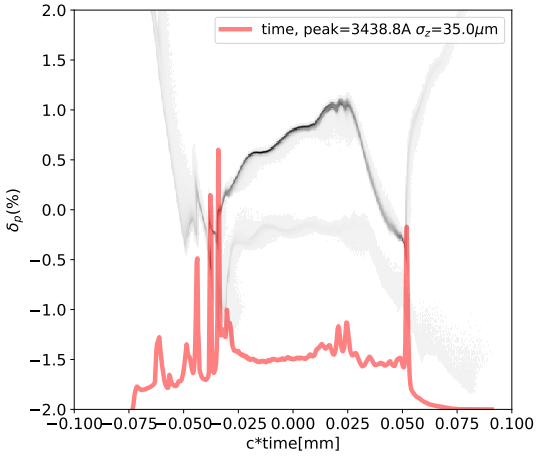

(f)

Figure 2.34: Longitudinal phase space distribution from ELEGANT simulation without (left) and with the linearizer (right). (a) and (b) show before the bunch compressor, (c) and (d) show after the bunch compressor, and (e) and (f) show at TESSA prebuncher entrance. The

2.10 Wake Effects on TESSA266

Wakefield effects are due to the electromagnetic interaction of a test charge due to the beam charges in front of it. The wake effects are influenced by the characteristics of the vacuum chamber that the charges travel through. The vacuum pipe for the TESSA undulator is a thin stainless pipe of OD=5.55mm and ID=4.54mm. This is smaller than that of the predecessor undulator used for the Rubicon and the Nocibur experiment, which had a gap greater than 12 mm [107]. If the pipe were perfectly conductive and smooth, it will not generate electric fields when a charged beam passes through. Stainless steel materials have a finite conductivity of $3.2 \times 10^{17} s^{-1}$, greater than that of aluminum materials with $1.3 \times 10^{16} s^{-1}$. The longitudinal wake of a cylindrical resistive pipe can be derived from Maxwell's equations: [17]:

$$W(s) = \frac{16}{a^2}\left[\frac{e^{-s/s_0}}{3}\cos\frac{\sqrt{3}s}{s_0} - \frac{\sqrt{2}}{\pi}\int_0^\infty \frac{dx x^2 e^{-x^2 s/s_0}}{x^6+8},\right] \tag{2.21}$$

where s_0 is the characteristic distance $s_0 = (ca^2/2\pi\sigma)^{1/3}$ a parameter that depends on the pipe radius a and the conductivity σ. The wake field effects due to an electron bunch can be estimated by the convolution integration over a beam distribution.

$$W_\lambda(s) = Ne^2 \int_{-\infty}^{\infty} \lambda(s-s') w_l(s') ds' \tag{2.22}$$

where $\lambda(s)$ is a normalized charge distribution and Ne is the total charge of a bunch. Simulations of the wake at different radii shows that the small vacuum chamber would not be as significant considering that the bunch wake magnitude is saturated around 4-6 mm of inner diameter.

Figure 2.35(b) shows the wake field due to a Gaussian current distribution of 300 pC and 36 μm. In a GENESIS simulation, energy loss at each slice is subtracted. The simulation shows that there would be 4 percent-difference in efficiency from 5.33% to 5.09% when taking into account the wake effects.

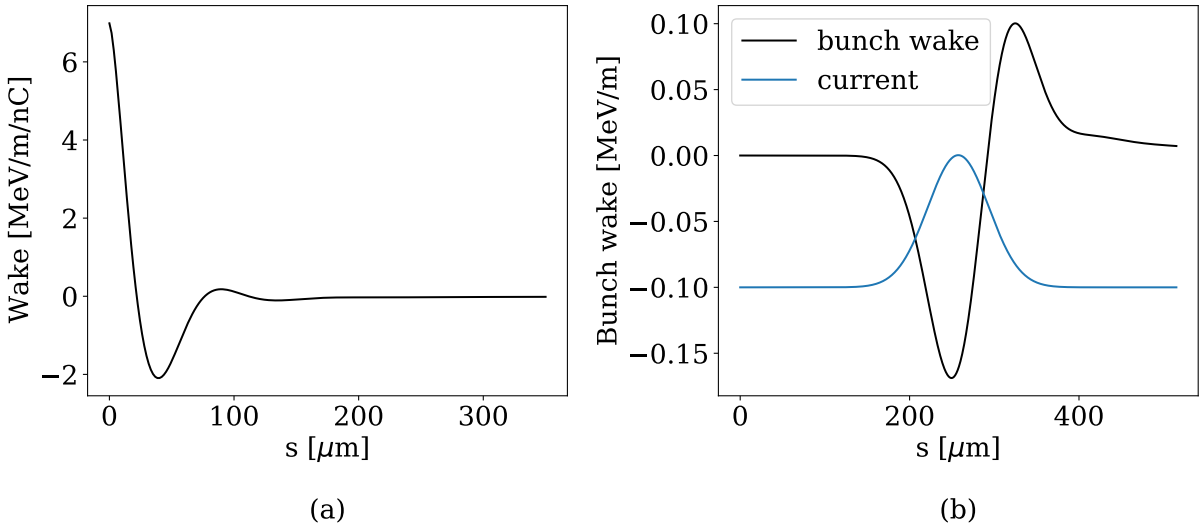

Figure 2.35: Wake effects due to the resistive wall of a round pipe with inner radius 4.54mm, where (a) shows wake function and (b) shows bunch wake (black) due to a Gaussian current distribution (blue) of charge = 300 pC and bunch length 36μm (normalized and shifted for visualization).

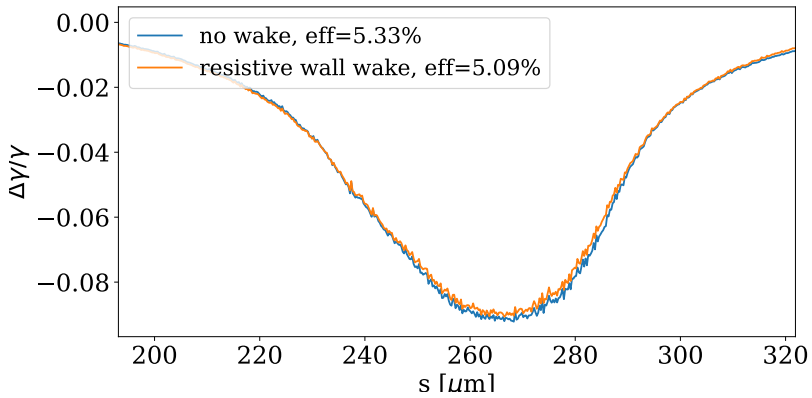

Figure 2.36: Genesis simulation of optimized tapering without (blue) and with (orange) wake due to a resistive wall, with an inner diameter 4.54mm. The result showed that there would be 4 percent-difference in efficiency due to the resistive wall.

2.11 Tolerance Studies

The study of tolerance in the TESSA simulation parameters was done by running the Genesis simulation based on a magnetic lattice with the optimized tapering scheme. While the effects of the parameters based on the tapering optimization could be an interesting subject for design purposes, the experimental tolerance should be based on an already optimized tapering scheme, resembling a tuned and measured undulator in a beamline. Changing one or two simulation parameters from the ideal, similar to how they would diverge in the laboratory, one can estimate whether the experiment will produce a measurable and publishable result despite the errors that would emerge in reality. We set the minimum acceptable amplification as -20% from the ideal value. Although an amplification less than this amount could still be measurable, a lower tolerance limit would not be safe because some of the errors would add in quadrature.

2.11.1 Magnetic Tolerance

The magnetic tolerance indicates how close the undulator field should be to the ideal in order to measure the amplification. A potential problem that can increase the magnetic error on the axis would be the deviation of the magnitude of and the angle of the magnetization in each of the undulator magnets. The undulator components such as the strong backs, the magnet holders, and the tuning plates should be engineered according to the tolerance estimate. In addition, the magnetic measurement tools should have sufficient precision to verify such tolerance estimate. In order to include the magnetic errors due to realistic circumstances, the field at each period was changed for a set of pseudo-random numbers generated within the range of the given percentage. Figure 2.37(a) shows how the change in the magnetic error would affect the radiation amplification in the time-independent GENESIS simulation. The time-independent scheme is sufficient to study the magnetic error because the undulator vector potential parameter is slice-independent. The simulation showed that the magnetic

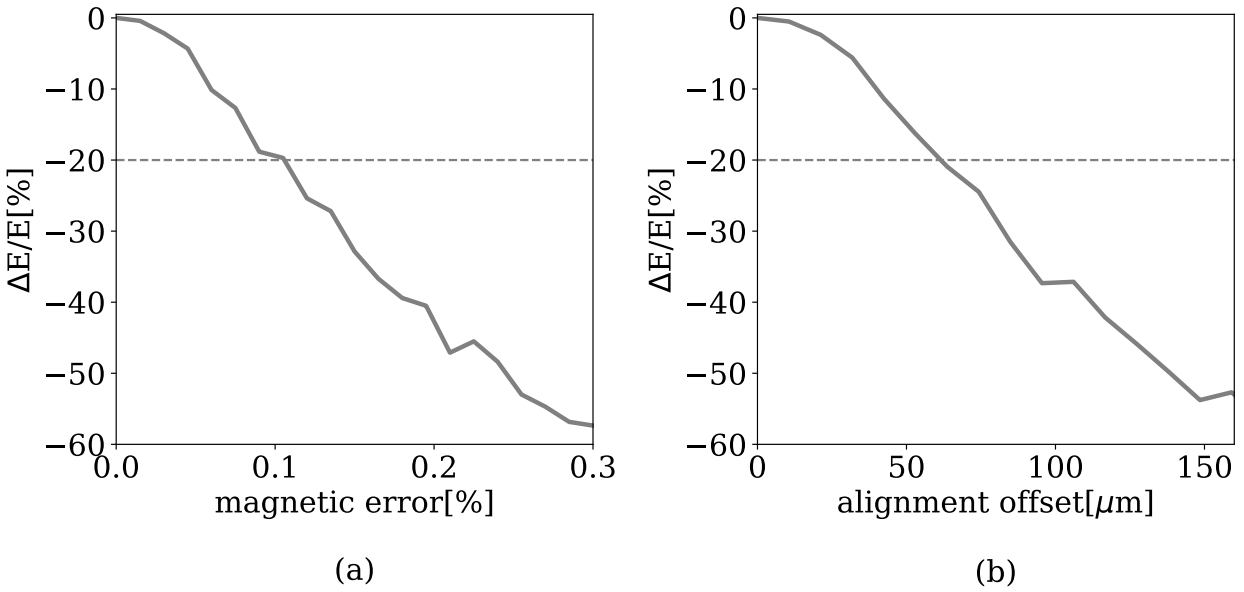

Figure 2.37: The tolerance in the magnetic strength and the alignment error. The magnetic strength was varied by changing the undulator vector potential parameter K per period from the optimized tapering in the GENESIS simulation. Alignment offsets were varied by shifting the beam position at each undulator entrance. The dashed lines show the -20% tolerance level set for the experiment.

error tolerance was 0.1%. In the LEA-TESSA scheme the initial vector potential parameter is 2.5, and with a 3.2 cm undulator period this gives a magnetic error tolerance is 8 gauss. This parameter is critical in the construction because the tuning screw should be precise enough that when it changes the on-axis field the gradient should be smaller than the tolerance, and also in the measurement setup because the probe sensitivity should be better than the target tolerance.

2.11.2 Alignment Tolerance

Aligning a system of four 1-meter-long undulator segments will require some engineering efforts, and realistically there would be some alignment error between each undulator. The

simplest way to study the alignment in the GENESIS simulation is to shift the electron beam particle positions after each undulator section while the undulator field stays on-axis. Figure 2.37(b) shows the alignment tolerance is 50μm. Another way to study the alignment would be to run the simulation in GPT, along with the breaksection, where it would be possible to change the angle of the axis for the undulator field profile. Then the parameters, such as the energy spread or the centroid position, would indicate how the beam may decelerate.

2.11.3 Simultaneous studies of magnetic and alignment error

In practice, both the magnetic field and the undulator alignment will have errors. It is important to study how the two parameters will add to the overall uncertainty. Figure 2.37 shows that the parameters add in quadrature. The magnetic error of 0.1% and the mechanical offset of 40 μm will add to the total error of -20% decrease in efficiency.

2.11.4 Energy Jitter

Electron beam energy varies per each shot due to numerous factors in the laboratory, such as the laser time of arrival jitter of the gun, the vacuum environment, the RF power fluctuations, or the cavity temperature. The energy jitter in the LEA beam is 150 keV up to 500 MeV, so less than .05%. In the time-independent GENESIS simulation, the initial energy entering the TESSA beamline is simply a single input parameter. For the longitudinal phase space of the time-dependent scheme it is better to consider the change of the energy in the input distribution. The average energy of a 6d-distribution was shifted according to the percentage in the error (Figure 2.39a). The simulation showed that the energy jitter should be better than $\pm$0.1%.

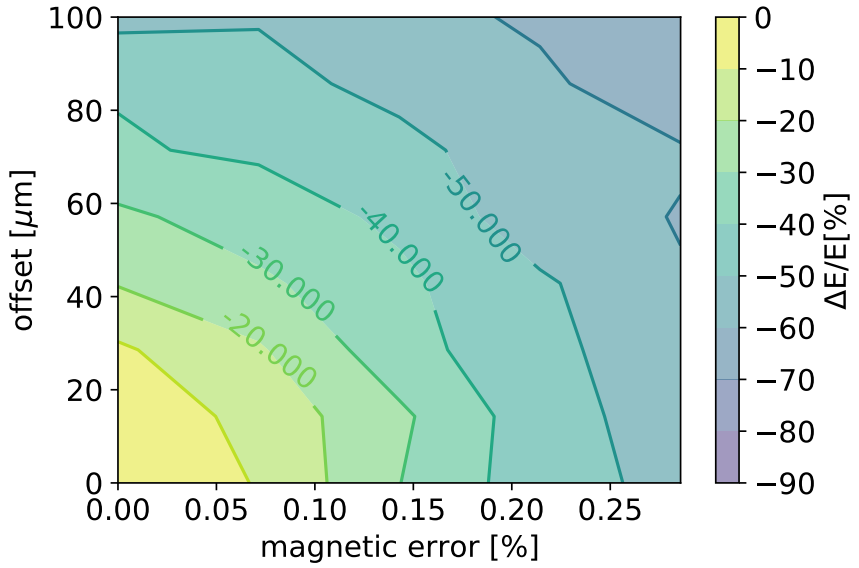

(a)

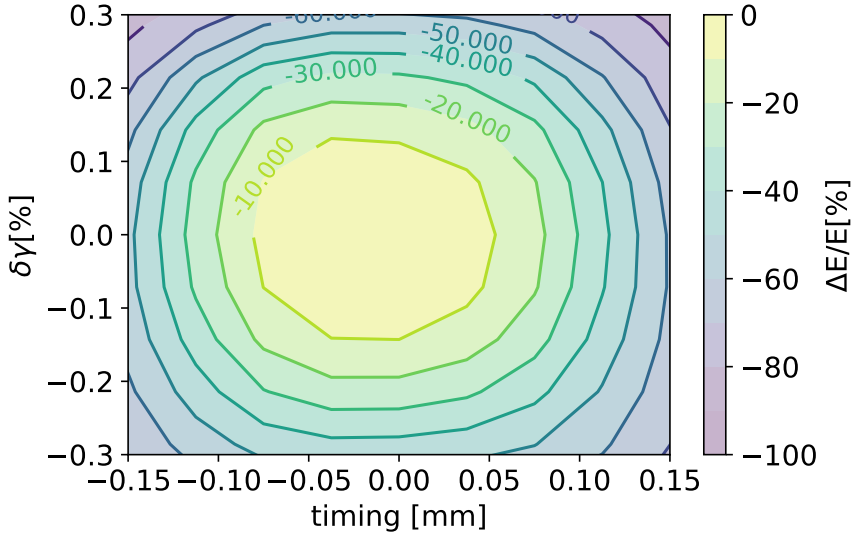

(b)

Figure 2.38: A study of simultaneous variation in (a) alignment and magnetic strength and (b) timing and energy. The studies showed that the parameters add in quadrature.

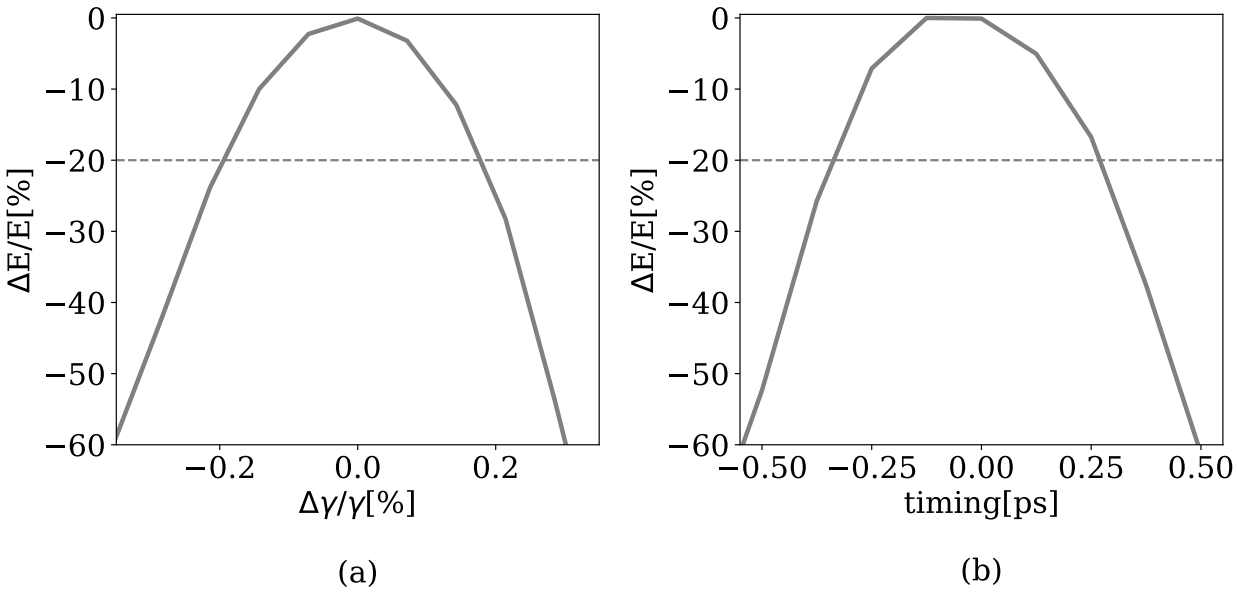

Figure 2.39: Energy and temporal jitter studied in time-dependent Genesis simulation using an ideal Gaussian distribution.

2.11.5 Beam Arrival Time

The arrival time of the seed laser can vary based on how the laser and the electron beams are set up. The beam arrival time jitter in the APS LEA beam is 200 fs. To simulate the beam timing in the GENESIS simulation the time difference between the electron beam and the seed laser was varied. Figure 2.39b shows that the timing jitter of 300 fs would be acceptable for the experiment.

2.11.6 Energy Spread

The energy spread parameter is another important parameter in free-electron laser studies. The energy spread for a good FEL interaction should be smaller than the Pierce parameter [86], which is 9×10^{-3} with $K = 2.5$, $\gamma = 671.2$, and $\sigma_x = 46\mu m$. The expected energy spread is .1% of the average energy. As shown in Figure 2.40, the FEL interaction degrades exponentially as the energy spread deviates from 0.1%, and should be less than 0.15% for

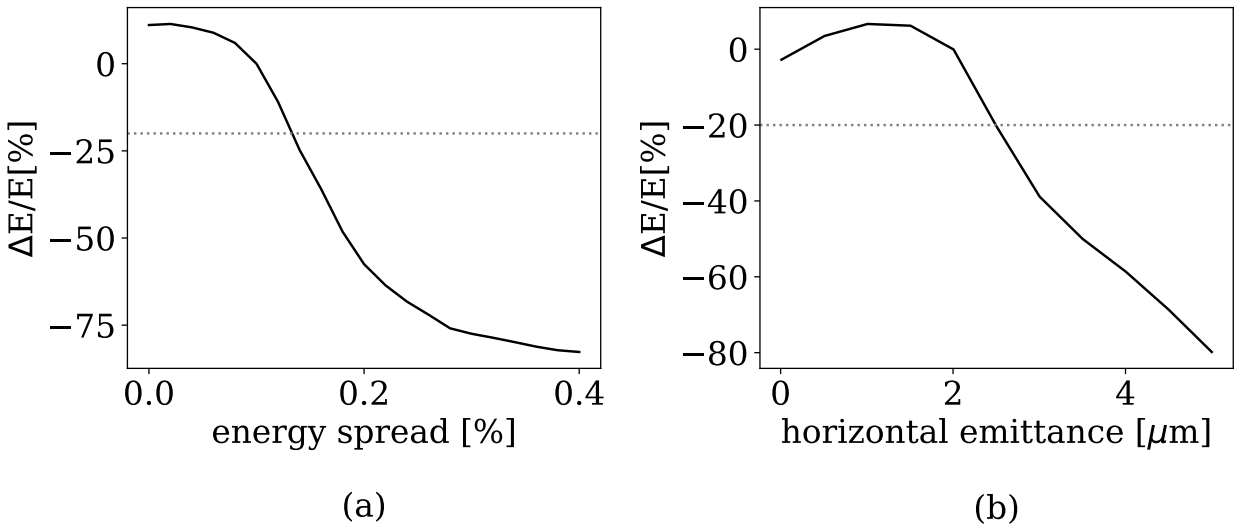

Figure 2.40: Tolerance studies in the time-independent GENESIS of TESSA-266 where the simulation showed that the energy spread should be less than 0.15% (a), and horizontal emittance should be less than 2.5μm in order for a tolerance limit of -20% (b).

the tolerance limit of -20%.

2.11.7 Transverse Emittance

In the initial design studies, the transverse emittance is 2 mm-mrad. This is 3×10^{-9} in the geometric emittance and is less than $\lambda/4\pi = 20 \times 10^{-9}$ as required for a good FEL interaction[86]. As the transverse emittance increases, the interaction degrades because the ratio between the electron beam and the laser spot size ratio is critical in their interaction. The simulation showed that emittance should be less than 2.5 μm to be above the tolerance limit as shown in Figure 2.40.

2.11.8 A Summary of Tolerance Studies

Table 2.4 summarizes the tolerance intervals obtained for all of the parameters including laser waist position, Rayleigh range, energy spread and transverse emittance. These results

are important not only to give an idea of the beam stability required for the experiment, but also as they allow to specify the level of accuracy of the various diagnostics used to characterize the TESSA-266 input beams.

Tolerance / Jitter Studies		
Parameter	Unit	Value/tolerance
Relative magnetic errors	%	± 0.1
Beam energy jitter	%	±0.2
Undulator section alignment	μm	±60
Time of arrival	ps	±0.35
Minimum input seed power	GW	0.5
Energy spread	%	<0.15
Transv. emittance	mm-mrad	<2.5

Table 2.4: Tolerance and jitter studies of key parameters in TESSA-266. The values represent the deviation from the nominal parameters which would be acceptable for the experiment.

2.12 Post-Undulator Diagnostics

In TESSA electron beam deceleration process, the electrons trapped in the ponderomotive bucket will decelerate by around 10% of their initial, while the detrapped electrons remain at higher energy. This section will explore design plans for electron beam energy diagnostics that could energy spread up to 15%. In addition to 15% energy spread due to the FEL deceleration, it would be helpful to also be able to measure less than 0.1% energy spread which is the nominal energy spread. In this way, the spectrometer can be used during the installation process to evaluate the beam after the prebuncher.

In the temporal aspect of the bunch length, we can assume a Gaussian or a flat distribution which would have 30-100μ (100-300 fs) of bunch length for 300 pC. This section presents design studies for after-undulator electron beam diagnostics that were planned with the TESSA collaborators.[1]

Some of the key parameters in designing a spectrometer are the energy spread of interest and the available drift space for the diagnostics. The best energy resolution of a spectrometer is achieved when the e-beam size is minimized at the measurement screen, while the dispersion is large enough at the bending magnet [116]. Given that there is a sufficient space for the diagnostics (around 10 meters), the dipole does not have to be very strong to achieve a sufficient vertical dispersion. Electron beam with energy spread $\delta_E = \frac{\Delta E}{E}$ after a spectrometer of length L, bending angle θ_b, and radius of curvature ρ would drift through space of distance D following the vertical dispersion of the transport matrix R_{36}:

$$\begin{aligned} y &= R_{36}\delta_E \\ y &= (\rho(1-\cos(\theta)) + D\sin(\theta_b))\delta_E. \end{aligned} \tag{2.23}$$

[1] Although a technical note was not published due to the complicated status of TESSA project, the work presented here was planned with A. Zholents as a TESSA collaboration during the SCGSR period, where he helped with the analytic studies and the design choices for the diagnostics presented in this section.

which can be written as

$$\begin{aligned} y &= \left(\frac{L}{\theta_b}\left(1-\left(1-\frac{\theta_b^2}{2}\right)\right)+D\theta_b\right)\delta_E \\ y &= \left(\theta\left(\frac{L}{2}+D\right)\right)\delta_E. \end{aligned} \tag{2.24}$$

In other words, the electrons passing through the bend magnet will deflect to different angles according to their energy, and their overall difference in energy would be related to the overall vertical beam size at the screen. Therefore, assuming a 1.5 inch screen size, an energy spread 0.15, a drift space of 2.5 m, and a 0.1 m bend magnet, the bend angle should be around 5°. One would require a larger bend angle if there were a less drift space available, but otherwise it would be more cost-efficient to consider a smaller deflection angle as a design parameter.

Moreover, the vertical beam size at the screen position should be as small as possible to improve the resolution, so $\sigma_y < R_{36}\delta_E$ will be critical when considering the focusing.

In the temporal side, we plan to use an horizontally deflecting cavity. The deflecting voltage is chosen based on how the electron beam should be kicked. The horizontal kick angle on the electron beam due to a deflecting cavity of voltage V_c, cavity frequency ω_c, and electron beam energy E during time τ can be expressed as[101, 1] :

$$x'(t) = \frac{eV}{E}\sin(\omega t). \tag{2.25}$$

The deflecting cavity affects the energy spread of the electron beam, so pushing too much on the time resolution will negatively affect the general performance of the longitudinal phase space diagnostics. This effect can be explained by Panofsky-Wentzel Theorem which says the curl of the integrated impulse, or the wake potential is zero.

$$\frac{\partial p_x}{\partial z} - \frac{\partial p_z}{\partial x} = 0 \tag{2.26}$$

Given that the energy spread can be expressed in terms of cavity voltage and frequency

$$\delta_E = \frac{\sigma_E}{E} \sim \frac{eV}{cE}\omega\sigma_x, \tag{2.27}$$

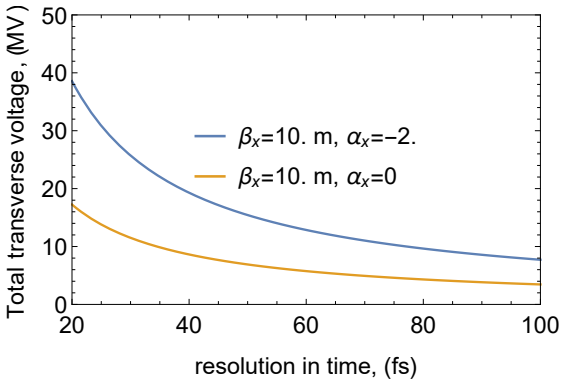

(a)

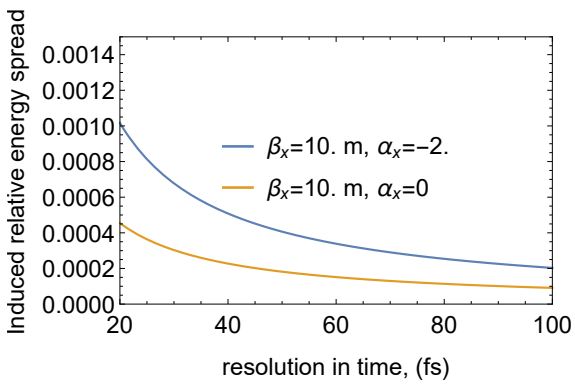

(b)

Figure 2.41: (a) Temporal resolution at different cavity voltage and the transverse parameters (b) Energy resolution at given temporal resolution based on Panofsky-Wentzel theorem

the energy spread can be expressed in terms of in terms of the temporal resolution τ achieved by a given cavity voltage V

$$\delta_E = \frac{1}{\tau}\sigma_{x'}\sigma_x, \tag{2.28}$$

which can also be expressed in terms of the Twiss parameters as

$$\delta_E \tau = \epsilon(1+\alpha^2). \tag{2.29}$$

Interestingly, the energy and the temporal resolution are limited by each other. If the emittance and α were constant, the multiplication of the energy and the temporal resolution should be constant. Therefore, one would find the best temporal resolution while also considering the induced energy spread and energy resolution required for the system.

Presented in Figure 2.41a is the temporal resolution given at different transverse voltage, where larger β_x and smaller α_x is advantageous to get better resolution with the same cavity voltage based on Equation 2.25. In addition, at a given temporal resolution one can compute the induced energy spread based on 2.29 as shown in Figure 2.41b.

Based on the initial design of spectrometer and the deflecting cavity, both elements would benefit from a larger beta function in their position and smaller beam size on the

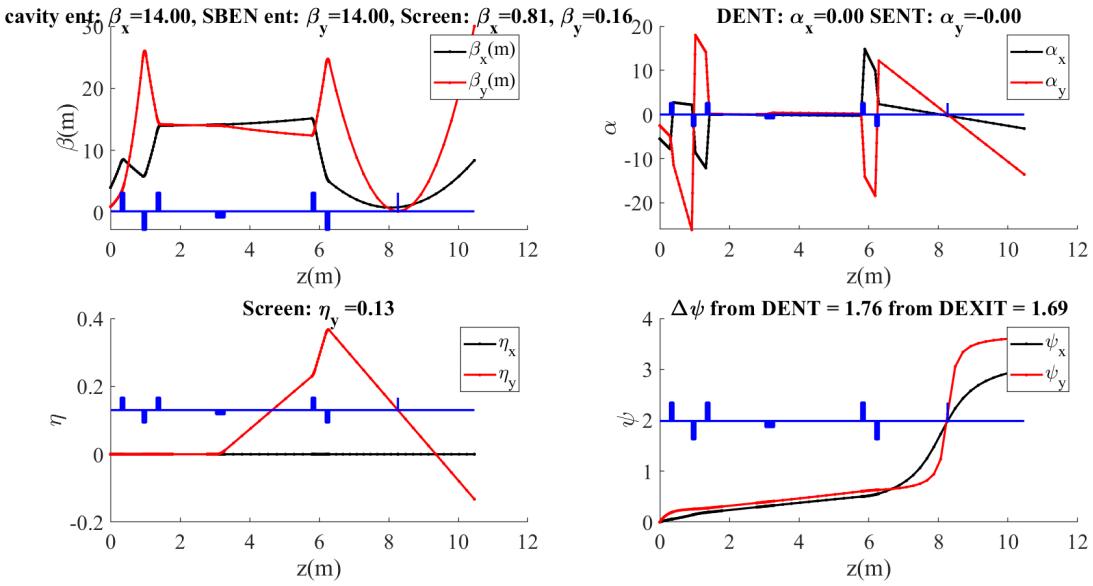

Figure 2.42: Twiss parameters, dispersion, and phase advance throughout the after undulator diagnostics section

screen. Accordingly, a five quadrupole system was presented as a final design, where three quadrupoles before the deflecting cavity increase the beam size horizontally and vertically, and the last two quadrupoles focus the beam size to fit on screen (Figure 2.42).

Figure 2.43a shows the electron beam particle distribution output from the GENESIS simulation, where the distribution is re-scaled based on the current density at each slice, and Figure 2.43b shows the on-screen image output of the ELEGANT simulation after the beam pass through the after-undulator diagnostics section, with a spectrometer of 0.25 m at a 5° bend angle, 1.2 m deflecting cavity at 15 MV, and five quadrupoles of 0.104 m with geometric strengths up to 15 m^{-1} (15-27 T/m at 300-343 MeV).

The decelerated distribution has different transverse beam parameters in each energy-slice of the beam, so selecting the most decelerated portion of the particles to fine-tune the quadrupole strength helps with the visualization. After fine-tuning the parameters based on the lower-energy potion of the beam, the Twiss parameters were $\alpha_x, \alpha_y \sim 0.5$, $\beta_x, \beta_y \sim$

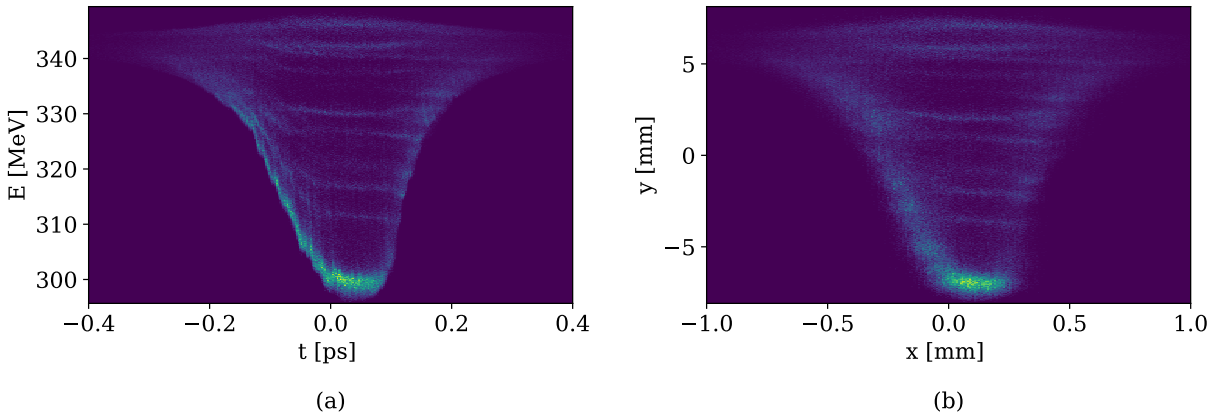

Figure 2.43: (a) Longitudinal phase space distribution of e-beam from TESSA-266 from GENESIS simulation (b) Transverse beam distribution on screen after the diagnostics from ELEGANT simulation.

$9, 12$ m at the deflector and the bending magnet respectively, and at the screen were $\alpha_x, \alpha_y \sim 1.7$ and $\beta_x, \beta_y \sim 1.2, 0.4$.

Finally, the resolution of the diagnostics was studied by changing the energy spread and the bunch length of an input Gaussian beam throughout the same lattice (Figure 2.44) where the beam showed linear relationship in beam distribution parameters to on-screen beam size up to 100 fs and 0.1%.

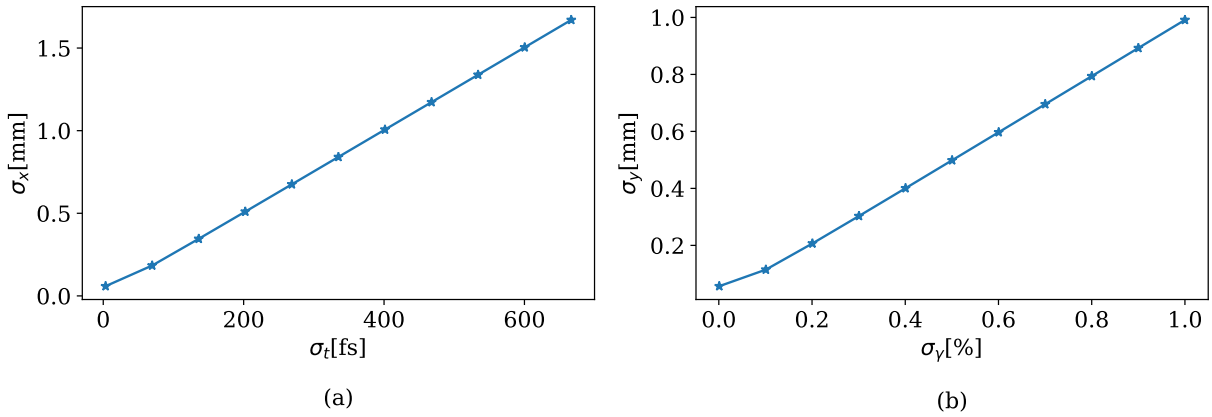

Figure 2.44: Temporal and energy resolution of the after-undulator diagnostics.

2.12.1 TESSO

The LEA-TESSA simulation studies have furthered the understanding of how to improve the tapering to maximize the efficiency. The next big steps in the project are to demonstrate the oscillator setup of the TESSA system and to move towards a shorter radiation wavelength.

To increase the average power, the TESSA system should be in an oscillator setup with a high repetition rate. While the system uses prebunched electron beams and tapered undulators, a portion of the undulator radiation is sent back to the prebuncher entrance using a beam splitter or a mirror with a hole. A lens is placed to focus the beam back to the initial spot size. By optimizing the transmission and the optical setup, an FEL oscillator outputs a stable amount of power if an input radiation with a suitable power and a spot size is fed back to the undulator at every passes. According to the previous simulation studies, a system of e-beam energy 250 MeV, radiation wavelength of 1 μm, and undulator vector potential 4.2 can generate an average power up to 250 kW [31] (Figure 2.45a).

Figure 2.45b shows an example of time-independent simulation output given a TESSO system at 257.5 nm radiation wavelength. Ten percent of output radiation travels back to the cavity and passes through a focusing lens of 4 meters, and returns to the prebuncher

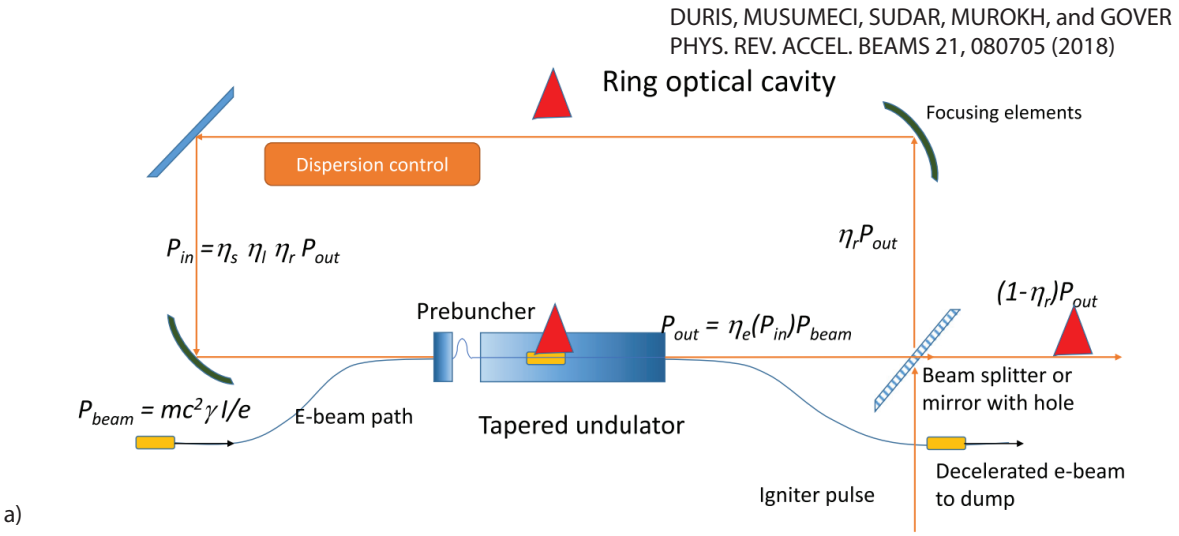

a)

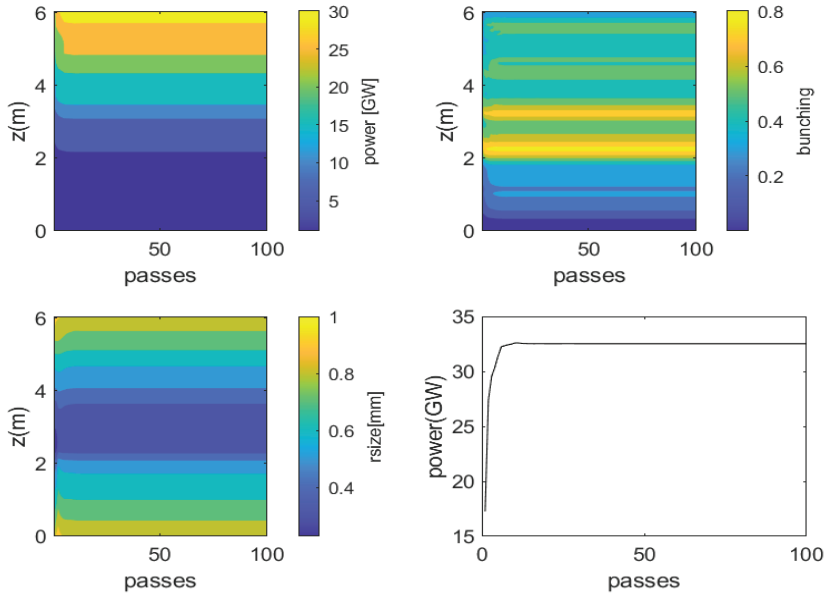

b)

Figure 2.45: a) A schematic layout of the TESSO experiment. Optical elements are used to recirculate a portion of the undulator radiation to use as a seed for the next pass. b) A simulation output of TESSO at 257.5 nm with transmission of 10% and focusing element of 4 m.

entrance. After the first ten passes, the output power is stabilized at 32 GW. If the seed laser had a pulse length of 180 μm and e-beam were at a repetition rate of 1 MHz, the system would have an average power of 17 kW.

Currently, because of the changes in the plans at APS, an experimental verification of the high gain TESSA regime is to be held at Fermilab Accelerator Science and Technology (FAST) at a lower energy and a longer wavelength (150 MeV and 515 nm). The superconducting accelerator in the FAST beamline enables 3-9 MHz repetition rate, allowing a very high average beam power. In the case of the FAST beamline at a longer wavelength, a peak power of 12 GW is possible at a peak current of 600 A, based on an optimization process discussed earlier. When placed in an oscillator setup, the system requires more portion of the undulator radiation for the seed, because the output peak power is lower. The seed laser should be greater than 1 GW in order to modulate the beam for prebunching. When 30 % of radiation is sent back as a seed, passing through a lens of 4.2 meters focal length, the output power stabilizes after ten passes. For a repetition rate of 5 MHz and radiation pulse length of 180 μm, an average power of 30 kW would be possible.

In order to obtain the maximum possible average power, the transmission and optical system should be optimized more thoroughly. In addition, the time-dependent simulation of a realistic input beam should be considered in order to fully assess the system efficiency.

The cavity requires a long optical distance to synchronize with a repetition rate of 1-5 MHz. The travel distance should be 300 meters at 1 MHz and 60 meters at 5 MHz.

An experimental demonstration of the TESSO system will pave the way to the short wavelength, high efficiency, high average power radiation source. A high average power and short wavelength radiation source will increase the productivity of EUV lithography. A high average power radiation source is also beneficial in the research areas of beam-based space propulsion, nuclear power plants, and plasma ignition.

CHAPTER 3

The TESSAtron experiment and future goals

The final chapter of this document discusses a recent experiment conducted at UCLA using the undulator made for the TESSA experiment. While the LEA-TESSA experiment was postponed due to the COVID situation compounded with the national laboratory schedule, the experiment held at UCLA demonstrated a high efficiency, high power FEL-based THz radiation source, verifying a zero slippage interaction and also testing the new undulator built by Radiabeam/UCLA for the TESSA experiment. This chapter first discusses the motivation for a THz experiment and introduces the concept behind the zero slippage interaction and the reasoning behind the parameter choices. Then, the experimental setup and results are discussed, followed by more details about the simulation and the experimental protocols.

The frequency range of 0.1 THz and 30 THz is called the THz gap because of the scarcity of usual radiation sources in the range. Diode lasers have a wide coverage of high frequencies from mid-infrared to UV (3 μm to 200 nm) [114], and microwave and radiowave sources can cover the lower frequencies (1 cm to 1 m), but efficient radiation sources in between the two ranges are less available.

Because the THz waves are transparent to some materials that are opaque in the visible waves, THz imaging has been used for medical and security imaging. The THz range has also been of great interest for molecular spectroscopy of chemical species that have strong absorption lines in the THz.

Researchers in the past decades have developed THz radiation sources based on variety of methods. Electronic solid state lasers, quantum cascade lasers, and laser driven THz

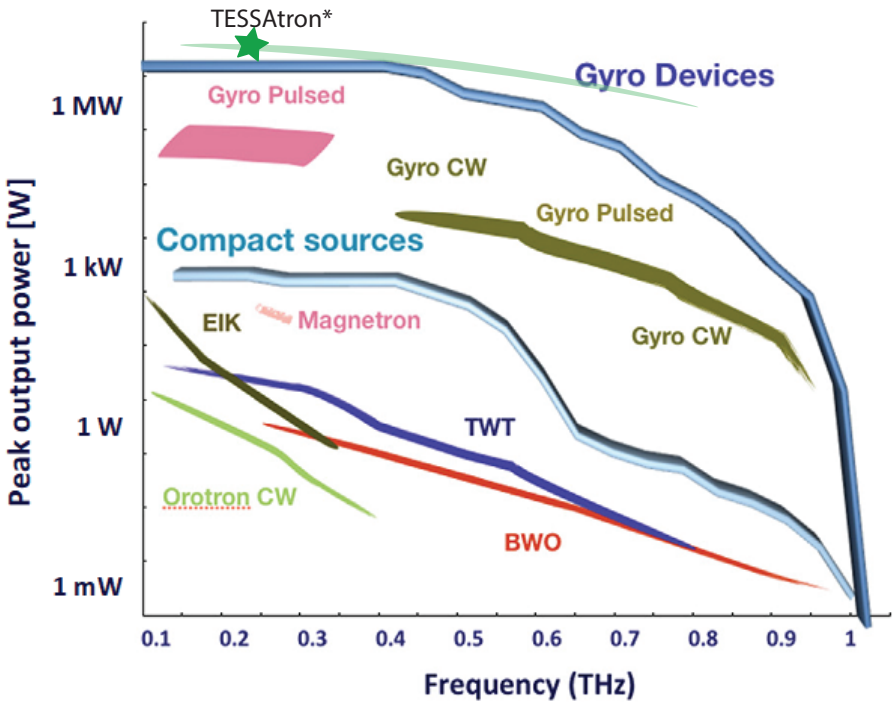

Figure 3.1: Average power of vacuum, electron THz devices available [24] plotted with the experimental result of the TESSAtron experiment (star) and expected spectrum (green).

emitters are some examples of compact THz sources that have become basis for modern imaging technologies.

Traditional vacuum based compact radiation sources such as klystrons or magnetrons usually provide higher power, but they become less efficient at higher frequencies above 300 GHz [24] (Figure 3.1). Recent advancements of gyrotrons have provided higher power radiation sources in the THz range. A gyrotron is another beam-based THz source based on high field magnets that has been researched since the 1950's, in which electron beams are emitted from a cathode and gyrate in an magnetic field [64]. In the kilowatt range gyrotrons are used for electron spin resonance spectroscopy [75] and distant detection of radiaoactive sources[64].

Higher power, megawatts-class THz sources have been used in energy and space sciences. Repetitive pulses from a THz source of 1 MW, 170 GHz gyrotron were used for plasma ignited propulsion, which generated up to 300 N/MW for propulsion [80]. Megawatt-level, nearly continuous millimeter sources are used for nuclear power plants and for plasma ignition and heating [110, 111]. Developing THz radiation sources with more peak power and more average power is important for progress in the energy research. The International thermonuclear experimental reactor project (ITER) would require eleven 170 GHz gyrotrons that provide 1 MW of continuous power. Future fusion power plants demand even higher power [68]; for example, DEMO, a conceptual fusion power plant, demands a 50 MW source with 60% efficiency [49].

FEL-based THz sources have also been researched over decades. UCSB FEL has provided kW power THz sources (2.5 mm to 340 mum) to users since 1998 [91]. JLab has achieved an average power of 20 W and peak power of 1 MW at around 0.5 THz[16]. NovoFEL has an average power of 400 W and peak power of 0.6kW [63]. Osaka FEL measured 29 mJ of 4μm FWHM at 65 μm, with 260μJ micropulse energy [58].

Both gyrotrons and FELs operate in vacuum and generate radiation due to the curved trajectory of electrons. While the magnetic field of an undulator is periodic due to the external periodic array of magnets, the magnetic field of a gyrotron is uniform axial field caused by the coils surrounding the tube. of electrons guided by external magnetic field. The researchers increase the efficiency of the gyrotrons by tapering the field [27], matching the dispersion relation of the waveguide [61], as well as improving the e-beam bunching [103], similar to how the researchers improve the FEL FEL efficiency. Due to the similarities in the two systems, improving one system can provide interesting insights for the other in a constructive manner.

Gyrotrons are usually compactly made devices for commercial purposes while the FELs are large laboratory sized system. Meanwhile, FELs can also be designed in a compact manner.

The recent THz experiment conducted at the PEGASUS Laboratory at UCLA utilizes already installed S-band photoinjector and an 11-cell S-band linear accelerator, with beam energy of γ=10-18 and bunch charge of 1-500 pC (Figure 3.1) [41].

The demonstration of high efficiency and high peak power due to the zero slippage interaction, as well as testing the recently built helical undulator will serve as an important step in the development of a high average power FEL based radiation source.

3.0.1 The zero slippage condition

The zero slippage interaction refers to matching the phase and the group velocity of the radiation with the electron beam velocity. By matching the dispersion relation of the waveguide and the electron beam, it is possible to satisfy the resonance condition with a large bandwidth of frequencies and support interaction with short electron bunches.

The longitudinal velocity of electrons can be written as

$$\beta_z = \sqrt{1 - \frac{1 + K^2}{\gamma^2}} \tag{3.1}$$

as shown in Chapter 1. By the FEL resonance condition, the gradient of the ponderomotive phase must stay constant

$$\frac{\partial \theta}{\partial z} = (k_w + k_s) - \omega \frac{\partial t}{\partial z} \approx (k_w + k_s) - \frac{\omega}{v_z} = 0, \tag{3.2}$$

so the resonant frequency can be written as

$$\omega = c\beta_z(k_u + k_s). \tag{3.3}$$

The magnitude of a wave vector is a summation in quadrature of the longitudinal wave vector and the the transverse wave vector

$$k_0^2 = \frac{\omega^2}{c^2} = k_s^2 + k_\perp^2 \tag{3.4}$$

in which the transverse wave vector of a TE11 circular waveguide mode is

$$k_\perp = \frac{1.8412}{R} \tag{3.5}$$

where R is the radius of the waveguide, and the longitudinal wave vector is dominated by the laser field. The longitudinal wave vector can be substituted to find the solution for the zero slippage condition. Defining $\gamma_z^2 = \frac{1}{1-\beta_z^2} = \frac{\gamma^2}{1+K^2}$, the resonant wave vector can be derived as

$$\omega = c\gamma_z^2\beta_z\left(k_u \pm \sqrt{k_u^2 - \frac{k_\perp^2 + k_u^2}{\gamma_z^2}}\right). \tag{3.6}$$

Depending on the electron beam energy, the quadratic solution would have a single tangential solution between the waveguide dispersion and the electron beam resonant energy:

$$\begin{aligned} k_u &= \frac{1}{\gamma_{z,zs}}\sqrt{k_u^2 + k_\perp^2} \\ \omega_{zs} &= c\gamma_{z,zs}^2\beta_{z,zs}k_u \end{aligned} \tag{3.7}$$

The resonant energy and the frequency at the zero slippage condition based on the above relation is:

$$\begin{aligned} \gamma_{z,zs}^2 &= 1 + \frac{k_\perp^2}{k_u^2} \\ \omega_{zs} &= ck_\perp\sqrt{1 + \frac{k_\perp^2}{k_u^2}} \end{aligned} \tag{3.8}$$

which also relates the zero-slippage resonant energy and frequency as

$$\omega_{zs} = ck_\perp\gamma_{z,zs}. \tag{3.9}$$

Therefore, the radiation frequency can be written in terms of the beam energy and the resonant energy as

$$\omega = \frac{ck_u\gamma^2}{1+K^2}\sqrt{1 - \frac{1+K^2}{\gamma^2}}\left(1 \pm \sqrt{1 - \frac{\gamma_{zs}^2}{\gamma^2}}\right). \tag{3.10}$$

When there are two solutions to the frequency, at the higher frequency the radiation group velocity is larger than the electron velocity, and at the lower frequency the radiation

group velocity is smaller than the electron velocity. The wave packet therefore has a fast high frequency slipping ahead of the electron bunch, and a lower frequency trailing behind. When the system is at the zero slippage condition, the wave packet travels at $v_g = c\beta_z$.

As shown in Figure 3.2a, the waveguide and the electron beam dispersion relation cross tangentially at the single solution, allowing a broader spectral bandwidth of resonant frequency in the neighborhood (the red fill in Figure 3.2a). Not only that, there are two solutions when the energy is above the resonant energy (the cyan stars in Figure 3.2a). As a result, the system is less susceptible to deviate from the resonance condition. In comparison, the dispersion relation of the laser wave in free space is $\omega = ck_s$ which is a straight line, and consequently there is only one solution for the resonance condition (the red hexagon in Figure 3.2a). When the energy is lower, there would be no crossing between the dispersion relation of the waveguide and the electron beam.

Given the fixed undulator period (32 mm) of Theseus, the frequency is dominated by the radius of the waveguide. Figure 3.2b shows the relation of the frequency and the pipe radius. The resonant frequency increases with a smaller waveguide. Meanwhile, with a smaller pipe radius, the system needs a higher energy, given the same undulator field, to meet the resonance condition. However, as the waveguide becomes smaller it is more difficult to pass the electron beam through the pipe.

An electron beam in a helical undulator travels in a helical trajectory as illustrated in Figure 3.3. The transmission of an electron beam travelling in a helix through a thin pipe depends on the helix radius and the pipe radius. A helically travelling beam with a larger helix radius has more difficulty to pass through a small pipe as the pipe can sag mid-way through the meter-long undulator, and the beam will also go through the betatron oscillation. The helical trajectory in an undulator has a radius of

$$r = \frac{K}{\gamma k_u \beta_z} \tag{3.11}$$

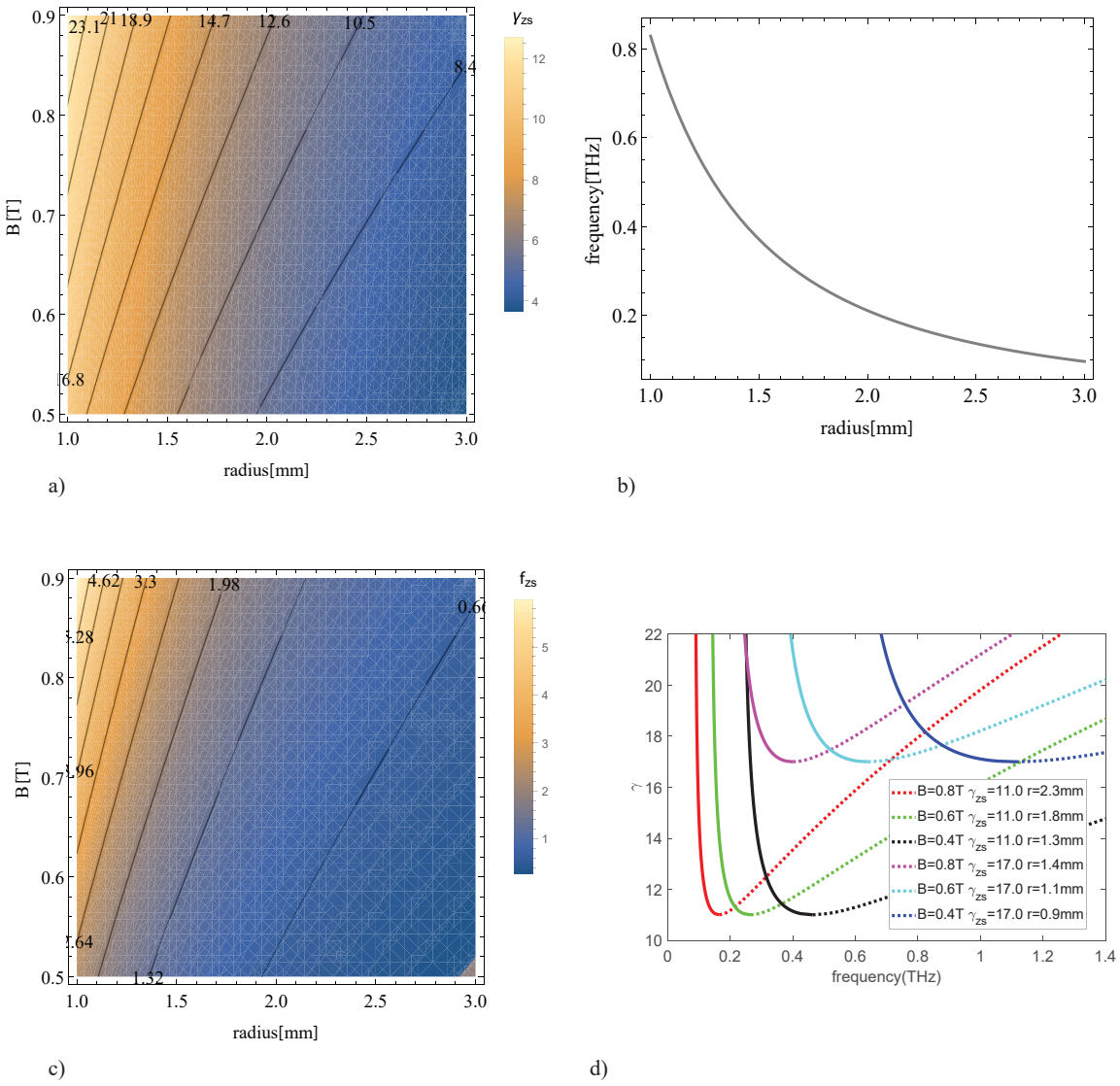

Figure 3.2: Zero slippage condition. a) Zero slippage resonant energy compared with the waveguide pipe radius and undulator on-axis field, given a fixed undulator period of 32 mm. b) Zero slippage resonant frequency at different waveguide radii and a fixed undulator period of 32 mm. c) Zero-slippage resonant frequency compared with the waveguide pipe radius and the undulator on-axis field. d) electron beam energy and radiation frequency relation at different undulator fields B, pipe radii r, and corresponding resonant zero-slippage energy γ_{zs} according to Equation 3.10

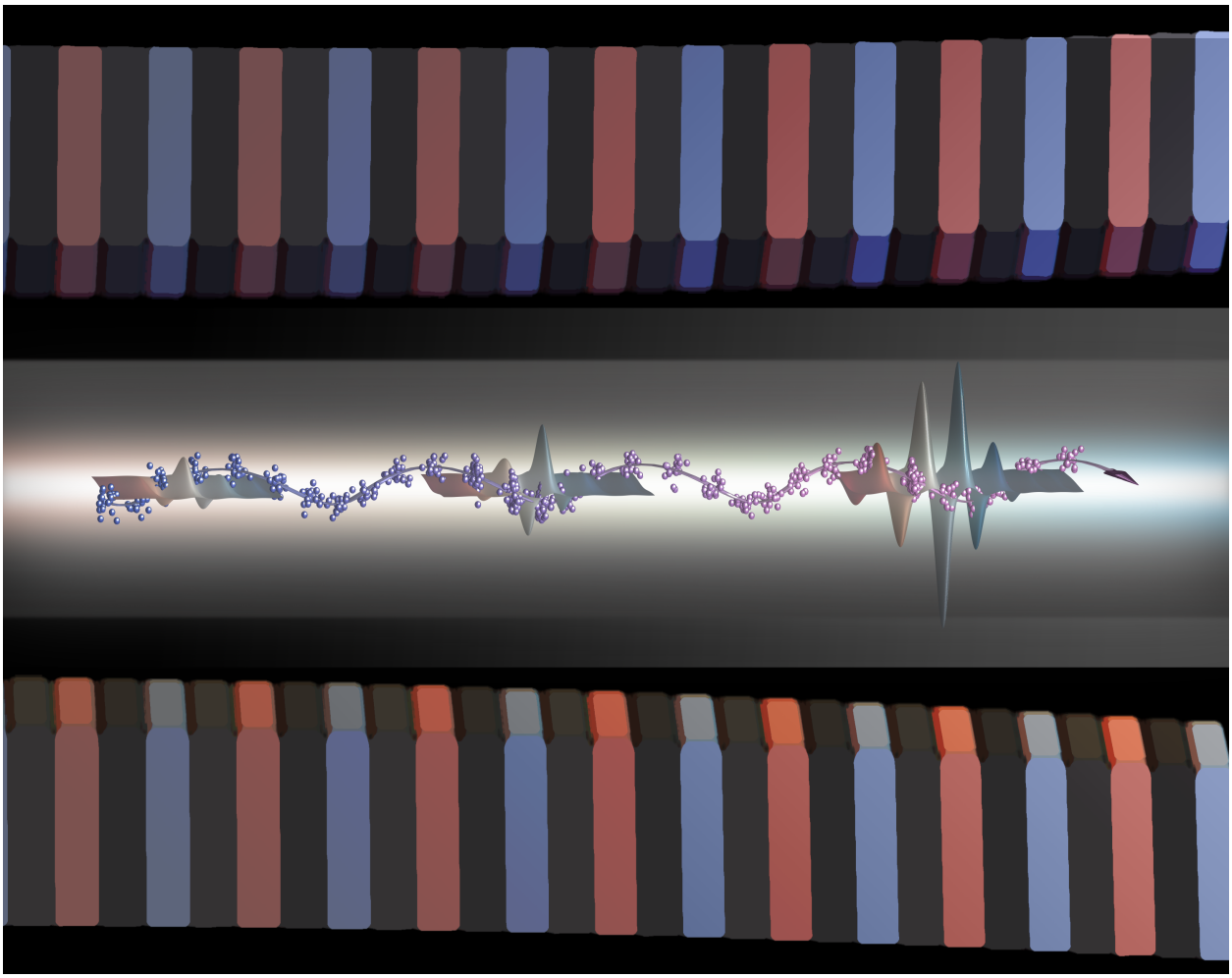

Figure 3.3: An illustration of bunched electrons travelling in a tapered undulator. As the electrons decelerate (indicated by the color of blue→ red), radiation is amplified (red → blue). The waves indicate the increase in the electric field, in which the phase is shifted from the red → blue wavelength, which is also shown in Figure 3.8 at different beam energies.

which can be written as

$$r^2 = \frac{K^2}{k_u^2 \gamma^2}\left(1 - \frac{1+K^2}{\gamma^2}\right)^{-1}. \tag{3.12}$$

Assuming the transmission is related to $T = (b^2 - r^2)/b^2$ where b is the pipe radius and r is the helix radius, the transmission at different undulator fields and e-beam energies can be compared. Figure 3.4a shows an expected transmission of an electron beam through a pipe at different electron beam energies and undulator magnetic fields. At a smaller beam energy and higher field, the transmission becomes more difficult than at a higher beam energy and a smaller field.

The ratio in Figure 3.4b shows that a higher energy would be preferable in order to pass the beam through a pipe. However, to meet the zero slippage condition, the radius of the pipe needs to be smaller at a higher e-beam energy given a similar range of undulator field. If the radius of the pipe were smaller, the transmission would be more difficult.

Meanwhile, when the electrons travel at the zero-slippage resonant condition in the waveguide, the trajectory radius depends on the waveguide radius, so the ratio of the trajectory radius and the waveguide radius is dominated only by the undulator vector potential

$$\frac{r^2}{b^2} = \frac{K^2}{1+K^2}\frac{1}{1.841^2}. \tag{3.13}$$

Figure 3.4b shows a ratio of the electron beam trajectory radius and the pipe radius when the electron beam energy is at the zero slippage condition. When the beam is at resonance, there would be an increased transmission difficulty at a larger on-axis field. It is interesting that this factor does not vary with the waveguide radius. If the waveguide pipe were smaller, the trajectory radius would also be reduced, resulting in a similar likelihood of transmission. This analysis is for a point-like electron beam, but in reality, the beam has a transverse dimension.

The transverse matched beam size at equilibrium is $\sigma_x = \sqrt{\frac{\epsilon_n \lambda_u}{2K}}$ where ϵ_n is the normalized emittance. Assuming that the electrons would be offset from the helical trajectory by

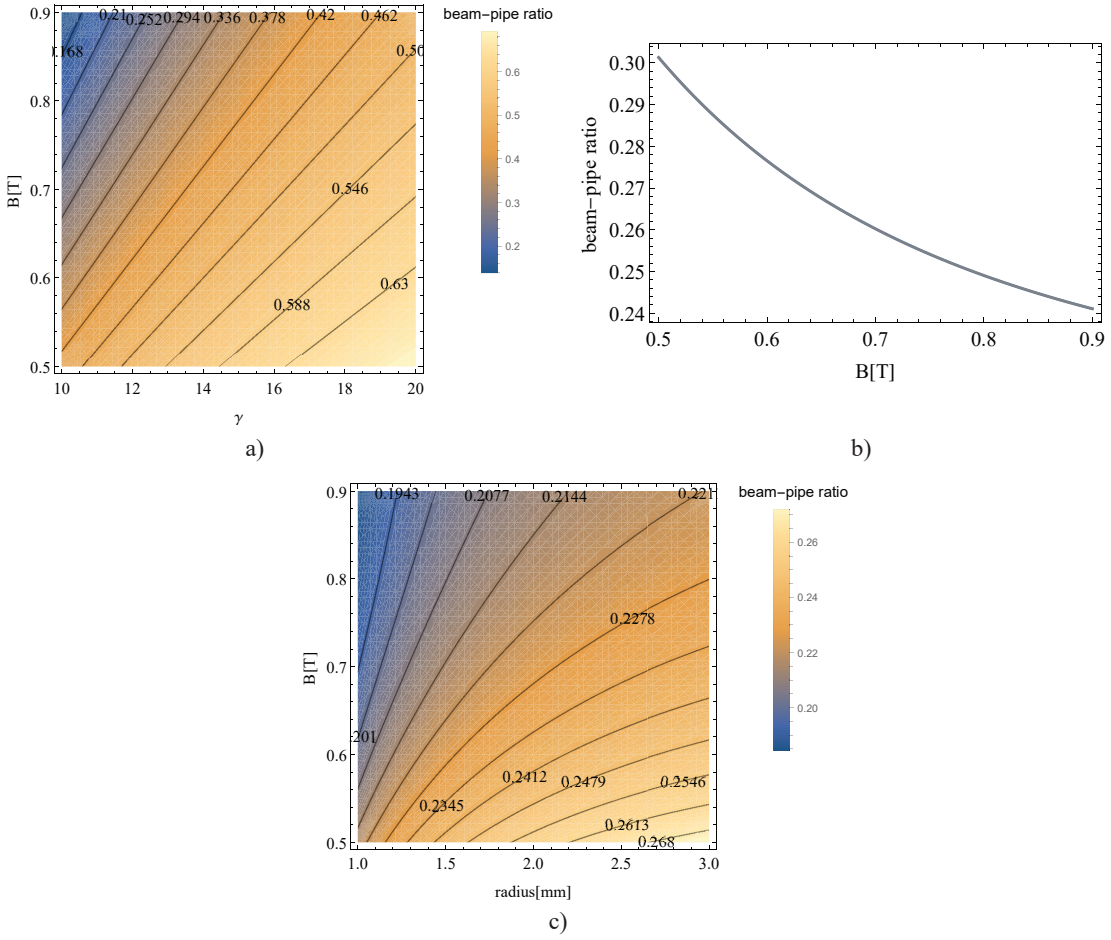

Figure 3.4: a) Ratio $T = (b^2 - r^2)/b^2$ of electron beam size r and pipe radius b at different beam energies and undulator fields. b) Ratio T at the zero slippage condition. c) Beam offset taking into account additional effects caused by the transverse beam size.

the amount of the equilibrium beam size, while their beam energy meets the zero slippage condition depending on the pipe radius and the undulator field, it is possible to show the ratio of the beam offset and the pipe size at different pipe radii and undulator fields (Figure 3.4c). The transmission is more difficult at a larger undulator field and a smaller pipe radius based on the trajectory offset and the beam size.

3.0.2 Pegasus-Tessatron Experimental Setup

The zero slippage experiment was held at the UCLA Pegasus photoinjector laboratory. The laboratory consists of a beamline room (bunker) that is radiation-shielded with an interlocked door system, a control room where the magnets (solenoid, quadrupoles, steering, etc) are connected to the control computers via cables running through a hole in the wall, a space for the RF modulator and klystron, and a laser room that houses the driver lasers (Figure 3.6).

The drive laser for the photocathode was the Titanium-Saphhire laser system from Coherent. Frequency-tripled to 266 nm, this laser provides pulses of 100 μJ energy with rms spot size around 0.9 mm and FWHM pulse length 100 fs. The laser is converted to UV in the laser room and is transported to the beamline room through the pipe. From the second crystal to the pipe is 316 mm, the pipe is 151 mm, there is an iris at about 73 mm from the wall, a lens at 469 mm from the wall, and the photocathode is around 88 mm from the lens. The laser intensity can be measured from a virtual cathode installed in the beamline room. A beam splitter is placed at a position equidistant to the photocathode and to the camera screen, sending around 1% of the laser to the camera screen.

The master oscillator from a digital board or an analog system sends 2.856 GHz optical trains. The RF signal is amplified by the pre-amplifier to 30 dBm. The splitter, which attenuates the signal by around 4 dBm, sends a half of the signal to the laser room and the other half to the RF-Box. The RF Box has a phase shifter and an amplifier, which increases the signal to 30 dBm. The RF signal is sent to the kilowatt amplifer, which sends the signals

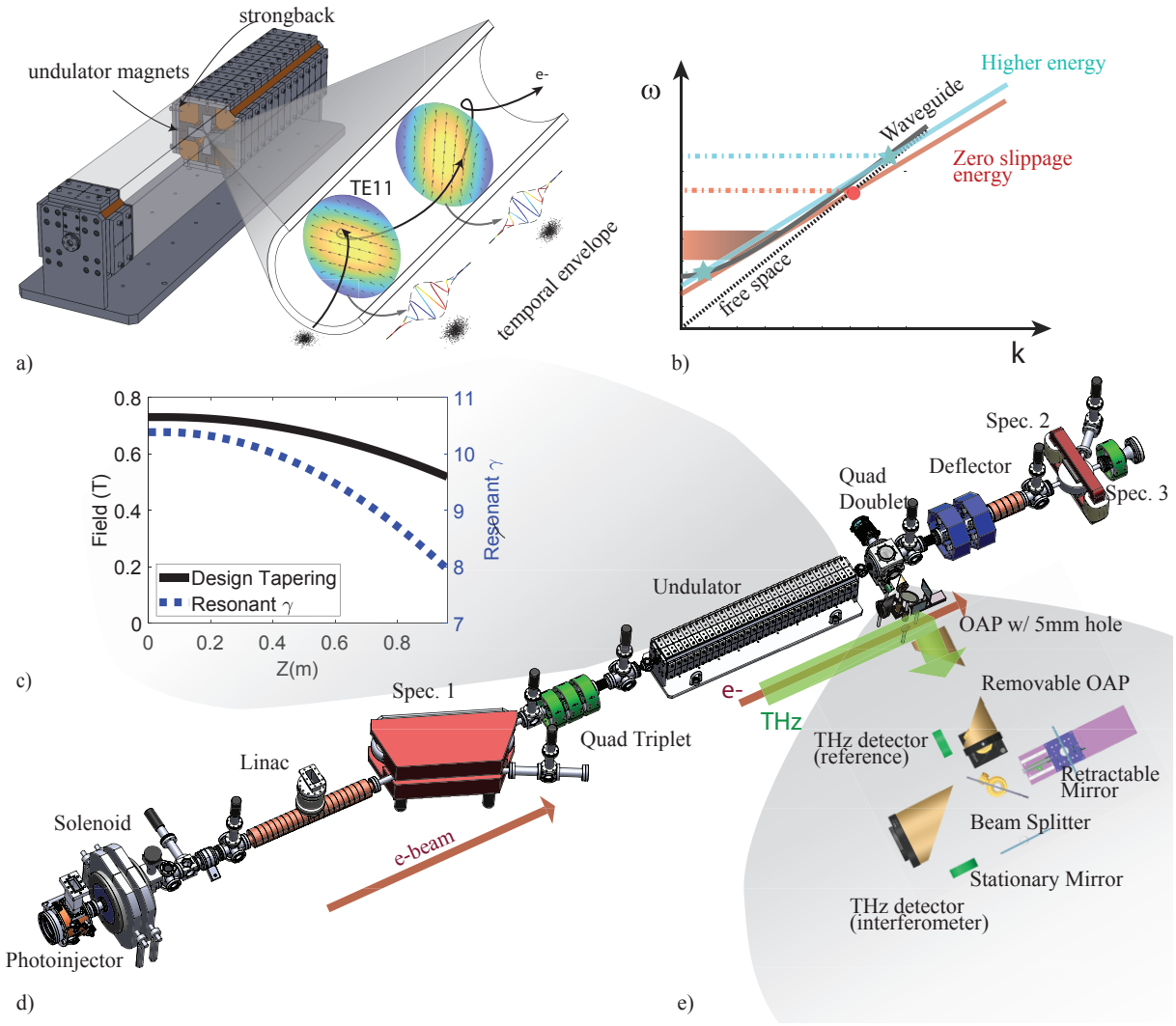

Figure 3.5: Tapering-enhanced zero slippage THz FEL scheme. a) Cartoon of the zero slippage FEL interaction between relativistic electrons and the TE11 mode of a circular waveguide in a helical undulator. b) Dispersion diagram for a waveguide FEL. Resonant phase matching occurs when the phase velocity of the electrons in the undulator (red line) intersects the radiation dispersion curves (black solid for waveguide, dotted for free space). When the two curves have a tangent intersection, the interaction bandwidth is significantly increased. c) Undulator magnetic field amplitude and resonant energy tapering along the undulator. d) Pegasus beamline technical drawing showing the photoinjector, the buncher linac, the undulator, and the e-beam diagnostics. e) The inset shows more details on the THz diagnostics setup for pulse energy and interferometry measurements.

to the klystron. The klystron sends around 10 MW electromagnetic power to the gun and the linac through the waveguide filled by SF6. Meanwhile, the other side of the low-level RF at 0.2 W is sent to the Synchronization and Delay Generator (SDG, synchrolock) in the laser room. The Evolution laser, which produces optical pulses at 1 kHz sends some of the pulses to the pulse generator in the laser room. The digital delay / pulse generator (Stanford DG-535) controls the laser frequency to be at 60 Hz or 960 Hz.

The pulse generator triggers the SDG which synchronizes the RF signals and the laser pulses. The SDG synchronizes the pulses based on the low-level RF signal which is at 79.33 MHz (converted from the 2.856 GHz pulses sent from the master oscillator) and the laser pulses at 960 Hz. The SDG adjusts the pockels cells that sets the laser timing. The two pockels cells, which control the optical pathway by their voltages, trap the laser pulses in a resonator and release the amplified pulse at a timing synchronized with the RF signal. The output laser is converted to 266 nm, enters the beamline room through the 151 mm long pipe, and arrives the photocathode by an injection mirror.

Meanwhile, the SDG also sends the pulses to the pulse generator in the control room (DG-645), which uses the pulses as a reference to trigger the modulator at every 0.6 s. The modulator provides the high voltage for the klystron which powers the photoinjector and the linac, so the signal from DG-645 is the dominant trigger that controls the electron beam generation. With the laser on the photocathode and amplified RF power in phase, an electron beam is generated at every 0.6 s.

The main components in the beamline are an S-band RF gun, a solenoid, a booster linac, a spectrometer dipole a set of three quadrupoles, a deflecting cavity, and a second spectrometer dipole. The S-band RF gun has a copper photocathode and can generate up to 200 pC electron beams with energy of $\gamma = 7$. The booster linac is an 11 cell S-band linac, with peak gradient of 20 MV/m that accelerates the beam energy up to $\gamma = 18$. The energy of the beam can be adjusted by the linac phase which also changes the energy spread, and also by the linac temperature which takes longer but reduces the energy spread. The linac

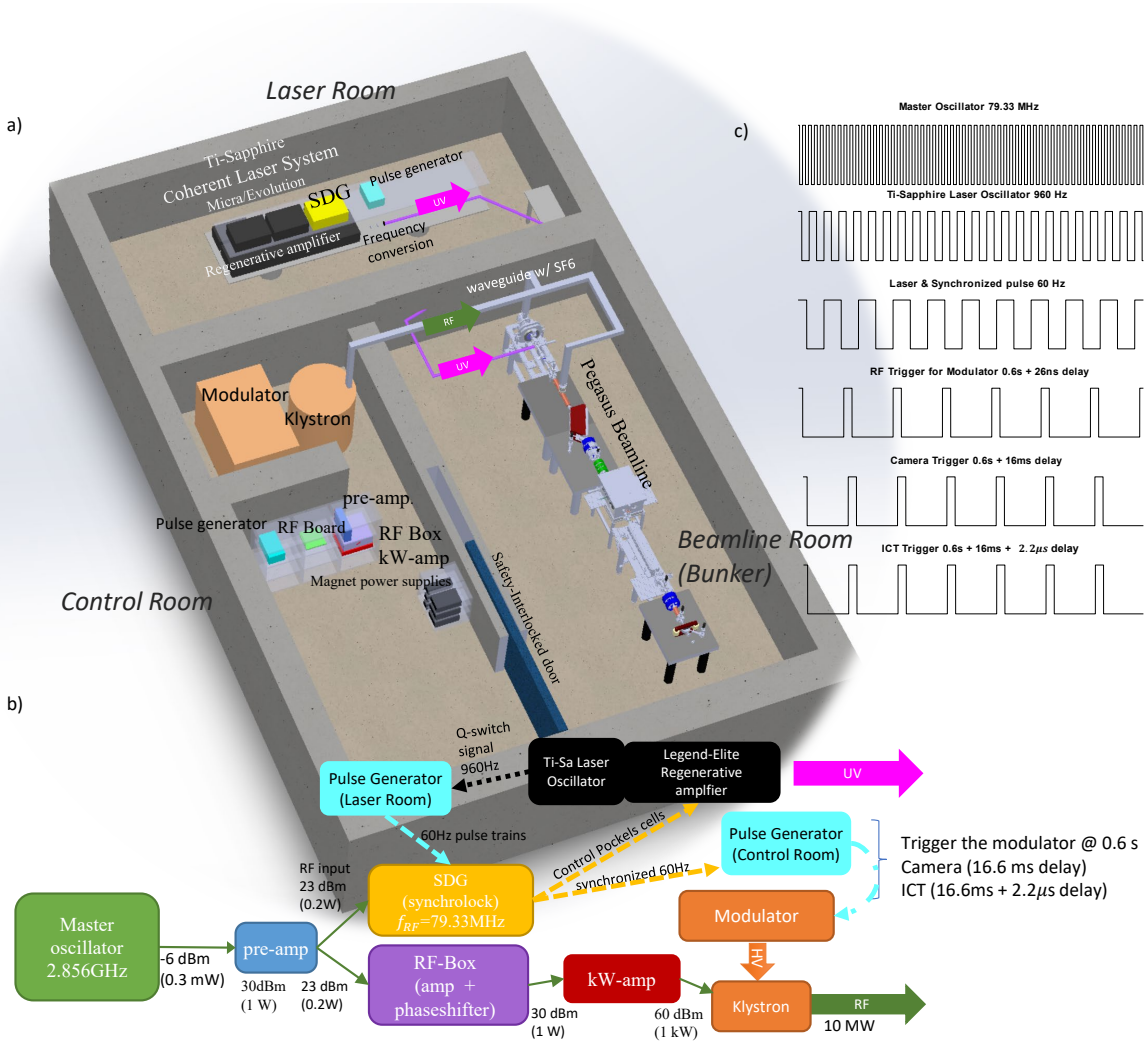

Figure 3.6: a) An illustration of the Pegasus Laboratory (not drawn to scale). b) The RF power source for the accelerating cavities and the trigger connections. c) An illustration of the trigger pulse trains.

phase should be tuned 50 to 75 degrees off-crest in order to compress the beam by velocity bunching.

The magnets in the beamline are connected to the power supplies in the control room, and the power supplies are connected to one of the control computers. By opening the serial port using a virtual serial port software, the port can be accessed by other computers in the laboratory. The magnets are controlled by a main control script written in Labview. The main Pegasus control can be used to manipulate the magnets and the screens. The settings for the magnets and the screens are saved in the PostgreSQL database. The control also reads the data from the camera and saves the image analysis data. The main control also checks for changes in a machine-control table and adjusts the magnetic setting. By changing the data in the machine-control table, a user can manipulate the magnets using other scripts, externally from the Labview control.

The charge is measured by a Turbo Integrating Current Transformer (ICT) located at 1 m from the cathode. Electron beam transport can be monitored before the linac (YAG2), after the linac (YAG4), and after the quadrupole-triplet (PIMAX3). YAG2 is the first screen in the beamline that visualizes electron beams emitted from the cathode, and the solenoid scan data at this screen is very useful for calibration and QE measurements. YAG4 is the first screen after the linac and the first spectrometer, and the screen is used to monitor the beam transport after the linac and the dipole. There are three quadrupoles used for this experiment. Electron beam size is optimized by a quad scan script written in Matlab. The quad scan finds an analytic solution for a set of quadrupoles that will make a round beam at an approximate location of the screen, sends signals to the Labview control to change the quadrupole setting in the lab, and records beam size measurements from each set of quadrupoles based on the data from the PIMAX control. Based on the set of data measured at different quadrupole settings, the script can analyze the emittance, charge, and energy of the beam. The script also calculates the initial beam matrix at screen 4, and a user can adjust the beam to focus at a location further than the PIMAX screen. The ICT and the

camera are triggered by the pulse generator in the control room.

Electron beam energy spectrum is measured before the undulator using Spec. 1, which has radius of curvature 0.67 m and bending angle of 45 degrees. Spec. 2 and Spec. 3 are installed after the undulator to monitor the beam deceleration. Spec. 2 is a round pole dipole that bends the beam by 45 degrees with radius of curvature 0.093 m. The spectrometer screen is located 0.15 m downstream of the dipole and the dispersion at the screen is 0.13 m. The camera calibration is 41 μm per pixel, and each pixel corresponds to 3e-4 relative energy variation. The 12 mm opening of the vacuum pipe at the spectrometer exit limits measurement to ± 9 %. The interaction at zero slippage condition can decelerate more than 20%, so the full energy spectra can only be obtained by stitching images recorded at different dipole currents. An additional spectrometer (Spec. 3) using a short rectangular dipole providing very small dispersion is used on the straight-thru beamline for independent confirmation of the average beam energy loss, validating the stitching approach. A 9.6 GHz deflector with a maximum voltage of 500 kV is used to streak the beam vertically to record the longitudinal phase space image.

The electron beam from the undulator passes through a 4.7 mm diameter short extension pipe used to collect the radiation at the exit of the undulator, and the radiation couples to free space. An off-axis parabolic mirror (OAP) with a 5 mm diameter hole (2" diameter, gold plated, focal length 3") installed in a vacuum cube (4.5" long) reflects the THz radiation, while the electrons that pass through the OAP are measured in the longitudinal phase space diagnostics section. The THz radiation reflected by 90 degrees from the OAP leaves the vacuum system through a z-cut quartz THz window. The total energy in the radiation pulse is measured by placing a removable 50 mm diameter OAP, which focuses the radiation onto a 8 mm diameter pyroelectroic Gentec THz detector. The detector is factory-calibrated at 1 mm wavelength to 7 nJ/mV.

The transmission of the THz transport system from the undulator to the detector is measured by using a 10 mW CW 140 GHz radiation source placed at the entrance of the

undulator. The radiation collected at the detector is 27 % of the radiation at the undulator exit. The main reasons for the poor transmission are losses on the collecting pipe, the OAP size, the in-vacuum apertures, and the vacuum window. Radiation diffracts rapidly after the undulator, so a larger diagnostics setup (a larger OAP and larger vacuum components) would have helped. However, the size of the assembly was limited by the available space in the laboratory.

Upon removing this OAP, the THz radiation entered a Michelson interferometer system. A wire-grid beamsplitter separates the radiation along two paths. One path directs the radiation to a stationary mirror, and the other directs the radiation to a movable mirror mounted on a linear stage. The two lights merge at the beam splitter due to the difference in polarization and are directed by an OAP to another 8 mm diameter pyroelectroic Gentec THz detector. The interferogram is obtained by moving the linear stage through 50 mm. The signal on the interferometer is less than 10% of the reference signal due to the large absorption of the beam splitter (30% transmission) and additional diffraction caused by the small aperture of the THz window. While a larger cube with a larger aperture and a larger optical setup could improve the signal strength, the system is sufficient to detect the interferogram and measure the wavelength of the THz signal.

The Theseus undulator is tapered from 0.73 T to 0.52 T. The vacuum pipe has an outer diameter of 5.56 mm and inner diameter of 4.54 mm. The undulator is aligned by a green laser injected after the photoinjector. The undulator supports allow for fine adjustment of position and angle. There are two small cubes (1.33") with pipe mounts in order to use a smaller pipe, but experiments with smaller pipes have not been performed due to the experimental schedule and the difficulty of straightening the pipe. The mounts are on a 3-axis stage which allowed finer adjustment of the vacuum path.

3.0.3 Experimental Results and Data Analysis

Upon sending the electron beam through the undulator, the beam is steered through the deflector and is imaged on PIMAX. The deceleration of the beam is clear when the beam has a long tail. The decelerated beam shows denser energy collected at several points, indicating electron (Figure 3.7a).

The FEL interaction is established by recording the energy profiles of the beam from the high resolution magnetic spectrometer as well as the THz radiation energy measured by the reference pyrodetector as a function of the input beam charge. In the contour plot in Figure 3.7a, the energy spectra are normalized to better highlight the evolution of the energy distribution as the THz FEL interaction grows in strength. For charges above 50 pC, in conjunction with the appearance of a clear signal on the pyro-detector as shown in Figure 3.7b, the e-beam spectrum broadens and red-shifts to a lower mean energy. The spectra also develop large and deep modulations, which are characteristic signatures of the FEL longitudinal phase space dynamics occuring in the tapered undulator[107]. At the highest injected beam charge (220 pC), the average beam energy decreases by 10%, with some particles losing more than 20 % of their initial kinetic energy. Taking into account the THz pyroelectric detector calibration (145 kV/J) and the losses in the THz transport line mostly due to apertures and diffraction (73%), the maximum signal recorded on the detector yields an estimated THz energy at the undulator exit of 50 μJ. The amount matches the average energy loss by the electron beam, assuming the stainless steel waveguide losses and that only 40 % of the injected charge is transmitted through the undulator.

The THz signal and the associated electron spectra are well correlated with the injected charge through the undulator (Figure 3.7b), with output fluctuations less than 10% for a given input charge, mostly attributable to energy and pointing fluctuations. The overall stability is remarkable for single pass FEL in the absence of an external radiation seed signal, and is explained by the initial bunching from the compressed electron beam which effectively

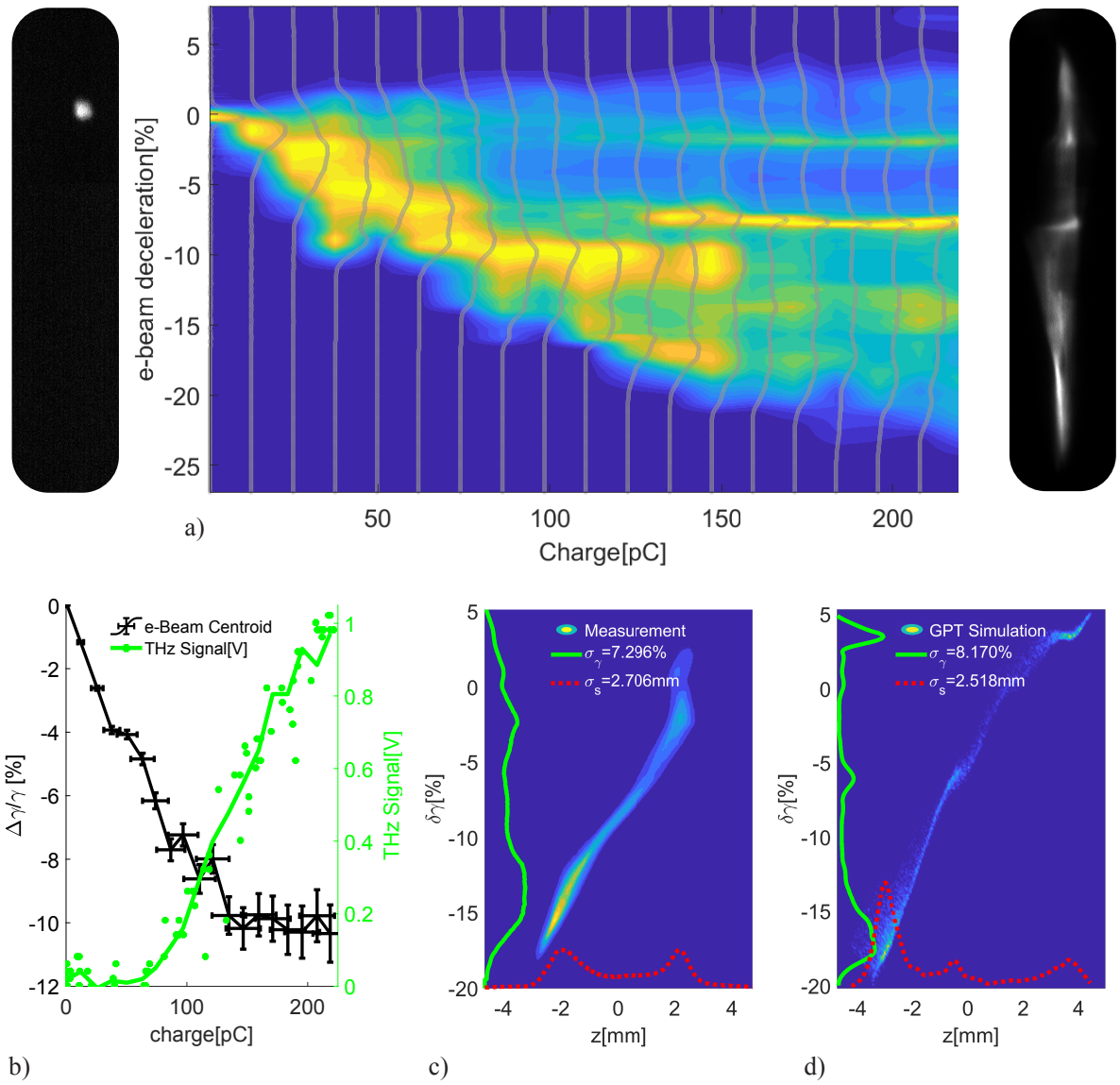

Figure 3.7: a) High resolution electron beam spectra as a function of the charge injected into the undulator. Two reference raw spectrometer images for the lowest (left) and highest (right) charge are also shown b) Relative beam energy centroid variation and THz pulse energy from the reference pyro detector corresponding to a). The horizontal errors correspond to the width of the charge bins. The vertical errors on the centroid data represent the rms of the distribution calculated over 10 images. Measured (c) and simulated (d) longitudinal phase spaces for 150 pC injected beam charge. For this comparison, the longitudinal phase space at the exit of the undulator is propagated up to the deflector plane located 6.5 m from the cathode.

works as an FEL seeding signal.

The x-band deflector located after the undulator can be used to streak the beam vertically and visualize the longitudinal phase space on the spectrometer screen. A sample phase space corresponding to 150 pC injected charge is shown in Figure 3.7d. While the resolution of the longitudinal phase space measurement is blurred from the large transverse size of the beam in the deflector and relatively large emittance of the beam after the undulator, the most salient features in the beam distribution such as chirp, energy spread, and bunch length are well reproduced in the measured image.

The resonant nature of the interaction is studied by adjusting the linac phase to vary the initial beam energy and measuring the spectral content using a Michelson interferometer (Figure 3.5e). Two sample autocorrelation traces and the associated Fourier transforms are displayed for beam energies near (blue) and above (orange) the expected zero-slippage resonant value. Clear differences in period and radiation pulse length can be observed.

A more complete scan of the peak frequency and spectral bandwidth is reported in Figure 3.9c,d. The decrease of the peak frequency with with the increased energy agrees with the analytic relation (Equation 3.10) shown as a black solid curve and also with the GPT simulation results, which are the contour colors in which the the yellower represent the higher efficiency. The THz energy measured at each e-beam energy is plotted vertically (solid red line), and the e-beam deceleration is also plotted vertically (blue error bars). Expected e-beam deceleration in the GPT simulation is plotted in solid orange.

In the plotted simulation, the PEGASUS beamline with a photoinjector, a solenoid, a linear accelerator, and a triplet of quadrupoles is simulated in GPT. Then, the distribution is used to compute the FEL interaction using the GPT FEL module developed by UCLA [40], in which the FEL interaction of electron beams in an undulator is calculated using a frequency and modal expansion of the electromagnetic field.

Both the simulation and the experimental results agree with the low frequency branch

of the analytic curve. Because the bunch length is much smaller than the resonant wavelength, the electrons appear more bunched as the radiation wavelength becomes longer. Consequently, the amplification is much stronger at the longer resonant wavelength.

Figure 3.8 visualizes the FEL radiation waveforms at different energies according to the GPT simulation. In this simulation, the Theseus undulator with the field tapered from 0.73 T to 0.52 T and the period of 32 mm and a Gaussian input distribution of charge 150 pC, transverse emittance 2 mm-mrad, and beam sizes σ_x=σ_z=0.3 mm are used. When the electron beam energy is the zero-slippage resonant energy (γ=10.4), the waveform has one dominant frequency. As the beam energy becomes higher than the zero-slippage energy, the high and the low frequency waveforms become more distinguishable.

In Figure 3.9d the spectrum FWHM is plotted versus the peak frequency. When approaching the zero-slippage condition at 160 GHz, the radiation pulse is only a few cycles long and its relative bandwidth approaches 50 %. The relative bandwidth is the maximum when the beam energy is at the zero-slippage condition. That the FEL bandwidth increases as the beam energy is the closest to the optimal condition is as expected. As the faster and the slower waves overlap at the zero-slippage condition, there is a single wide spectrum. While the pulselength was not measured simultaneously at the time, later measurements indicate around 25 ps FWHM [66], so the peak power would be around 2 MW.

The pulse energy is maximized at a higher average energy than the zero-slippage condition. The electrons arrive at the undulator with a spectrum of energies due to the energy spread and the transverse emittance. Electrons with energies below the zero slippage resonant energy cannot be phase matched and do not participate in the interaction, while the electrons with energies above the zero slippage resonant energy can be phase matched. As a result, there are more electrons participating in the FEL interaction when the average energy is above the zero-slippage condition.

Electron beam transmission through the vacuum pipe is more difficult as the average energy is lowered. The relation between the electron transmission and the beam energy can

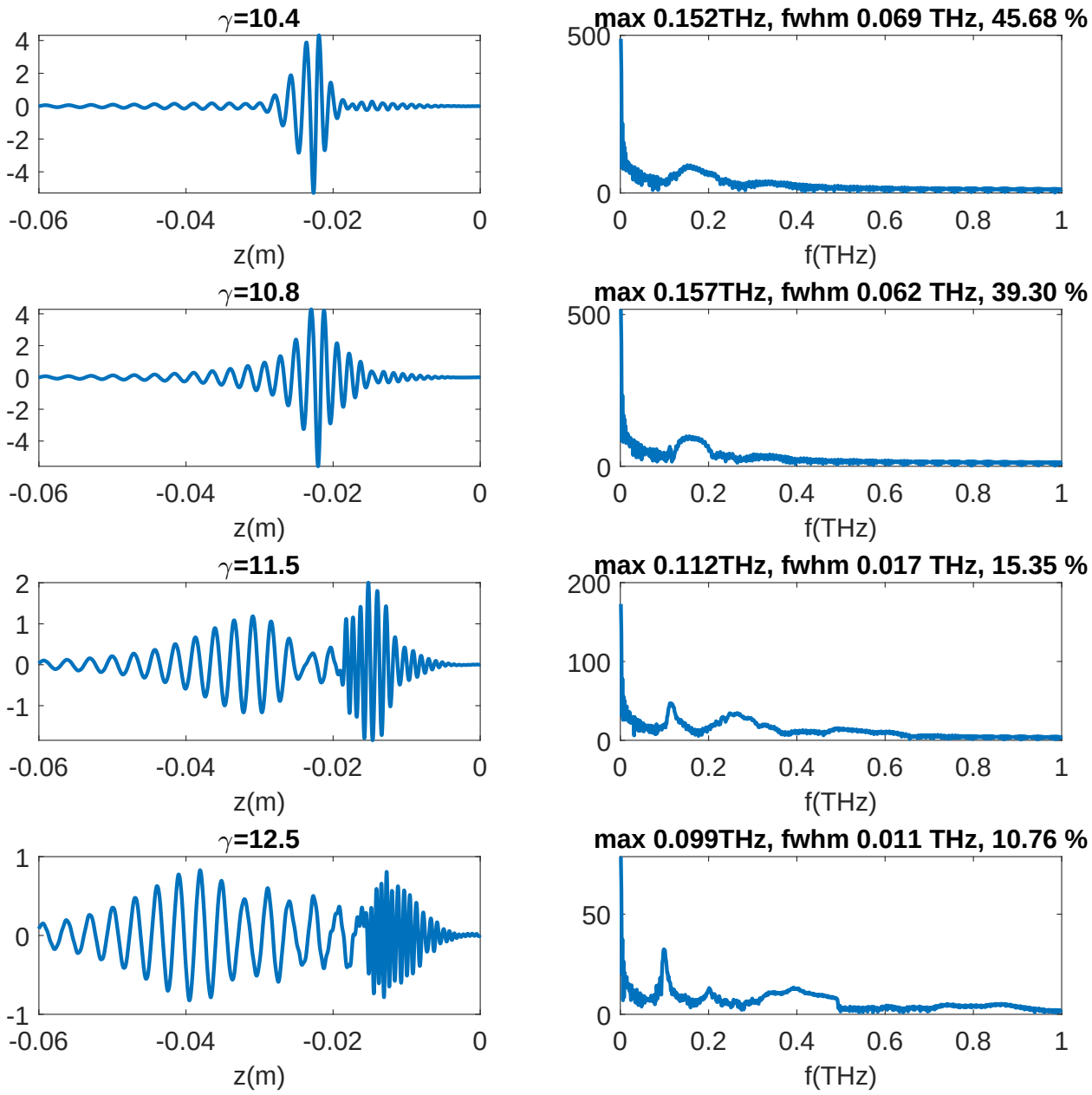

Figure 3.8: Radiation amplitudes from the GPT simulation at $\gamma = 10.4, 10.8, 11.5, and 12.5$, given a Gaussian input beam of 150 pC, 2 mm-mrad, σ_x=σ_z=0.3 mm, a pipe of radius 2.27 mm, and the Theseus undulator tapered from 0.73 to 0.52 T. The zero-slippage resonant energy for this system is $\gamma = 10.4$.

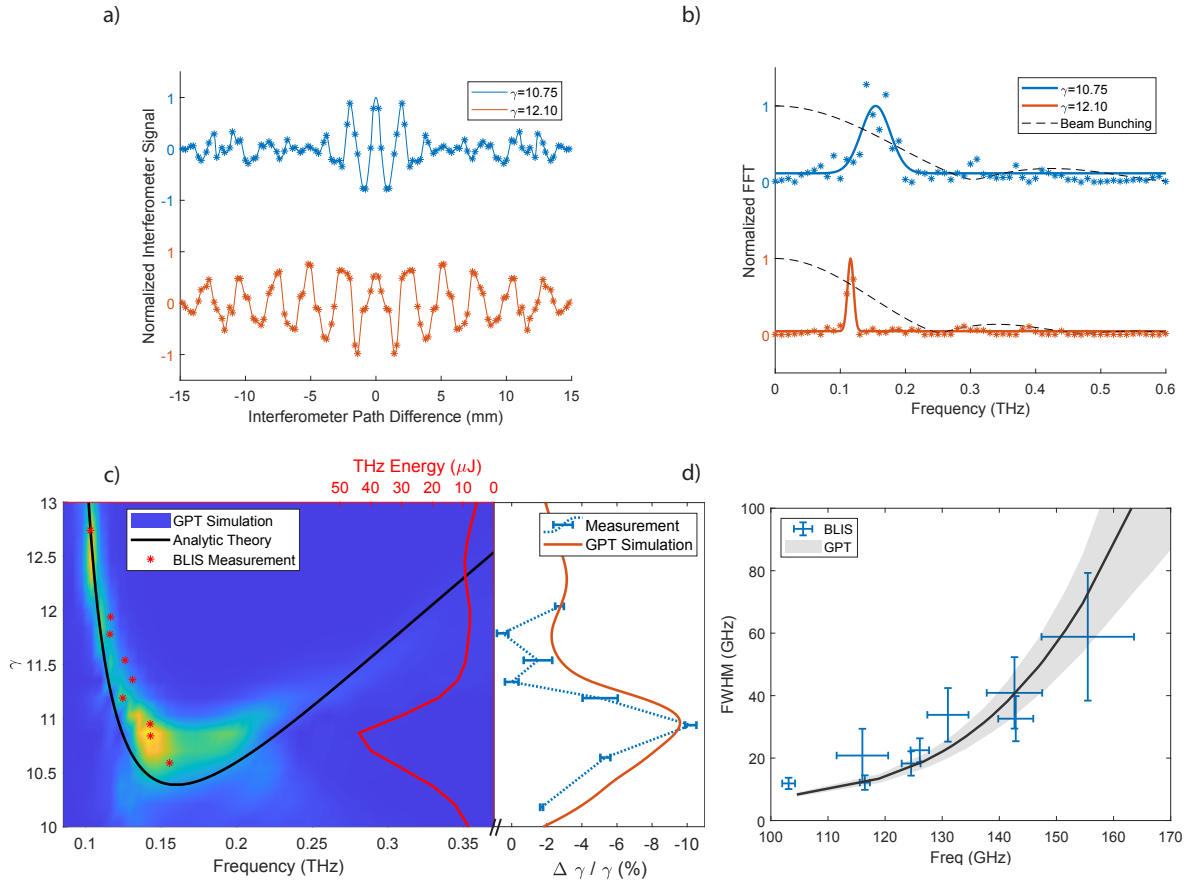

Figure 3.9: (a) Interferometer traces for input beam energies near (blue) and above (orange) the zero-slippage condition. (b) Power spectrum of the emitted radiation is computed from a FFT of the interferometer traces and plotted together with the beam bunching factors obtained from beam dynamics simulations. (c) The interferometer peak frequency measurements are compared to GPT simulations and to the theoretical phase-resonance curves. The simulated pulse energies show a maximum interaction at a slight positive energy detuning. Measurements of FEL efficiency vs input e-beam energy are plotted against GPT results. The charge in these simulations is scaled by the observed transmission through the undulator. (d) THz spectrum bandwidth (FWHM) is shown as a function of the peak radiation wavelength for measurements and simulation. Errors bars are 95% confidence intervals of gaussian fits to the spectral peaks like those shown in b).

be explained by the beam offset in the helical trajectory and the betatron oscillation. As shown in Figure 3.4a, the trajectory offset is greater at a smaller beam energy.

In the future, choosing a different set of waveguide size and beam energy will extend this scheme to the generation of higher frequencies. As shown in Figure 3.2, sending a beam with higher energy through a smaller waveguide will yield a higher frequency radiation. While the transmission through a smaller pipe can be more difficult, the ratio of the helical trajectory in the undulator to the waveguide remains constant as the resonant frequency is scaled (Equation 3.13). The betatron oscillation increases with the smaller pipe and higher frequency (Figure 3.4c), but additional matching optics can help reducing the increase. It will be helpful to design a pipe mount to help with straightening a thin pipe throughout the a meter-long undulator. Wakefield effects and electron beam size will eventually limit the pipe size and the possible terahertz frequency.

3.1 Supplemental simulation studies about the Pegasus-Tessatron system

The experimental parameters for the magnetic elements in the Pegasus beamline are optimized to measure the strongest FEL interaction. The laser spot size is chosen to extract the greatest amount of charge, while the gun phase is set at a standard position (17 degrees) where the beam transverse quality and the stability are more reliable. The triplet quadrupoles are optimized to match the beam into the undulator. While some choices are self-evident, more simulation studies help clarify the choices made for the solenoid and the linac.

In order to study the Pegasus beamline, the beamline elements as shown in Figure 3.5 are tracked using the GPT simulation from the photoinjector to the undulator entrance. Achieving a high brightness, compressed electron beam is possible without using a magnetic compressor when the electrons are accelerated at an off-crest phase from the maximum

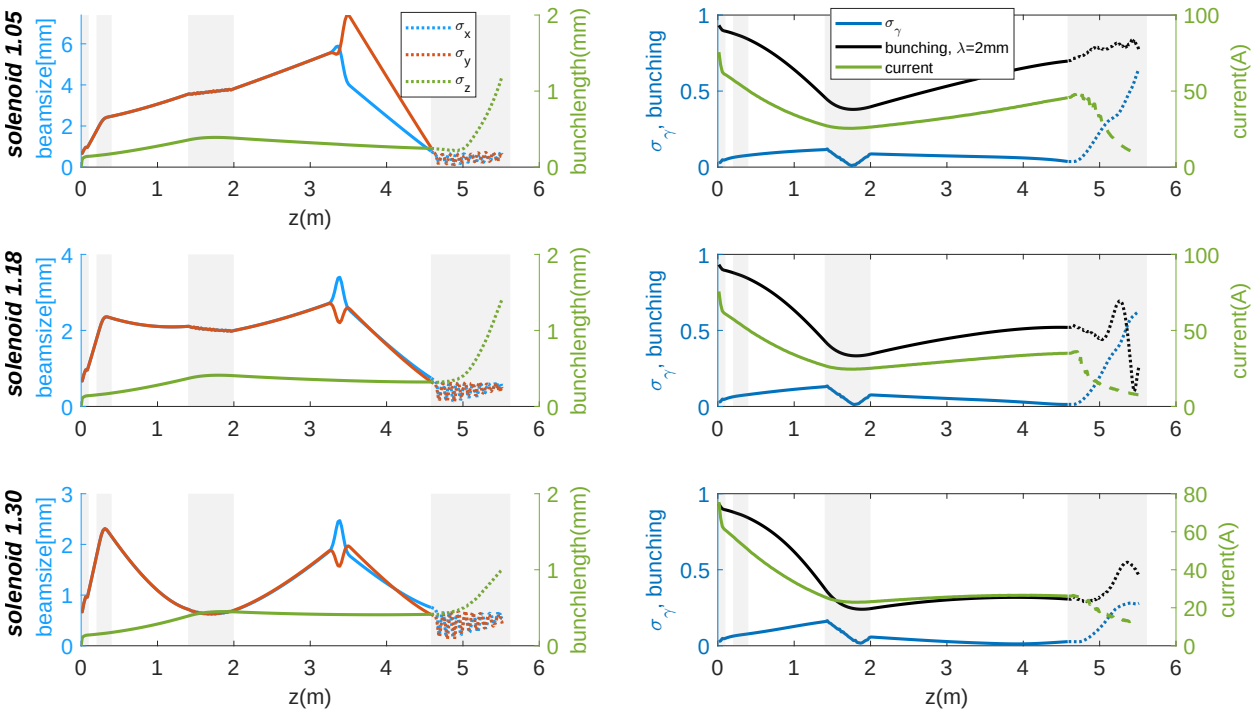

Figure 3.10: GPT simulation results at solenoids 1.05, 1.18, and 1.30 (bottom). The numerical values indicate the solenoid control value that can be converted to the peak field by $B[T] = 0.147 * [\text{controlvalue}] + .01$. The electron beam sizes (red and blue) and bunch length (green) are shown in the left side, and the energy spread (blue), bunching factor (black), and average current (green) are shown in the right side.

accelerating phase [100].

Figure 3.10 shows the difference in bunching at different solenoid strengths of 1.05, 1.18, 1.30. As the solenoid strength is increased, the beam size is more focused throughout the beamline, which increases the space charge effects. Meanwhile, the spot size is limited by the vacuum aperture size. Therefore, choosing the largest possible spot size that can travel in the beamline is ideal for recovering more density modulation.

The linac phase and the gradient also influence the FEL efficiency. Figure 3.11 shows the changes in the beam parameters with the linac phase. The maximum accelerating phase is at 90 degrees. As the phase is further away from 90 degrees, the energy spread expands

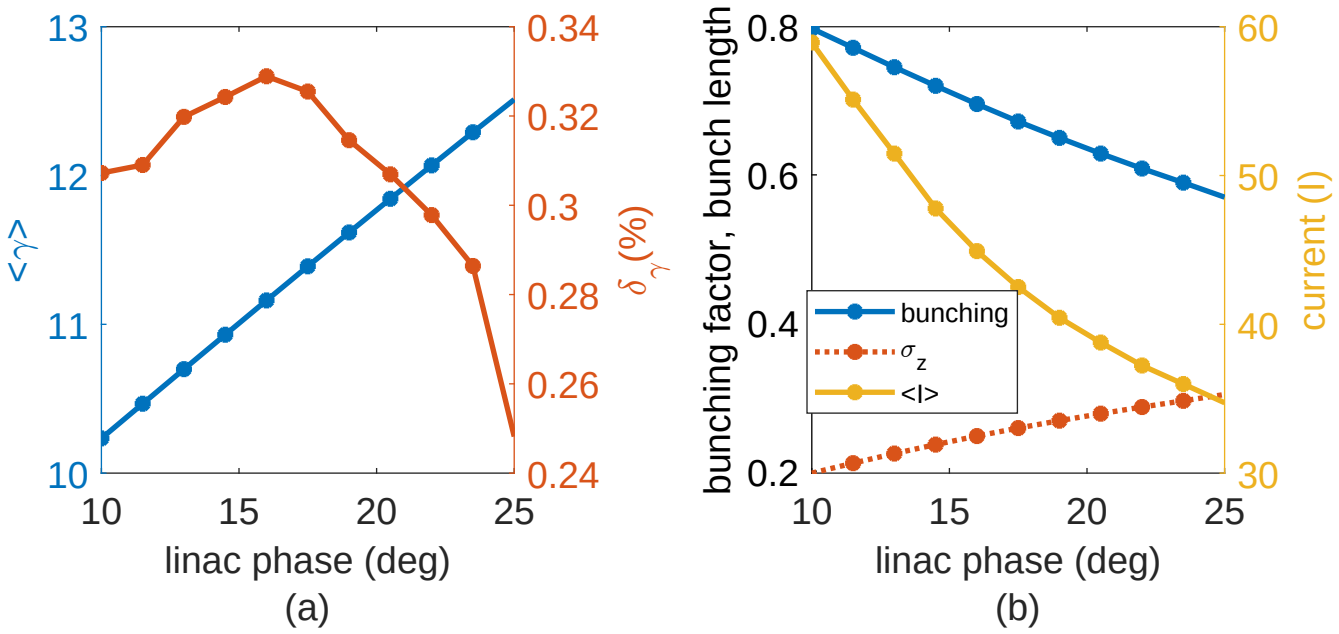

Figure 3.11: A linac phase scan from the photoinjector to the FEL. The phase at the maximum energy is 90 degrees. Maximum efficiency is obtained when the beam energy is near the zero-slippage resonant energy. The bunching factor is larger as the linac phase is further away from the maximum accelerating phase.

while the bunch length decreases. Because the THz wavelength is long compared to the bunch length, a smaller bunch length influences the bunching factor. Because a larger linac gradient causes more energy spread at a low energy and increases the bunching factor, a larger linac gradient is preferred.

The tapering of the undulator is optimized by varying the taper starting position z_t, the first order tapering t_1, and the second order tapering t_2 in $B(z) = B_0(1+t_1(z-z_t)+t_2(z-z_t)^2$. The optimization shows that delaying the tapering to 0.05 meters improved the efficiency. In the absence of a seed laser, the bunched electrons provide their own seed for the superradiant interaction. The gradient in the electron energy follows

$$\frac{\mathrm{d}\gamma}{\mathrm{d}z} = -\frac{KK_lk_s}{\gamma}\sin((k_w+k_s)z-\omega t) = -\frac{KK_lk_s}{\gamma}\sin(\theta_r) \tag{3.14}$$

as discussed in Chapter 1. Meanwhile, the zero-slippage resonant energy would change with

the undulator vector potential by

$$2\gamma_{zs}\frac{\mathrm{d}\gamma_{zs}}{\mathrm{d}z} = 2\frac{k_s}{k_\perp}K\frac{\mathrm{d}K}{\mathrm{d}z}, \tag{3.15}$$

so the tapering equation is

$$\frac{\mathrm{d}K}{\mathrm{d}z} = -k_\perp K_l \sin\theta_r. \tag{3.16}$$

Because the gradient in the tapering and the energy are related, imposing a quadratic tapering factor after a small distance should help in aligning with the superradiant growth in the radiation field.

Figure 3.12 shows a case of changing the linear and the quadratic tapering strength when the tapering delay was 0.05 m. The tapering is optimized when the linear term is up to -0.1 m^{-1} and when the quadratic term is between -0.3 and -0.4 m^{-2}. Similar scans at a tapering delay of 0.02 m and 0.10 m would show similar results.

Figure 3.13 shows the phase space evolution at different longitudinal positions. The input distribution is from the GPT simulation of the Pegasus beamline at $\gamma = 10.5$. Each phase space distribution is plotted with a separatrix calculated based on the radiation field at a resonant phase of 0.1 radian. The center of the distribution is closer to zero while the detrapped particles are eventually lost in the simulation. Based on the radiation field obtained from the simulation, one can try to back track the tapering based on Equation 3.16. The plot of the tapering that is tracked based on the radiation field aligns with the input tapering when ψ_r is around 0.1, indicating a very gentle tapering. When a more abrupt tapering was applied as shown in Figure 3.14, the deceleration is more abrupt initially, but the particles are detrapped. It is possible that varying the position where the linear tapering begins would help with the optimization. As shown in Figures 3.13a, the deceleration enters a linear regime as more particles are detrapped, so an optimal tapering could be more complicated.

Updating the tapering based on the radiation field would have been interesting, but a code to update the tapering in the GPT-FEL simulation was not written during the project

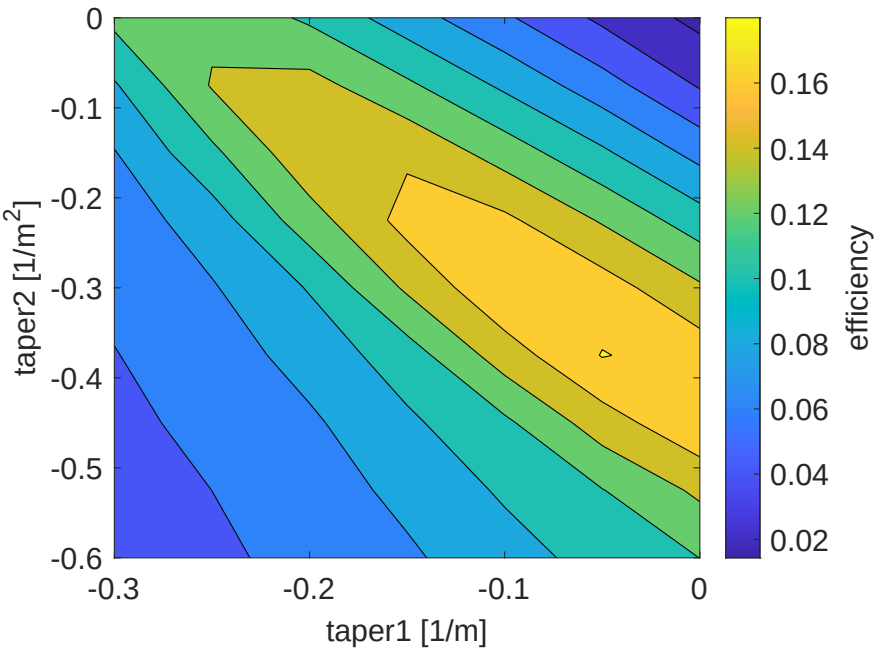

Figure 3.12: The efficiency of the THz undulator is computed for different linear and quadratic tapering parameters, when the undulator field is varied by $B = B_0(1 + t_1(z - z_t) + t_2(z - z_t)^2$. Tapering delay z_t is kept constant at 0.05 m.

period. Currently, the code is written to compute the undulator field and the radiation field in two separate custom functions. It should be possible to optimize the tapering based on the radiation growth once the two codes are combined.

The bunching factor is a critical factor to initiate the FEL process and influences the efficiency significantly. As shown in Figure 3.15a, the FEL efficiency degrades by 70% when the bunching factor is reduced by half. As shown in Figure 3.11, the linac phase is moved from the crest to reach the resonant energy while bunching the beam in the current beamline setup. In order to experiment with a higher frequency, it is necessary to reach a higher energy than the current configuration, while remaining at a similar magnitude of the bunching factor. This means the beam needs to be bunched in a different way than the velocity bunching. Instead of increasing the linac gradient to achieve a compressed beam at a higher energy, adding a magnetic chicane can provide more control in the compression.

The simulation shows high tolerance as for the energy spread. An energy spread of 10% is shown to degrade the efficiency by around 12% from the maximum (Figure 3.15b). This is because the energy spread should be smaller than the Pierce parameter ρ for a good FEL interaction [86]:

$$\sigma_E/E < \rho, \tag{3.17}$$

where the Pierce parameter is around 0.05 for this system. Even though the energy spread measured before the undulator is relatively large because of the off-crest phase set for the velocity bunching (around 7%), the input beam is sufficient to see the FEL interaction because of the high tolerance in the energy spread.

For an ideal FEL interaction, the transverse emittance should be much smaller than the resonant wavelength,

$$\epsilon < \frac{\lambda}{4\pi}. \tag{3.18}$$

Because of the long terahertz wavelength, the tolerance on the emittance is also relatively

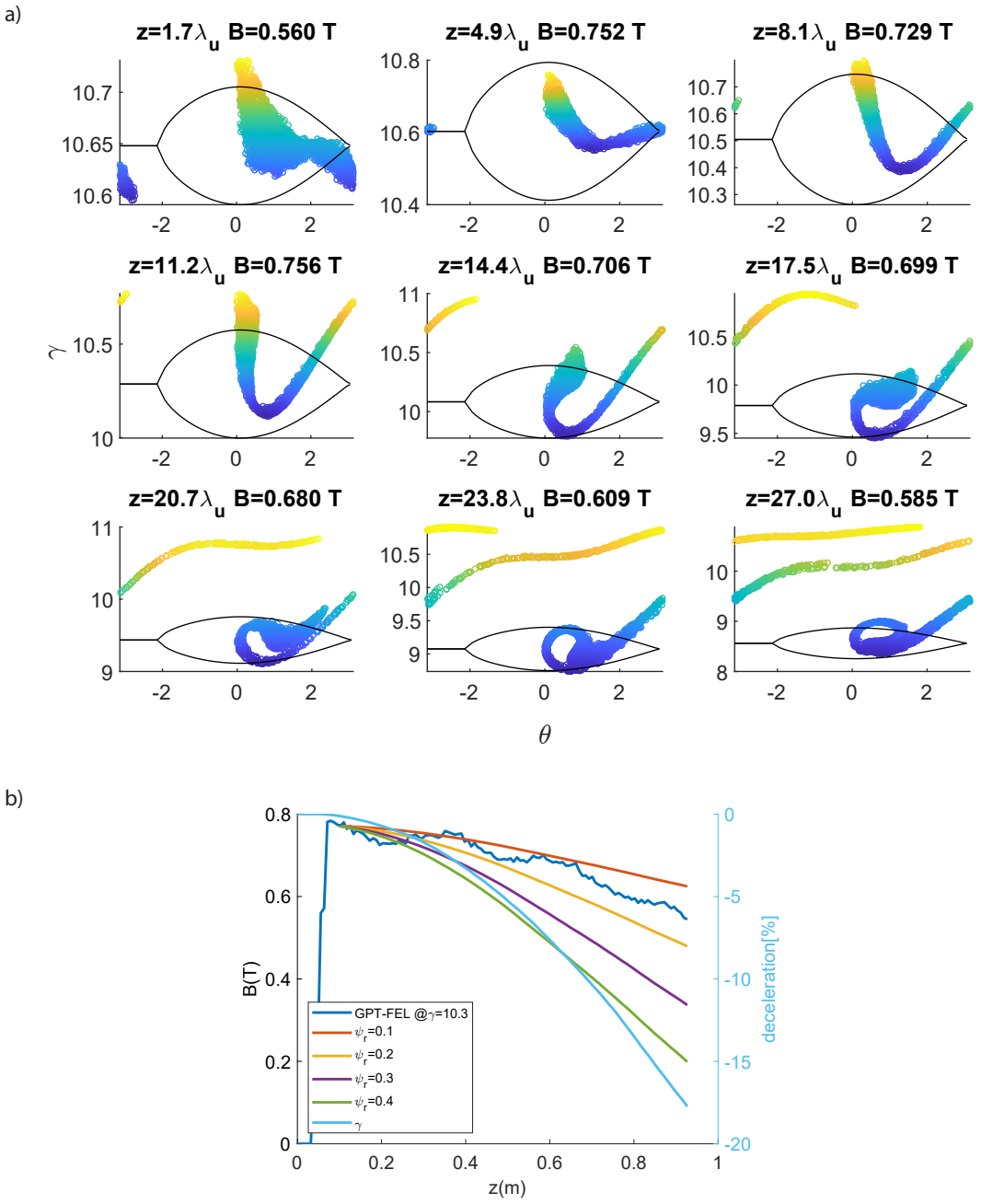

Figure 3.13: a) Phase space evolution in the GPT simulation, plotted with resonant phase at ψ_r=0.1. b) Input tapering is compared with the tapering tracked based on Equation 3.16 and the radiation field at different resonant phases.

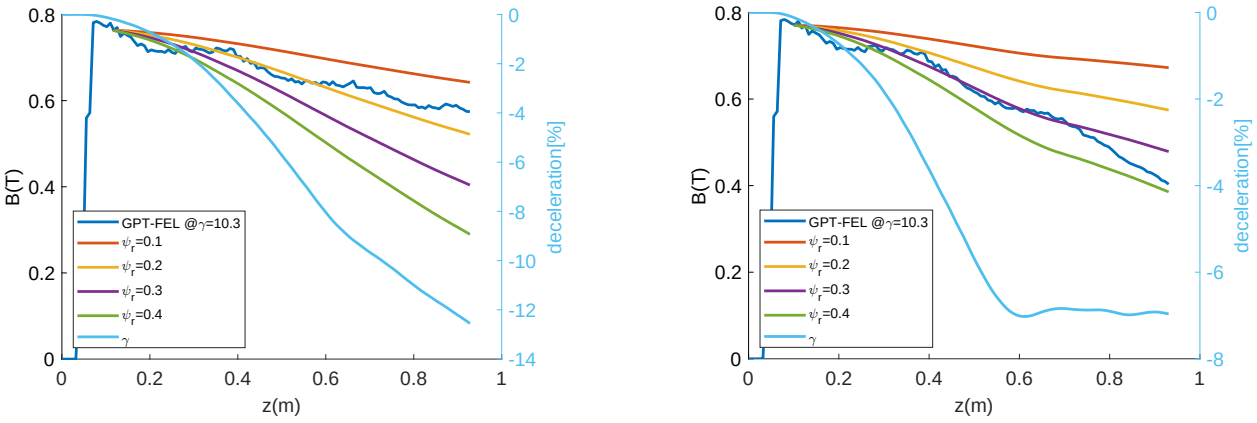

(a) (b)

Figure 3.14: Tapering schemes more abrupt than the ideal case are compared at different resonant phases. a) t_1 = -0.3m^{-1}, t_2 = 0m^{-2} b) t_1=-0.25m^{-1}, t_2 = -0.38m^{-2}.

high. In the simulation, a transverse emittance of 20 mm-mrad degrades the efficiency by 40% (Figure 3.15c).

The simulation shows that a transverse beam size of 2 mm in both vertical and horizontal size decreases the efficiency by 50 % from the maximum (Figure 3.15d). The matched beam size of 150 μm is not easy to achieve in the experimental setup; the beam size measured is around 300 to 400 μ m. One way to better focus the beam size in the future is to add another solenoid.

To summarize, the magnet parameters of the Pegasus beamline elements are chosen to demonstrate the best FEL interaction from the available setup. The chosen solenoid field is weak enough to transport a large beam that fits in the vacuum apertures while minimizing the space charge effects, retrieving more density modulation at the undulator entrance. The linac phase is set at an off-crest, while the linac gradient is set close to the maximum achievable, in order to increase the bunching factor. The undulator tapering is chosen based on optimizing the linear and quadratic parameters. The chosen tapering parameter appears to be a rather gentle choice based on the resonant phase of 0.1-0.2. In addition, the tolerances of the bunching factor, energy spread, transverse emittance, and transverse beam size are

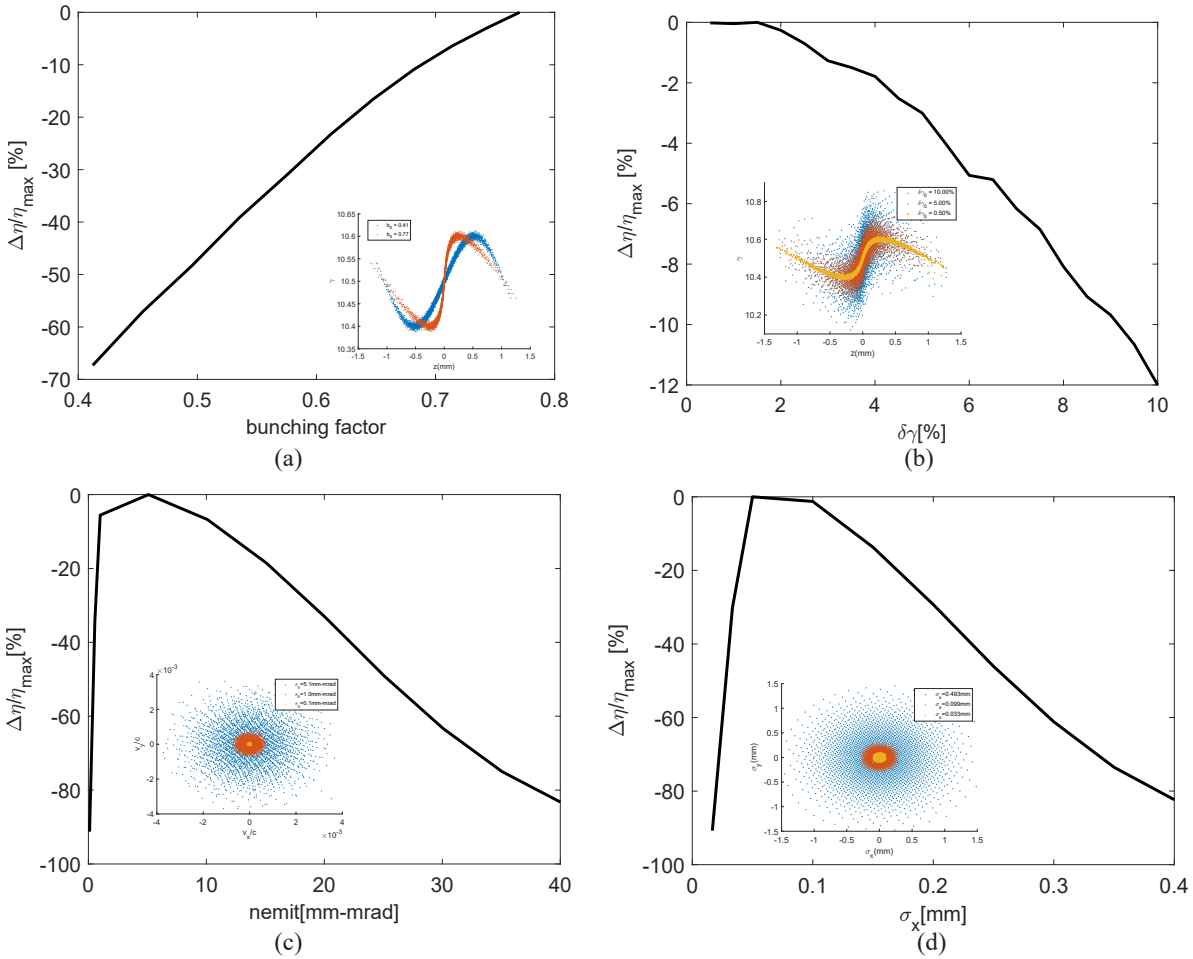

Figure 3.15: Tolerance studies of the GPT-FEL simulation. (a) The bunching factor is varied by varying the modulation amplitude of an arbitrary initial Gaussian bunch. The changes in the longitudinal phase space of the input beam at bunching factor of 0.41 (blue) and 0.77 (red) are shown. (b) The energy spread is varied up to 10% which shows 12% decrease from the maximum efficiency. The longitudinal phase space at energy spreads of 10% (blue), 5% (red), and 0.5% (yellow) are shown. (c) The transverse emittance is varied up to 40 mm-mrad. The changes in the transverse divergence at normalized emittance of 5 mm-mrad (blue), 1mm-mrad (red), and 0.1mm-mrad (yellow) are displayed. (d) The transverse beam size is varied up to 0.4 mm. The changes in the transverse distribution at spot sizes of 0.49 mm (blue), 0.10 mm (red), and 0.03 mm (yellow) are displayed.

examined. While all of the tolerance parameters are achievable from the current setup at a low energy, achieving the required longitudinal compression and the transverse beam size at a higher energy will need additional beamline elements such as a magnetic chicane or a solenoid.

APPENDIX

3.A Measurement protocols in the Pegasus Beamline

This section discusses the recent upgrades in the measurement methods for the Pegasus beamline. While the spectrometer parameters have been provided earlier in this chapter, this section shows the energy measurement before the undulator while discussing the stitching method. The quadrupole scan section discusses optimizing the transverse size of the input beam, which is also a critical factor for the THz experiment. The charge scan section discusses a recent installation that improves the charge measurements and explains how the automated scans are done to obtain the experimental results. The solenoid scan section provides an example of a scan and how the scan is used given different goals.

3.A.1 Quad scan

The Pegasus beamline has six quadrupoles installed after the linac, before the undulator. For the THz experiment, the last three quadrupoles are used to focus the beam for sending to the undulator. The quadrupoles' strengths can be adjusted manually, but a quadrupole scan helps with finding an ideal set of quadrupole strengths.

The quadrupole strengths are scanned via a Matlab script in an external desktop. In order to match the beam size at the undulator entrance, the triplet is scanned based on an analytic calculation. Based on the position of Screen 4, the three quadrupoles, and the PIMAX 3 screen (the high resolution camera before the undulator), the transverse transport matrices are used to estimate the beam size at different quadrupole settings. At low charge, it is possible to estimate the matching quadrupole parameters. The transport matrix is

$$\sigma_f = M\sigma_i M^t \tag{3.19}$$

used to calculate the spot size at the PIMAX screen, where M is a multiplication of the

matrices for each element in the FODO lattice of the beamline. A Matlab optimizer is used to minimize the spot size and the difference between σ_x and σ_y to find a round waist solution. While this method is good for a low charge, the result diverges as the charge increases due to the space charge effects. Accordingly, the quadrupole parameters are scanned based on a matching solution given different distances d_s from the position of the last quadrupole to the PIMAX 3. At each d_s, the quadrupole settings and the beam size are recorded ten times. The beam sizes σ_x and σ_y are obtained based on fitting the projection of the image intensity in the x and the y direction to Gaussian distribution. After a scan of quadrupole settings at different d_s is complete, an optimizer is run to find the best beam matrix at Screen 4 that yields the analytic values that are the closest to the measured values. Based on the initial σ-matrix optimized, the emittance can be calculated. A limitation in this method is that an initial beam matrix solution is needed in order to calculate the quadrupole solutions for a round waist. Using the initial beam matrix solution, it is possible to feed into the simulation a distance that focuses the beam at the undulator entrance.

Although this beam matrix does not need to be exact, an unusually shaped initial beam at Screen 4 can be difficult to analyze. Usually, the scan can eventually find a matching solution after a couple of iterations, feeding back the optimized initial beam matrix for the next scan. A beam that is too focused at Screen 4 will not focus well at PIMAX, and the result diverges. An initially vertical beam may not have a good round waist solution, so the analyzer has difficulties finding a good set of quadrupole inputs for the scan. Although the analysis diverges from the measurements with a higher charge and lower quality input beam, the scan is able to find an approximate solution for the beam that can be sent to the undulator. Figure 3.A.1 shows an example running a quad scan operated at a low charge.

3.A.2 Charge scan

The Pegasus beamline has recently installed a Turbo Integrated Transformer, which can measure a bunch charge that passes through the assembly. As the beam passes through the

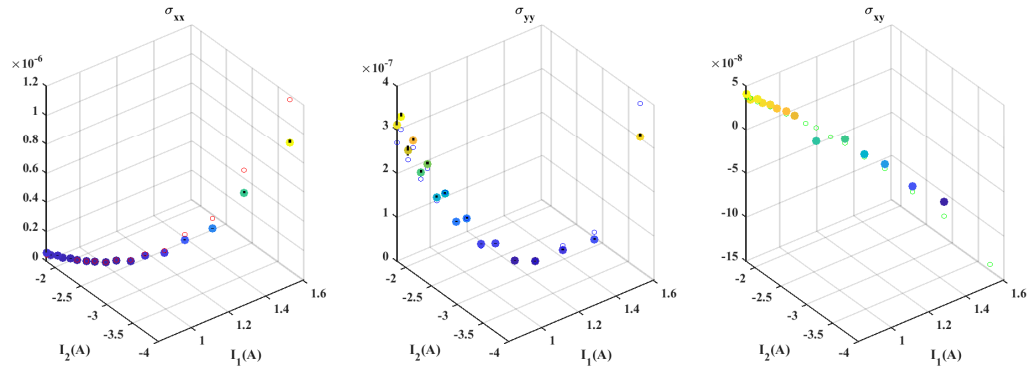

Figure 3.A.1: An example of quad scan output at charge = 300 fC, laser spot size 0.2 mm. The quad scan analyzer shows that the transverse emittance is 0.3 mm-mrad.

coils, the induced current is analyzed as a charge measurement. This method is a significant improvement from using a Faraday cup to measure the charge. A Faraday cup is a metal cup attached at the end of a beamline, and when electrons hit the metal, the induced current sends the voltage to the scope. In order to measure the charge using a Faraday cup, the beam needs to be sent to the end of the beamline, so it is not possible to inspect a full image of a beam. Because the ICT can measure the charge as the beam travels in the beam line, both the charge and the full image of the beam at each shot can be captured simultaneously.

In the Pegasus beamline, the ICT is installed after Screen 2 (Figure 3.5). The trigger of the ICT should be synchronized with the cameras, and then the trigger delay can be fine-tuned within 250 ns. The ICT is read from a Labview VI that reads the virtual cathode camera (VCC) parameters simultaneously, recording the output value of the ICT and the virtual cathode in a database. The synchronization is limited because the camera and the ICT information do not arrive exactly together, but when the camera receives a signal, the VI records a signal from the ICT that is simultaneous or the latest data available.

Measurement of the quantum efficiency is important for quantifying the characteristics of a photoinjector setup. The quantum efficiency (QE) is defined by the number of electrons per the number of photons. The number of electrons can be measured from the charge of

the bunch. To measure the number of photons one can measure the laser energy and divide by the Plank constant:

$$QE = \frac{n_e}{n_\gamma} = \frac{Q}{E_\gamma[eV]} \frac{1240[eVnm]}{\lambda[nm]} \tag{3.20}$$

where E_γ is the laser energy and λ is the wavelength of the laser for the photocathode.

One way to measure the laser energy is to calibrate the intensity of a portion of the input laser energy shown on the virtual camera. The beam splitter is set to send around 1% of the input photocathode laser to the virtual cathode camera placed at a position equidistant with the position of the cathode. A known amount of laser energy is sent to the VCC, and the gaussian sum is recorded. Then, while the laser is sent to the photoinjector to inject an electron beam so that its charge is detected by the ICT, the VCC image recorded by the same VI is used to measure the simultaneous laser energy. The laser energy intensity is controlled by a polarizer connected to a stepper motor, and using a Matlab or a Python script one can control the motor and record the concurrent data into the database. Figure 3.A.2 shows an example of a QE measurement. An advanced photocathode made of Na-K-Sb showed an efficiency of 5e-3, which is a great improvement from a copper cathode which has a QE around 2e-6.

The improved charge scan protocol helps confirm the measurements that are previously were done manually by a few data points of charge and screen intensity done. The linearity of the data shown in Figure 3.A.2 is one way to confirm that the measured relation between the charge and the virtual cathode image works at any charge. The concurrent measurement of the charge and the screen image can be used for calibrating any of the screens. Using the Spec. 2 camera to record the energy spread as shown in Figure 3.7 demonstrate another way that the charge scan protocols are implemented, in which the charge, the electron beam spectrum, and the THz radiation energy are measured simultaneously while a script records the reference number for the saved data and moves the stepper motor for the next value of charge.

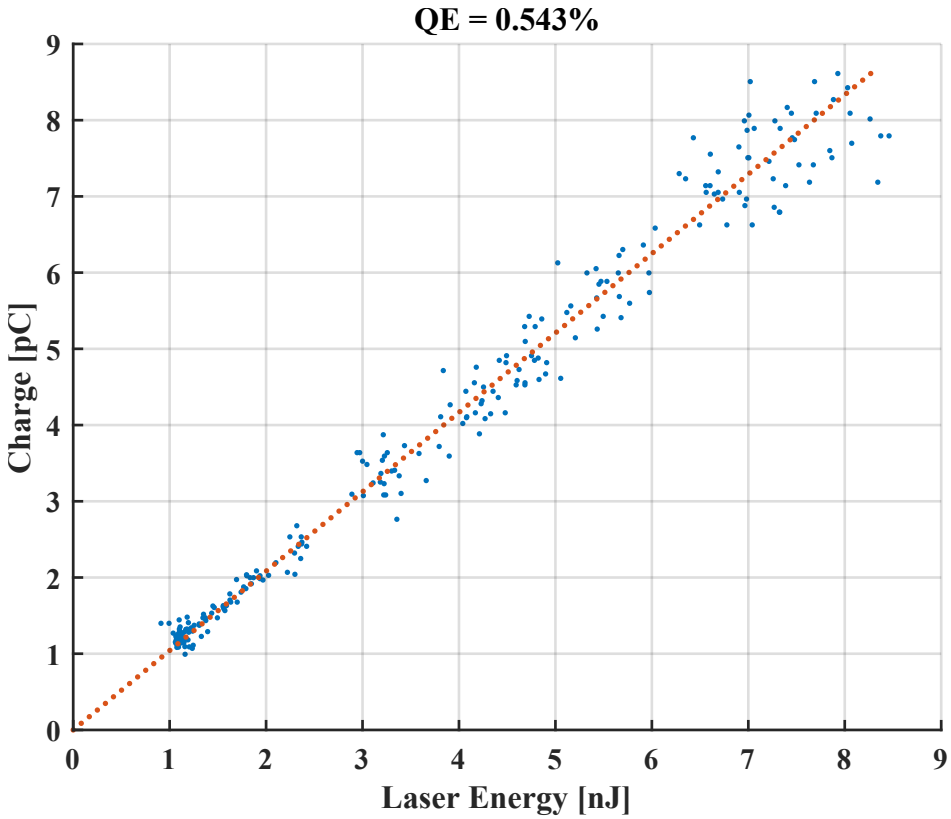

Figure 3.A.2: Q.E. measurement of an advanced photocathode made of Na-K-Sb based on the ICT and the VCC.

3.A.3 Solenoid scan

A solenoid scan of the electron beam that arrives at Screen 2 before the linear accelerator helps compare the experimental data with the simulation results. The solenoid value is controlled by a virtual serial port that can be connected from Labview, and the input control value changes the field in the solenoid approximately by $B[T] = 0.147 * [\text{controlvalue}] + .01$. The solenoid scan script is written in Labview, in which a user can input the number of data points to take and the range of the solenoid values. Because the beam focuses or defocuses transversely as the solenoid control value is changed, the gain of the camera needs to be adjusted either because of the saturation or because the beam is not as visible. A user can input a range of the screen intensity that the VI can accept as a data point, and the gain is adjusted if the condition is not met. Figure 3.A.3 shows an example of the solenoid scan.

The solenoid scan is a good way to measure the transverse emittance. Because the beam emittance is the determinant of the σ-matrix, the changes in the beam size as the solenoid value is varied can be used to determine the beam emittance. The solenoid and the drift elements correspond to the transport matrices of

$$M_s = \begin{pmatrix} 1 & 0 \\ k & 1 \end{pmatrix} \quad M_d = \begin{pmatrix} 1 & D \\ 0 & 1 \end{pmatrix} \tag{3.21}$$

where $k = -\frac{1}{f}$ is the solenoid strength, which can be expressed in terms of the solenoid field as

$$k = \frac{1}{4}\left(\frac{e}{p}\right)^2 B_s^2 L_s. \tag{3.22}$$

The total transport after a solenoid of strength K and a drift of length D is

$$M = \begin{pmatrix} 1 + kL & L \\ k & 1 \end{pmatrix}. \tag{3.23}$$

The σ-matrix can be written as

$$\sigma = \begin{pmatrix} s_{11} & s_{12} \\ s_{21} & s_{22} \end{pmatrix}, \tag{3.24}$$

where the first element is the square of the beam size $s_{11} = \sigma_x^2$. The σ-matrix can be transported to a position after a solenoid and a drift by

$$\sigma_f = M\sigma_i M', \tag{3.25}$$

from which the following relation can be obtained

$$\sigma_{11} = (s_{11}d^2)k^2 + (2ds_{11} + d^2(s_{12} + s_{21}))k + (s_{11} + d(s_{12} + s_{21}) + d^2 s_{22}), \tag{3.26}$$

which shows that the square of the transverse beam size is related to the solenoid strength k to the second order. This means that a quadratic fit of the beam size and the solenoid strength can be used to match with each of the zeroth to the second order terms. Expressing the above as

$$\begin{aligned} A = P_1 &= s_{11}d^2 \\ -2AB = P_2 &= 2s_{11}s + 2s_{12}d^2 \\ C + AB^2 = P_3 &= s_{11} + 2s_{12}d + s_{22}d^2 \end{aligned} \tag{3.27}$$

where

$$\sigma_{11} = P_1 k^2 + P_2 k + P_3 \tag{3.28}$$

it is possible to find that the transverse emittance is related to the coefficients as

$$\epsilon^2 = det[\sigma] = s_{11}s_{22} - s_{12}^2 = \frac{AC}{d^4} = \frac{P_1 P_3 - \frac{1}{4}P_2^2}{d^4}. \tag{3.29}$$

Therefore, the transverse emittance is measured based on the quadratic fit of the beam size and the solenoid focusing strength. Figure 3.A.3 shows an example of solenoid scan data. A solenoid scan at a charge of 300 fC and laser spot size of 115 μm showed a normalized emittance of 3.5 mm-mrad. The result is compared with a GPT simulation of a solenoid scan that results in a similar fit, which also shows 3.5 mm-mrad based on the quadratic curve of the solenoid scan result, and 3.3 mm-mrad based on the output distribution.

The GPT simulation in Figure 3.A.3 is run with a laser spot size larger than the measured laser spot size to match the result with the quadratic curve of the data. As shown in the

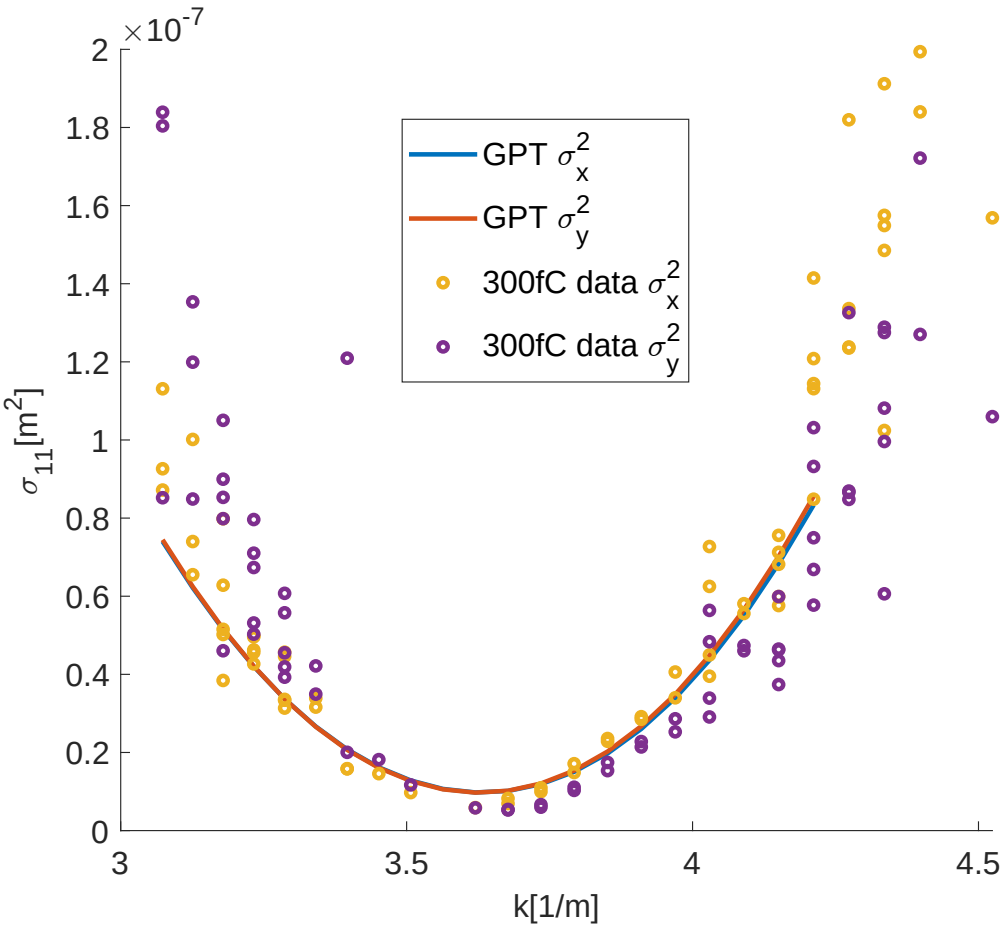

Figure 3.A.3: Solenoid scan data at a charge of 300 fC and the laser spot size of 115 μm plotted in terms of the solenoid strength k and s_{11} matrix element.

relation $P_1 = s_{11}d^2$, the squares of the initial spot size and the solenoid distance influence the steepness of the curve. The difference in the simulation and the data can be due to the measurement errors. The distance from the gun to the solenoid and the screen is measured by a measuring tape, and there can be errors in orders of centimeters. The virtual cathode may not have shown an accurate image of the spot size at the cathode. The laser intensity is adjusted to see a small spot size on the screen because the laser spot at a low charge setting is too dim. Meanwhile, the mean transverse energy and the gun voltage values in the simulation change the position and the value of the minimum spot size. The calibration for the solenoid and the gun voltage as well as an accurate input model of the gun also influence the simulation. That the space charge effects dominate the front-end section where the energy is low does not help because the mesh to study the space charge effects increases the simulation time significantly. The solenoid scan data of the Pegasus beamline have been generated for machine learning and neural network studies to improve the simulation time in providing an accurate model of the experiment.

3.A.4 Spectrometer

Among the three spectrometer dipoles available to measure the electron energy, Spec. 1 and Spec. 2 are equipped with high-resolution PIMAX cameras which allow visualizing the details of the bunch shape. Because of the large energy spread caused by the velocity bunching, the spectrometer images are stitched to visualize the entire bunch. In order to combine the images shown at different dipole currents, the current value is recorded while monitoring the same energy-position of the bunch. When the images are combined, the pixel distance between images provides the energy value at each position of the bunch. Figure 3.A.4 shows an example of a long e-beam bunch shown on Spec. 1. Stitching involves combining the images of the screen, so the background has been cleaned up for the purposes of the illustration. After the images are obtained, the charge is reduced to compare the energy at a low charge at which the energy spread is small enough to fit in a screen. The

spectrometer design can be improved by incorporating a larger screen and adding focusing.

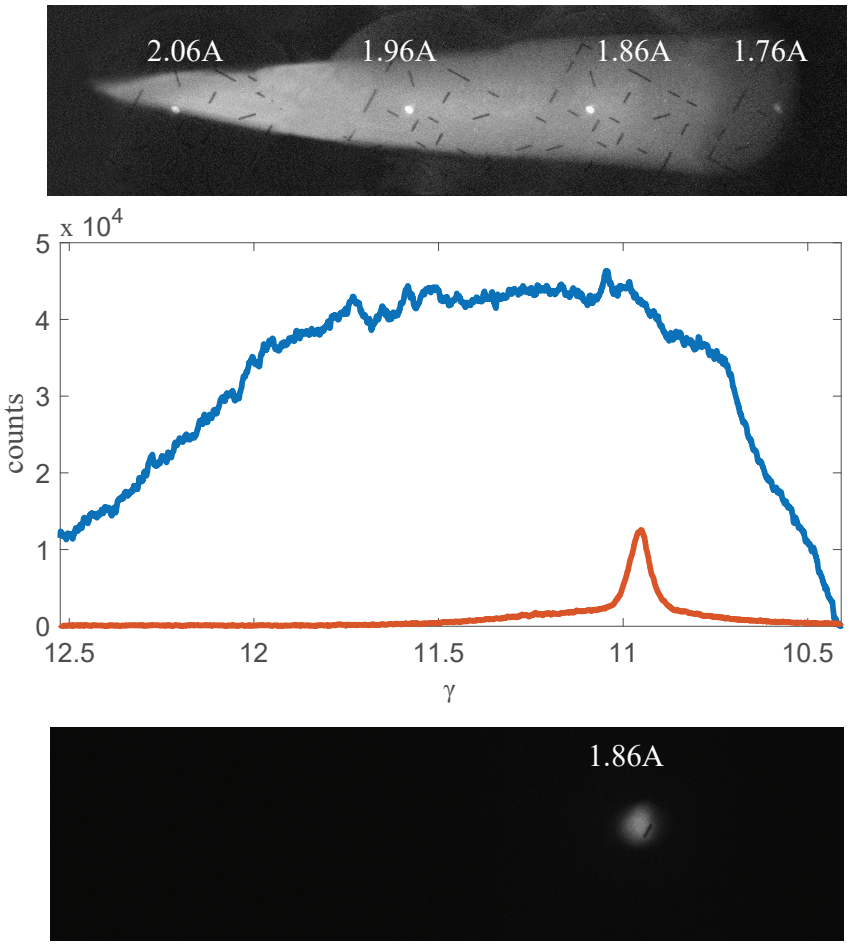

Figure 3.A.4: Spectrometer measurements at a high charge (220 pC) and a low charge (2 pC). Top) A cleaned illustration of the spectrometer images stitched at different currents as indicated on the image. Center) Horizontal projections of the image intensities at a high and a low charge plotted with the energy values estimated based on the pixel position. Bottom) Low charge energy measurement combined to align with the high charge energy measurement.

CONCLUSION

The high gain regime of a prebunched electrons in a strongly tapered undulator system has been studied as a part of the Tapering Enhanced Stimulated Superradiant Amplification program. While this document mostly explores the single-pass scenario in which the peak power and the pulse energy are optimized, the ultimate goal of the program is to increase the average beam power. Many research areas demand high average power radiation sources in order to move forward and actualize the conceptual designs. A short wavelength and high power light source is important for EUV lithography to increase the resolution and the productivity. Propulsion of a light spacecraft is expected to become much less costly with a high average power radiation source. A high average power THz source can provide the radiation source for plasma ignition and nuclear power.

As a coherent, wavelength tunable radiation source that operates in vacuum, the free electron lasers have great potential to meet the demands of the science community. Utilizing prebunched electron beams and strongly tapered undulators, the TESSA program aims to actualize an FEL-based high average power, high efficiency radiation source by utilizing strongly tapered undulators and prebunched electron beams. The study of a single-pass TESSA system explored in this document is an early step towards that goal. While the previous Nocibur experiment has already verified the electron beam deceleration at a low gain regime, this document discusses the experimental design, simulation optimization, and diagnostics involving a TESSA system in a high gain regime. The COVID situation and the government laboratory schedule hindered the demonstration of the system, but the future experiment at FAST facility will put together the discussed designs in reality. The FAST facility is a good place to also explore the oscillator setup due to the high repetition rate of the electron beams.

While the tapered FELs have been studied in extensive analytical detail in history, this document has explored the three dimensional effects of a high gain, strongly tapered FEL

that have not been fully studied. Utilizing the three dimensional FEL simulation and the modern computing resources, the tapering is optimized based on the radiation diffraction in the undulator. The high performance parallel computing available today also allows an optimization of a start-to-end electron beamline by studying different input parameters of a system simultaneously. The start-to-end simulation studies for the LEA-TESSA system involves moving between multiple accelerator codes. The FEL simulation developed at UCLA uses GPT simulation and allows placing the elements from the photoinjector to the FEL and to the diagnostics in one beamline. Meanwhile, matching the simulation with the experimental results is not a simple task and depends on the accuracy of several measurements such as the distance between the beamline elements, the length and the field map of each element, or the calibration from the values at the laboratory to the physics parameters in the simulation.

An alternate experiment conducted at UCLA explores the strongly tapered case of a zero slippage interaction in the THz wavelength. While the TESSA undulator is designed for an UV range wavelength, the waveguide dispersion relation allows a much longer radiation wavelength. A high average power THz radiation source is also in high demand in the plasma and nuclear research, so there is a strong motivation to explore the capability of an FEL based radiation source. A high gain regime of the zero slippage interaction has been explored by matching the resonance condition with the undulator waveguide. The experimental verification of the high efficiency and high peak power at 10% and 2 MW from a single-pass zero-slippage, superradiant interaction shows a great possibility that the oscillator setup of the system can exhibit a substantial amount of average power. Experimental designs for a higher THz frequency and an oscillator setup are in progress. In the case of an 100-Hz S-band thermionic injector which has been developed at Radiabeam [65], one can expect an average power of around 15 W THz radiation.

Because the relevant research areas such as the lithography, space exploration, plasma fusion, and nuclear power are highly intertwined with important technologies in contempo-

rary society, and because the free electron lasers have already shown great advantages in their high brilliance, tunability, coherence, and vacuum interaction (less dependence on the repetition rate), the continued exploration to reach a high average power and high efficiency from a free electron laser will be a significant addition to the science community.

REFERENCES

[1] R. Akre, L. Bentson, P. Emma, and P. Krejcik. A transverse rf deflecting structure for bunch length and phase space diagnostics. In *PACS2001. Proceedings of the 2001 Particle Accelerator Conference (Cat. No. 01CH37268)*, volume 3, pages 2353–2355. IEEE, 2001.

[2] R. Alkofer, M. Hecht, C. D. Roberts, S. Schmidt, and D. Vinnik. Pair creation and an x-ray free electron laser. *Physical Review Letters*, 87(19):193902, 2001.

[3] J. Amoani. Intensity Dependent Nonlinear Refractive Index of Fused Silica. Master's thesis, University of Eastern Finland, 2019.

[4] K. Bane and G. Stupakov. Corrugated pipe as a beam dechirper. *Nuclear Instruments and Methods in Physics Research Section A: Accelerators, Spectrometers, Detectors and Associated Equipment*, 690:106–110, 2012. doi:10.1016/j.nima.2012.07.001.

[5] K. Bane, G. Stupakov, and I. Zagorodnov. Analytical formulas for short bunch wakes in a flat dechirper. *Physical Review Accelerators and Beams*, 19:084401, Aug 2016. URL: https://link.aps.org/doi/10.1103/PhysRevAccelBeams.19.084401, doi:10.1103/PhysRevAccelBeams.19.084401.

[6] K. L. Bane, T. L. Barklow, M. Breidenbach, C. P. Burkhart, E. A. Fauve, A. R. Gold, V. Heloin, Z. Li, E. A. Nanni, M. Nasr, et al. An advanced ncrf linac concept for a high energy e^+e^- linear collider. *SLAC-PUB-17301*, 2018.

[7] A. Barty, J. Küpper, and H. N. Chapman. Molecular imaging using x-ray free-electron lasers. *Annual Review of Physical Chemistry*, 64(1):415–435, 2013. URL: https://doi.org/10.1146/annurev-physchem-032511-143708.

[8] K. Batchelor, H. Kirk, J. Sheehan, M. Woodle, and K. McDonald. Development of a high brightness electron gun for the accelerator test facility at brookhaven national laboratory. 1 1988. URL: https://www.osti.gov/biblio/7058521.

[9] S. Benson, D. A. G. Deacon, J. N. Eckstein, J. M. J. Madey, K. Robinson, T. I. Smith, and R. Taber. Optical autocorrelation function of a 3.2-μm free-electron laser. *Phys. Rev. Lett.*, 48:235–238, Jan 1982. URL: https://link.aps.org/doi/10.1103/PhysRevLett.48.235, doi:10.1103/PhysRevLett.48.235.

[10] S. V. Benson. What Have We Learned from the kilowatt IR-FEL at Jefferson Lab? *Nucl. Instrum. Meth. A*, 483:1–7, 2002. doi:10.1016/S0168-9002(02)00276-0.

[11] R. Bonifacio, B. W. J. McNeil, and P. Pierini. Superradiance in the high-gain free-electron laser. *Phys. Rev. A*, 40:4467–4475, Oct 1989. URL: https://link.aps.org/doi/10.1103/PhysRevA.40.4467, doi:10.1103/PhysRevA.40.4467.

[12] R. Bonifacio, C. Pellegrini, and L. Narducci. Collective instabilities and high-gain regime in a free electron laser. *Optics Communications*, 50(6):373–378, 1984.

[13] M. Borland. Elegant: A flexible sdds-compliant code for accelerator simulation. Technical Report LS-287, Argonne National Laboratory Advanced Photon Source, 8 2000. URL: https://www.osti.gov/biblio/761286, doi:10.2172/761286.

[14] M. Borland. Design and performance simulations of the bunch compressor for the advanced photon source low-energy undulator test line free electron laser. *Physical Review Special Topics-Accelerators and Beams*, 4:074201, 2001. doi:10.1103/PhysRevSTAB.4.074201.

[15] T. J. Campese et al. Strongly tapered helical undulator system for tessa-266. In *Proceedings, North-America Particle Accelerator Conference*, page MOZBA3, 2019.

[16] G. L. Carr, M. C. Martin, W. R. McKinney, K. Jordan, G. R. Neil, and G. P. Williams. Very high power THz radiation at jefferson lab. *Physics in Medicine and Biology*, 47(21):3761–3764, oct 2002. doi:10.1088/0031-9155/47/21/313.

[17] A. Chao and M. Tigner. *Handbook of Accelerator Physics and Engineering*. Handbook of Accelerator Physics and Engineering. World Scientific, 1999.

[18] H. N. Chapman and et al. Femtosecond x-ray protein nanocrystallography. *Nature*, 470(7332):73–77, Feb 2011. doi:10.1038/nature09750.

[19] O. Chubar, P. Elleaume, and J. Chavanne. A three-dimensional magnetostatics computer code for insertion devices. *Journal of synchrotron radiation*, 5(3):481–484, 1998.

[20] P. E. O. Chubar and J. Chavanne. Computing 3d magnetic field from insertion devices. In *Particle Accelerator Conf. PAC97*, pages 3509–3511, 1997.

[21] J. Clarke. *The Science and Technology of Undulators and Wigglers*. Oxford Series on Synchrotron Radiation. OUP Oxford, 2004.

[22] R. N. Coffee, J. P. Cryan, J. Duris, W. Helml, S. Li, and A. Marinelli. Development of ultrafast capabilities for x-ray free-electron lasers at the linac coherent light source. *Philosophical Transactions of the Royal Society A: Mathematical, Physical and Engineering Sciences*, 377(2145):20180386, 2019. URL: https://royalsocietypublishing.org/doi/abs/10.1098/rsta.2018.0386, doi:10.1098/rsta.2018.0386.

[23] D. A. G. Deacon, L. R. Elias, J. M. J. Madey, G. J. Ramian, H. A. Schwettman, and T. I. Smith. First operation of a free-electron laser. *Phys. Rev. Lett.*, 38:892–894, Apr 1977. URL: https://link.aps.org/doi/10.1103/PhysRevLett.38.892, doi:10.1103/PhysRevLett.38.892.

[24] S. S. Dhillon, M. S. Vitiello, E. H. Linfield, A. G. Davies, M. C. Hoffmann, J. Booske, C. Paoloni, M. Gensch, P. Weightman, G. P. Williams, E. Castro-Camus, D. R. S. Cumming, F. Simoens, I. Escorcia-Carranza, J. Grant, S. Lucyszyn, M. Kuwata-Gonokami, K. Konishi, M. Koch, C. A. Schmuttenmaer, T. L. Cocker, R. Huber, A. G. Markelz, Z. D. Taylor, V. P. Wallace, J. A. Zeitler, J. Sibik, T. M. Korter, B. Ellison, S. Rea, P. Goldsmith, K. B. Cooper, R. Appleby, D. Pardo, P. G. Huggard, V. Krozer, H. Shams, M. Fice, C. Renaud, A. Seeds, A. Stöhr, M. Naftaly, N. Ridler, R. Clarke, J. E. Cunningham, and M. B. Johnston. The 2017 terahertz science and technology roadmap. *Journal of Physics D: Applied Physics*, 50(4):043001, jan 2017. doi:10.1088/1361-6463/50/4/043001.

[25] R. H. Dicke. Coherence in spontaneous radiation processes. *Phys. Rev.*, 93:99–110, Jan 1954. URL: https://link.aps.org/doi/10.1103/PhysRev.93.99, doi:10.1103/PhysRev.93.99.

[26] L. Duffy, K. Bishofberger, J. Lewellen, S. Russell, and D. Shchegolkov. Photo-Injector Optimization and Validation Study with the OPAL Beam Simulation Code. In *Proc. of North American Particle Accelerator Conference (NAPAC'16), Chicago, IL, USA, October 9-14, 2016*, number 3 in North American Particle Accelerator Conference, pages 984–986. JACoW. doi:https://doi.org/10.18429/JACoW-NAPAC2016-WEPOB39.

[27] O. Dumbrajs and G. S. Nusinovich. Efficiency of gyrotrons with a tapered magnetic field in the regime of soft self-excitation. *Physics of Plasmas*, 25(1):013121, 2018. doi:10.1063/1.5019974.

[28] E. Duplay, Z. F. Bao, S. Rodriguez Rosero, A. Sinha, and A. Higgins. Design of a rapid transit to mars mission using laser-thermal propulsion. *Acta Astronautica*, 192:143–156, 2022. URL: https://www.sciencedirect.com/science/article/pii/S0094576521006305, doi:https://doi.org/10.1016/j.actaastro.2021.11.032.

[29] J. Duris, A. Murokh, and P. Musumeci. Tapering enhanced stimulated superradiant amplification. *New Journal of Physics*, 17(6):063036, 2015.

[30] J. Duris, P. Musumeci, and R. Li. Inverse free electron laser accelerator for advanced light sources. *Physical Review Special Topics - Accelerators and Beams*, 15(6):061301, 2012. doi:10.1103/PhysRevSTAB.15.061301.

[31] J. Duris, P. Musumeci, N. Sudar, A. Murokh, and A. Gover. Tapering enhanced stimulated superradiant oscillator. *Physical Review Accelerators and Beams*, 21(8), 8 2018. doi:10.1103/PhysRevAccelBeams.21.080705.

[32] F. R. Elder, A. M. Gurewitsch, R. V. Langmuir, and H. C. Pollock. Radiation from electrons in a synchrotron. *Phys. Rev.*, 71:829–830, Jun 1947. URL: https://link.aps.org/doi/10.1103/PhysRev.71.829.5, doi:10.1103/PhysRev.71.829.5.

[33] L. R. Elias, W. M. Fairbank, J. M. J. Madey, H. A. Schwettman, and T. I. Smith. Observation of stimulated emission of radiation by relativistic electrons in a spatially periodic transverse magnetic field. *Physical Review Letters*, 36:717–720, Mar 1976. URL: https://link.aps.org/doi/10.1103/PhysRevLett.36.717, doi:10.1103/PhysRevLett.36.717.

[34] C. Emma. *High efficiency, high brightness X-ray free electron laser pulses via fresh bunch self-seeding and undulator tapering*. PhD thesis, University of California, Los Angeles, 2017.

[35] C. Emma, K. Fang, J. Wu, and C. Pellegrini. High efficiency, multiterawatt x-ray free electron lasers. *Physical Review Accelerators and Beams*, 19(2):020705, 2016.

[36] C. Emma, K. Fang, J. Wu, and C. Pellegrini. High efficiency, multiterawatt x-ray free electron lasers. *Physical Review Accelerators and Beams*, 19(2):020705, 2016. doi:10.1103/PhysRevAccelBeams.19.020705.

[37] P. Emma, R. Akre, and et al. First lasing and operation of an ångstrom-wavelength free-electron laser. *Nature Photonics*, 4(9):641–647, Sept. 2010. doi:10.1038/nphoton.2010.176.

[38] J. F. Stephen hawking, mark zuckerberg, yuri milner launch $100m space project called breakthrough starshot, Apr 2016. URL: https://www.natureworldnews.com/articles/20799/20160414/stephen-hawking-mark-zuckerberg-and-russian-millionaire-yuri-milner-launch-100m-space-project-called-breakthrough-starshot.htm.

[39] W. M. Fawley, Z. Huang, K.-J. Kim, and N. A. Vinokurov. Tapered undulators for sase fels. *Nuclear Instruments and Methods in Physics Research Section A: Accelerators, Spectrometers, Detectors and Associated Equipment*, 483(1-2):537–541, 2002.

[40] A. Fisher, P. Musumeci, and S. Van der Geer. Self-consistent numerical approach to track particles in free electron laser interaction with electromagnetic field modes. *Physical Review Accelerators and Beams*, 23(11):110702, 2020.

[41] A. Fisher, Y. Park, M. Lenz, A. Ody, R. Agustsson, T. Hodgetts, A. Murokh, and P. Musumeci. Single-pass high-efficiency terahertz free-electron laser. *Nature Photonics*, May 2022. doi:10.1038/s41566-022-00995-z.

[42] K. Flottmann, S. Lidia, and P. Piot. Recent improvements to the astra particle tracking code. 5:3500–3502, 01 2003. doi:10.1109/PAC.2003.1289961.

[43] I. Fomenkov. Euv source for lithography in hvm: performance and prospects. URL: https://www.euvlitho.com/2019/S1.pdf.

[44] I. Fomenkov, D. Brandt, A. Ershov, A. Schafgans, Y. Tao, G. Vaschenko, S. Rokitski, M. Kats, M. Vargas, M. Purvis, R. Rafac, B. L. Fontaine, S. D. Dea, A. LaForge, J. Stewart, S. Chang, M. Graham, D. Riggs, T. Taylor, M. Abraham, and D. Brown. Light sources for high-volume manufacturing euv lithography: technology, performance, and power scaling. *Advanced Optical Technologies*, 6(3-4):173–186, 2017. URL: https://doi.org/10.1515/aot-2017-0029, doi:doi:10.1515/aot-2017-0029.

[45] A. Fratalocchi and G. Ruocco. Single-molecule imaging with x-ray free-electron lasers: Dream or reality? *Physical Review Letters*, 106(10):105504, 2011.

[46] A. Gover. Superradiant and stimulated-superradiant emission in prebunched electron-beam radiators. i. formulation. *Phys. Rev. ST Accel. Beams*, 8:030701, Mar 2005. URL: https://link.aps.org/doi/10.1103/PhysRevSTAB.8.030701, doi:10.1103/PhysRevSTAB.8.030701.

[47] A. Gover and E. Dyunin. Coherence of e-beam radiation sources and fels - a theoretical overview. *28th International Free Electron Laser Conference, FEL 2006*, 01 2006.

[48] A. Gover, R. Ianconescu, A. Friedman, C. Emma, N. Sudar, P. Musumeci, and C. Pellegrini. Superradiant and stimulated-superradiant emission of bunched electron beams. *Reviews of Modern Physics*, 91(3):035003, 2019.

[49] G. Granucci, G. Aiello, S. Alberti, K. Avramidis, F. Braunmüller, A. Bruschi, J. Chelis, J. Franck, L. Figini, G. Gantenbein, S. Garavaglia, G. Grossetti, S. Illy, Z. Ioannidis, J. Jelonnek, P. Kalaria, G. Latsas, A. Moro, I. G. Pagonakis, D. Peponis, E. Poli, N. Rispoli, T. Rzesnicki, T. Scherer, D. Strauss, M. Thumm, I. Tigelis, C. Tsironis, C. Wu, T. Franke, and M. Tran. Conceptual design of the EU DEMO EC-system: main developments and r&d achievements. *Nuclear Fusion*, 57(11):116009, aug 2017. doi:10.1088/1741-4326/aa7b15.

[50] Hafizi, Ting, Sprangle, and Tang. Development of sidebands in tapered and untapered free-electron lasers. *Physical review. A, General physics*, 38 1:197–203, 1988.

[51] B. Hafizi, A. Ting, P. Sprangle, and C. Tang. Efficiency enhancement and optical guiding in a tapered high-power finite-pulse free-electron laser. *Physical Review Letters*, 64(2):180, 1990.

[52] J. Hecht. The history of the x-ray laser, 2008. URL: https://www.optica-opn.org/home/articles/volume_19/issue_5/features/the_history_of_the_x-ray_laser/.

[53] E. Hemsing, G. Stupakov, D. Xiang, and A. Zholents. Beam by design: Laser manipulation of electrons in modern accelerators. *Rev. Mod. Phys.*, 86:897–941, Jul 2014. URL: https://link.aps.org/doi/10.1103/RevModPhys.86.897, doi:10.1103/RevModPhys.86.897.

[54] M. Hogan, C. Pellegrini, J. Rosenzweig, G. Travish, A. Varfolomeev, S. Anderson, K. Bishofberger, P. Frigola, A. Murokh, N. Osmanov, S. Reiche, and A. Tremaine. Measurements of high gain and intensity fluctuations in a self-amplified, spontaneous-emission free-electron laser. *Phys. Rev. Lett.*, 80:289–292, Jan 1998. URL: https://link.aps.org/doi/10.1103/PhysRevLett.80.289, doi:10.1103/PhysRevLett.80.289.

[55] E. R. Hosler. Next generation source power requirements. URL: https://www.euvlitho.com/2017/P15.pdf.

[56] E. R. Hosler, O. R. Wood II, and W. A. Barletta. Free-electron laser emission architecture impact on extreme ultraviolet lithography. *Journal of Micro/Nanolithography, MEMS, and MOEMS*, 16(4):041009, 2017.

[57] Y. Jiao, J. Wu, Y. Cai, A. Chao, W. Fawley, J. Frisch, Z. Huang, H.-D. Nuhn, C. Pellegrini, and S. Reiche. Modeling and multidimensional optimization of a tapered free electron laser. *Physical Review Special Topics-Accelerators and Beams*, 15(5):050704, 2012.

[58] K. Kawase, M. Nagai, K. Furukawa, M. Fujimoto, R. Kato, Y. Honda, and G. Isoyama. Extremely high-intensity operation of a thz free-electron laser using an electron beam with a higher bunch charge. *Nuclear Instruments and Methods in Physics Research Section A: Accelerators, Spectrometers, Detectors and Associated Equipment*, 960:163582, 2020. doi:https://doi.org/10.1016/j.nima.2020.163582.

[59] D. W. Kerst. The acceleration of electrons by magnetic induction. *Phys. Rev.*, 60:47–53, Jul 1941. URL: https://link.aps.org/doi/10.1103/PhysRev.60.47, doi:10.1103/PhysRev.60.47.

[60] D. W. Kerst. Historical development of the betatron. *Nature*, 157(3978):90–95, Jan 1946. URL: https://doi.org/10.1038/157090a0.

[61] V. Kesari and B. N. Basu. Fast-wave tubes. In *High Power Microwave Tubes: Basics and Trends, Volume 2*, 2053-2571. Morgan and Claypool Publishers, 2018. URL: https://dx.doi.org/10.1088/978-1-6817-4704-0ch7, doi:10.1088/978-1-6817-4704-0ch7.

[62] N. Kroll, P. Morton, and M. Rosenbluth. Free-electron lasers with variable parameter wigglers. *IEEE Journal of Quantum Electronics*, 17(8):1436–1468, 1981. doi:10.1109/JQE.1981.1071285.

[63] G. Kulipanov, N. Gavrilov, B. Knyazev, E. Kolobanov, V. Kotenkov, V. Kubarev, A. Matveenko, L. Medvedev, S. Miginsky, L. Mironenko, et al. Research highlights from the novosibirsk 400 w average power thz fel. *Terahertz Sci. Technol*, 1(2):107–125, 2008.

[64] N. Kumar, U. Singh, A. Bera, and A. Sinha. A review on the sub-thz/thz gyrotrons. *Infrared Physics & Technology*, 76:38–51, 2016. URL: https://www.sciencedirect.com/science/article/pii/S1350449515301316, doi:https://doi.org/10.1016/j.infrared.2016.01.015.

[65] S. Kutsaev et al. A new thermionic rf electron gun for synchrotronlight sources. In *Proceedings, North-America Particle Accelerator Conference*, page TUB3CO04, 2016.

[66] M. Lenz and P. Musumeci. Electro-optic sampling based characterization of broadband high efficiency thz-fel. 2022.

[67] I. Levchenko, K. Bazaka, S. Mazouffre, and S. Xu. Prospects and physical mechanisms for photonic space propulsion. *Nature Photonics*, 12(11):649–657, Nov 2018. URL: https://doi.org/10.1038/s41566-018-0280-7.

[68] A. G. Litvak, G. G. Denisov, and M. Y. Glyavin. Russian gyrotrons: Achievements and trends. *IEEE Journal of Microwaves*, 1(1):260–268, 2021. doi:10.1109/JMW.2020.3030917.

[69] A. Mak, F. Curbis, and S. Werin. Model-based optimization of tapered free-electron lasers. *Physical Review Special Topics-Accelerators and Beams*, 18(4):040702, 2015.

[70] G. Marcus, A. Halavanau, Z. Huang, J. Krzywinski, J. MacArthur, R. Margraf, T. Raubenheimer, and D. Zhu. Refractive guide switching a regenerative amplifier free-electron laser for high peak and average power hard x rays. *Physical Review Letters*, 125, 12 2020. doi:10.1103/PhysRevLett.125.254801.

[71] M. Maslov, V. Sychev, and M. Schmitz. Layout considerations on the 25gev/300kw beam dump of the xfel project. Technical Report TESLA-FEL–2006-05, Deutsches Elektronen-Synchrotron (DESY), 2006.

[72] M. Mastenbroek. Progress on 0.33 NA EUV systems for High-Volume Manufacturing. In T. Itani, P. A. Gargini, P. P. Naulleau, and K. G. Ronse, editors, *International Conference on Extreme Ultraviolet Lithography 2019*, volume 11147, pages 1 – 11. International Society for Optics and Photonics, SPIE, 2019. doi:10.1117/12.2532110.

[73] P. Mayer, D. C. Brandt, I. Fomenkov, M. Purvis, and D. Brown. Laser produced plasma EUV sources for N5 HVM and beyond: performance, availability and technology innovation. In N. M. Felix and A. Lio, editors, *Extreme Ultraviolet (EUV) Lithography XII*, volume 11609. International Society for Optics and Photonics, SPIE, 2021. doi:10.1117/12.2584407.

[74] D. Milam. Review and assessment of measured values of the nonlinear refractive-index coefficient of fused silica. *Appl. Opt.*, 37(3):546–550, Jan 1998. URL: http://ao.osa.org/abstract.cfm?URI=ao-37-3-546, doi:10.1364/AO.37.000546.

[75] S. Mitsudo, Aripin, T. Shirai, T. Matsuda, T. Kanemaki, and T. Idehara. High power, frequency tunable, submillimeter wave esr device using a gyrotron as a radiation source. *International Journal of Infrared and Millimeter Waves*, 21(4):661–676, Apr 2000. doi:10.1023/A:1006648223636.

[76] H. Motz, W. Thon, and R. N. Whitehurst. Experiments on radiation by fast electron beams. *Journal of Applied Physics*, 24(7):826–833, 1953. doi:10.1063/1.1721389.

[77] A. Murokh, P. Musumeci, A. Zholents, and S. Webb. Towards a compact high efficiency fel for industrial applications. In *Compact EUV & X-ray Light Sources*, pages EW4A–3. Optical Society of America, 2020.

[78] L. Myrabo. *World record flights of beam-riding rocket lightcraft - Demonstration of "disruptive" propulsion technology.* URL: https://arc.aiaa.org/doi/abs/10.2514/6.2001-3798, arXiv:https://arc.aiaa.org/doi/pdf/10.2514/6.2001-3798, doi:10.2514/6.2001-3798.

[79] R. Neutze, R. Wouts, D. van der Spoel, E. Weckert, and J. Hajdu. Potential for biomolecular imaging with femtosecond x-ray pulses. *Nature*, 406(6797):752–757, Aug 2000. doi:10.1038/35021099.

[80] Y. Oda, K. Komurasaki, K. Takahashi, A. Kasugai, T. Imai, and K. Sakamoto. Plasma Generation at Atmospheric Pressure using a High Power Microwave Beam and its Application to Rocket Propulsion. *IEEJ Transactions on Fundamentals and Materials*, 126(8):807–812, Jan. 2006. doi:10.1541/ieejfms.126.807.

[81] T. J. Orzechowski, B. R. Anderson, J. C. Clark, W. M. Fawley, A. C. Paul, D. Prosnitz, E. T. Scharlemann, S. M. Yarema, D. B. Hopkins, A. M. Sessler, and J. S. Wurtele. High-efficiency extraction of microwave radiation from a tapered-wiggler free-electron laser. *Physical Review Letters*, 57:2172–2175, 1986.

[82] D. O'Reilly, G. Herdrich, and D. F. Kavanagh. Electric propulsion methods for small satellites: A review. *Aerospace*, 8(1), 2021. URL: https://www.mdpi.com/2226-4310/8/1/22, doi:10.3390/aerospace8010022.

[83] H. Padamsee. 50 years of success for srf accelerators—a review. *Superconductor science and technology*, 30(5):053003, 2017.

[84] C. Pagani, E. Saldin, E. Schneidmiller, and M. Yurkov. Design considerations of 10kw-scale extreme ultraviolet sase fel for lithography. *Nuclear Instruments and Methods in Physics Research Section A: Accelerators, Spectrometers, Detectors and Associated Equipment*, 463(1-2):9–25, 2001.

[85] Y. Park, R. Agustsson, W. Berg, J. Byrd, T. Campese, D. Dang, P. Denham, J. Dooling, A. Fisher, I. Gadjev, C. Hall, J. Isen, J. Jin, A. Lumpkin,

A. Murokh, Y. Sun, W. Tan, S. Webb, K. Wootton, A. Zholents, and P. Musumeci. Tapered helical undulator system for high efficiency energy extraction from a high brightness electron beam. *Nuclear Instruments and Methods in Physics Research Section A: Accelerators, Spectrometers, Detectors and Associated Equipment*, 1028:166370, 2022. URL: https://www.sciencedirect.com/science/article/pii/S0168900222000456, doi:https://doi.org/10.1016/j.nima.2022.166370.

[86] C. Pellegrini, A. Marinelli, and S. Reiche. The physics of x-ray free-electron lasers. *Rev. Mod. Phys.*, 88:015006, Mar 2016. URL: https://link.aps.org/doi/10.1103/RevModPhys.88.015006, doi:10.1103/RevModPhys.88.015006.

[87] C. Phipps, M. Birkan, W. Bohn, H.-A. Eckel, H. Horisawa, T. Lippert, M. Michaelis, Y. Rezunkov, A. Sasoh, W. Schall, S. Scharring, and J. Sinko. Review: Laser-ablation propulsion. *Journal of Propulsion and Power*, 26(4):609–637, 2010. URL: https://doi.org/10.2514/1.43733.

[88] C. Phipps, C. Bonnal, F. Masson, and P. Musumeci. Launching swarms of microsatellites using a kw average power pulsed laser. *J. Opt. Soc. Am. B*, 35(10):B20–B26, Oct 2018. URL: http://opg.optica.org/josab/abstract.cfm?URI=josab-35-10-B20, doi:10.1364/JOSAB.35.000B20.

[89] C. R. Phipps, C. Bonnal, F. Masson, M. Boustie, L. Berthe, M. Schneider, S. Baton, E. Brambrink, J.-M. Chevalier, L. Videau, and S. A. Boyer. Transfers from earth to leo and leo to interplanetary space using lasers. *Acta Astronautica*, 146:92–102, 2018. doi:https://doi.org/10.1016/j.actaastro.2018.02.018.

[90] D. Prosnitz, A. Szoke, and V. K. Neil. High-gain, free-electron laser amplifiers: Design considerations and simulation. *Phys. Rev. A*, 24:1436–1451, Sep 1981. URL: https://link.aps.org/doi/10.1103/PhysRevA.24.1436, doi:10.1103/PhysRevA.24.1436.

[91] G. Ramian. The new ucsb free-electron lasers. *Nuclear Instruments and Methods in Physics Research Section A: Accelerators, Spectrometers, Detectors and Associated Equipment*, 318(1):225–229, 1992. doi:https://doi.org/10.1016/0168-9002(92)91056-F.

[92] S. Reiche. Genesis 1.3: a fully 3d time-dependent fel simulation code. *Nuclear Instruments and Methods in Physics Research Section A: Accelerators, Spectrometers, Detectors and Associated Equipment*, 429(1-3):243–248, 1999.

[93] E. Saldin, E. Schneidmiller, and M. Yurkov. The physics of free electron lasers. an introduction. *Physics Reports*, 260(4):187–327, 1995. doi:https://doi.org/10.1016/0370-1573(95)00004-Z.

[94] C. J. Saraceno, D. Sutter, T. Metzger, and M. Abdou Ahmed. The amazing progress of high-power ultrafast thin-disk lasers. *Journal of the European Optical Society-Rapid Publications*, 15(1):15, Jun 2019. doi:10.1186/s41476-019-0108-1.

[95] E. T. Scharlemann, A. M. Sessler, and J. S. Wurtele. Optical guiding in a free-electron laser. *Phys. Rev. Lett.*, 54:1925–1928, Apr 1985.

[96] P. Schmüser, M. Dohlus, and J. Rossbach. *Ultraviolet and Soft X-Ray Free-Electron Lasers*. 2014. doi:https://doi.org/10.1007/978-3-319-04081-3.

[97] E. A. Schneidmiller and M. Yurkov. Optimization of a high efficiency free electron laser amplifier. *Physical Review Special Topics-Accelerators and Beams*, 18(3):030705, 2015.

[98] J. V. Schoot, S. Lok, E. van Setten, R. Maas, K. Troost, R. Peeters, J. Finders, J. Stoeldraijer, J. Benschop, P. Graeupner, P. Kuerz, and W. Kaiser. High-NA EUV lithography exposure tool: advantages and program progress. In P. P. Naulleau, P. A. Gargini, T. Itani, and K. G. Ronse, editors, *Extreme Ultraviolet Lithography 2020*, volume 11517, pages 76 – 89. International Society for Optics and Photonics, SPIE, 2021. doi:10.1117/12.2572932.

[99] M. M. Seibert and et al. Single mimivirus particles intercepted and imaged with an x-ray laser. *Nature*, 470(7332):78–81, Feb 2011. doi:10.1038/nature09748.

[100] L. Serafini and M. Ferrario. Velocity bunching in photo-injectors. *AIP Conference Proceedings*, 581(1):87–106, 2001. URL: https://aip.scitation.org/doi/abs/10.1063/1.1401564, arXiv:https://aip.scitation.org/doi/pdf/10.1063/1.1401564, doi:10.1063/1.1401564.

[101] N. S. Sereno. Linac Deflecting Cavity Diagnostic Analysis and Placement. (2), 2012. arXiv:AOP-TN-2012-043,Rev.2.

[102] S. Shin, Y. Sun, J. Dooling, M. Borland, and A. Zholents. Interleaving lattice for the argonne advanced photon source linac. *Physical Review Accelerators and Beams*, 21:060101, Jun 2018. URL: https://link.aps.org/doi/10.1103/PhysRevAccelBeams.21.060101, doi:10.1103/PhysRevAccelBeams.21.060101.

[103] A. S. Singh and M. Thottappan. Bunching parameter study of hybrid gyrotron amplifier. In *2020 German Microwave Conference (GeMiC)*, pages 276–279, 2020. URL: https://ieeexplore.ieee.org/document/9080223.

[104] C. Smeets, R. V. Es, R. D. Graaf, L. Levasier, M. Mastenbroek, and E. Verhoeven. 0.33 NA EUV systems for high-volume manufacturing. In K. G. Ronse, P. P. Naulleau, P. A. Gargini, T. Itani, and E. Hendrickx, editors, *International Conference on Extreme Ultraviolet Lithography 2021*, volume 11854. International Society for Optics and Photonics, SPIE, 2021. doi:10.1117/12.2600961.

[105] P. Sprangle, A. Ting, and C. M. Tang. Radiation focusing and guiding with application to the free electron laser. *Phys. Rev. Lett.*, 59:202–205, Jul 1987. URL: https://link.aps.org/doi/10.1103/PhysRevLett.59.202, doi:10.1103/PhysRevLett.59.202.

[106] N. Sudar, Y. Ding, Y. Nosochkov, K. Bane, and Z. Zhang. Octupole based current horn suppresion in multi-stage bunch compression with emittance growth correction. *Physical Review Accelerators and Beams*, 23(11):112802, 2020. doi:10.1103/PhysRevAccelBeams.23.112802.

[107] N. Sudar, P. Musumeci, J. Duris, I. Gadjev, M. Polyanskiy, I. Pogorelsky, M. Fedurin, C. Swinson, K. Kusche, M. Babzien, and A. Gover. High efficiency energy extraction from a relativistic electron beam in a strongly tapered undulator. *Physical Review Letters*, 117:174801, Oct 2016. doi:10.1103/PhysRevLett.117.174801.

[108] N. S. Sudar. *Interactions of pre-bunched relativistic electron beams and electromagnetic waves in strongly tapered undulators*. PhD thesis, University of California, Los Angeles, 2019.

[109] Y. Sun, P. Emma, T. Raubenheimer, and J. Wu. x-band rf driven free electron laser driver with optics linearization. *Phys. Rev. ST Accel. Beams*, 17:110703, Nov 2014. URL: https://link.aps.org/doi/10.1103/PhysRevSTAB.17.110703, doi:10.1103/PhysRevSTAB.17.110703.

[110] M. Thumm, G. Denisov, K. Sakamoto, and M. Tran. High-power gyrotrons for electron cyclotron heating and current drive. *Nuclear Fusion*, 59(7):073001, jun 2019. doi:10.1088/1741-4326/ab2005.

[111] M. Thumm, G. Denisov, K. Sakamoto, and M. Tran. High-power gyrotrons for electron cyclotron heating and current drive. *Nuclear Fusion*, 59(7):073001, jun 2019. doi:10.1088/1741-4326/ab2005.

[112] S. B. van der Geer, O. J. Luiten, M. J. de Loos, G. Poplau, and U. van Rienen. 3D space-charge model for GPT simulations of high-brightness electron bunches. *Inst. Phys. Conf. Ser.*, 175:101–110, 2005.

[113] R. Warren, B. Newnam, J. Winston, W. Stein, L. Young, and C. Brau. Results of the los alamos free-electron laser experiment. *IEEE Journal of Quantum Electronics*, 19(3):391–401, 1983. doi:10.1109/JQE.1983.1071854.

[114] M. J. Weber. *Handbook of laser wavelengths*. CRC Press, Boca Raton, 1999.

[115] J. T. Weir, T. J. Orzechowski, J. L. Miller, Y. P. Chong, F. Chambers, G. A. Deis, A. C. Paul, D. Prosnitz, E. T. Scharlemann, K. Halbach, and J. Edighoffer. Results Of The PALADIN Experiment. In Y. Petroff, editor, *Free Electron Lasers II*, volume 1133, pages 97 – 101. International Society for Optics and Photonics, SPIE, 1989. doi:10.1117/12.961604.

[116] H. Wiedemann. *Particle accelerator physics; 3rd ed.* Springer, Berlin, 2007.

[117] S. P. Worden, W. A. Green, J. Schalkwyk, K. Parkin, and R. Q. Fugate. Progress on the starshot laser propulsion system. *Appl. Opt.*, 60(31):H20–H23, Nov 2021. URL: http://opg.optica.org/ao/abstract.cfm?URI=ao-60-31-H20, doi:10.1364/AO.435858.

[118] V. Yakimenko, L. Alsberg, E. Bong, G. Bouchard, C. Clarke, C. Emma, S. Green, C. Hast, M. Hogan, J. Seabury, et al. Facet-ii facility for advanced accelerator experimental tests. *Physical Review Accelerators and Beams*, 22(10):101301, 2019.

[119] Z. Zhang, K. Bane, Y. Ding, Z. Huang, R. Iverson, T. Maxwell, G. Stupakov, and L. Wang. Electron beam energy chirp control with a rectangular corrugated structure at the linac coherent light source. *Physical Review Special Topics-Accelerators and Beams*, 18(1):010702, 2015.

[120] Z. Zhang, R. Lindberg, W. M. Fawley, Z. Huang, J. Krzywinski, A. Lutman, G. Marcus, and A. Marinelli. Microbunching-instability-induced sidebands in a seeded free-electron laser. *Phys. Rev. Accel. Beams*, 19:050701, May 2016. URL: https://link.aps.org/doi/10.1103/PhysRevAccelBeams.19.050701, doi:10.1103/PhysRevAccelBeams.19.050701.